ROCKFALL SUSCEPTIBILITY ASSESSMENT ON UAV BASED 3D POINT CLOUDS

DANIEL SEABRA NOGUEIRA ALVES ALBARELLI
June 2020

SUPERVISORS:
Assistant Professor, Dr. Olga Christina Mavrouli
Lecturer, Dr. Panagiotis Nyktas

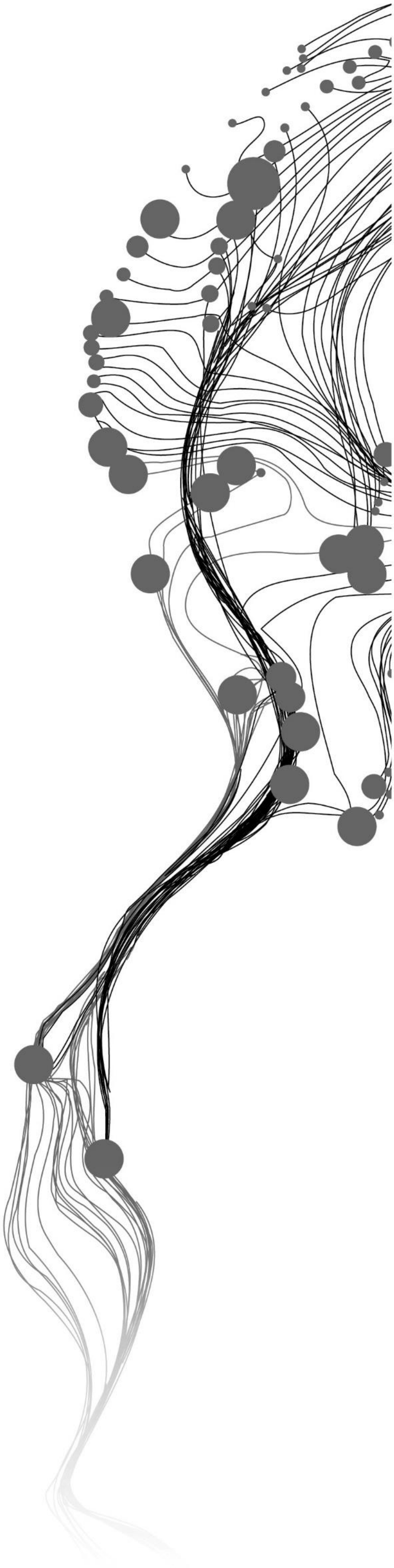

ROCKFALL SUSCEPTIBILITY ASSESSMENT ON UAV BASED 3D POINT CLOUDS

DANIEL SEABRA NOGUEIRA ALVES ALBARELLI
Enschede, The Netherlands, June 2020

Thesis submitted to the Faculty of Geo-Information Science and Earth Observation of the University of Twente in partial fulfilment of the requirements for the degree of Master of Science in Geo-information Science and Earth Observation.
Specialization: Natural Hazard and Disaster Risk Reduction

SUPERVISORS:
Assistant Professor, Dr. Olga Christina Mavrouli
Lecturer, Dr. Panagiotis Nyktas

THESIS ASSESSMENT BOARD:
Prof. Dr. Victor Jetten (Chair)
Assistant Professor, Dr. Harry Seijmonsbergen (External Examiner, University of Amsterdam)

ABSTRACT

Rockfall is a common geological hazard in mountainous areas causing economic and human losses when fallen blocks impact infrastructure and communities along its way. A key aspect on the mitigation of such losses starts by identifying in a rock slope (or cliff) the source areas where blocks are more likely to detach and generate rockfalls. This is the aim of the Rockfall Susceptibility Assessment, which constitutes the initial step for the following Hazard Assessment, such as estimation of block volume and rockfall simulation (trajectory, energy, rebound height). Geomechanical properties of rock mass play a major role especially for local assessments since discontinuity geometry and orientation largely govern the rock mass quality and stability.

Due to recent advances in remote sensing techniques, rock mass characterization is shifting from the traditional labor-intensive field surveys to the 3D point cloud environment, where accurate, abundant and high-resolution geometric information can be retrieved. Unmanned Aerial Vehicle (UAV) has been used as a platform to acquire RGB photographs of rock slopes and, through the photogrammetric method of Structure from Motion, generate 3D point clouds (3DPC). Nevertheless, the application of this technology to Rockfall Susceptibility Assessment is still in its early developments and there is a lack in the literature on methodologies tailored for application to UAV.

This thesis presents a comprehensive and novel methodology to fill this gap. It consists of 4 major sequential blocks: (i)) use of UAV photogrammetry with data acquisition to 3DPC generation, (ii) Feature extraction for rock mass characterization in which joint set orientation, persistence, spacing and block volume are obtained, (iii) Slope Stability Assessment by applying the extracted features firstly in Rock Mass Rating (RMR), followed by Slope Mass Rating (SMR) for each joint set and (iv) development of indicator for spacing, persistence, overhanging and SMR indexes, followed by their integration for a Rockfall Susceptibility Index.

This methodology was tested to a road cut rock slope of approximately 46 m lateral extension and 14 m height in a mountainous area of the Samaria Gorge National Park, in Crete Island (Greece). Visual validation shows that areas of higher and moderated rockfall susceptibility on the rock slope correspond to source location from where the bigger and highest number of fallen blocks were found on the foot of the slope. Hence, this approach helps to refine the identification of potential rockfall source areas, which are areas prone to rock detachment compared to their surroundings and to improve the input for hazard assessment, including rockfall run out simulations. Additionally, the methodologic workflow contributes to the following innovations on 3DPC: Rock Quality Designation (RQD) index estimation, visualization of spacing, persistence and SMR index, semi-automatic block volume calculation for regularly shaped blocks formed by flat exposed surfaces on the rock mass, the persistence of overhanging enabling the distinction on the extension of lack of support and thus an indicator of greater volume susceptible to rockfall.

Keywords: UAV, rock mass, slope stability, rockfall susceptibility, 3D point clouds

ACKNOWLEDGEMENTS

The foundation in which my journey was built relies on the most solid rock, my Lord and Saviour Jesus Christ. All the honour and glory I give to Him.

I also express my gratitude to all of those who helped me along the way…

….my family members, a constant source of encouragement and motivation, especially my parents. Their love, self-sacrifice and dedication towards my sister and me cannot be measured and hardly retributed. God willing I will raise my children based on their example.

…my sister Camila and brother-in-law Henrique, for visiting me with my nephew in the Netherlands and the good times together here and back home.

…my little nephew Gabriel, whose smile on recorded videos was a source of happiness when I felt tired of my daily routine. Although distant, he always remembered his absent uncle`s face and name (tio Dan).

…my supervisor Dr. Olga Mavrouli for the guidance, patience and great insights on the development of this thesis. Despite her busy schedule in teaching, research projects and other supervisions, ways welcomed me in her office and promptly replied to my emails.

…my supervisor Dr. Panagiotis Nyktas, for the assistance in the fieldwork activity, UAV data acquisition and all the logistics behind the scenes, especially in the context of bad weather conditions (raining and wind days) and the earthquake in Crete. He greatly contributed to the quality of input data for this work. One the last minutes of fieldwork, he managed to drive back to the study area and to take a sunlight window of opportunity to fly the UAV closer to the overhanging of the rock slope, which was occluded in previous flight attempts.

…the personnel and president, Petro Lymberakis, of the Management Body of Samaria – West Crete, and the Forest Directorate of Chania for the logistic support and permissions for the fieldwork activities in the area.

…Dr. Cees van Westen for the talks about life, career and faith.

…Drs. Nanette Kingma for all the hours dedicated to helping us, students, during class exercises, and group projects in the disciplines of this master. Without her help, I surely would not have reached the thesis phase.

…now MSc. Leojay Zhang from ITC Water department, for the friendship and help in the elective of Programming Solutions. He introduced me to a completely new world of scripts.

…now MSc. Mostafa Gooma from ITC Water department, for the friendship and motivation on the physical exercises alongside the studies. His discipline for a healthier life is a lesson learned for me.

…my brothers in Christ, Giuliano Clemente and Jan-Maarten Lubberts, for their friendship and support in prayer, talks and good times sharing food and laugh. My stayed in Enschede was much happier with them by my side.

I am also grateful to the University of Twente for providing me with the ITC Excellence Scholarship to study this master course, and coworkers from the Institute for Technological Research in Brazil to allow me this 2 years study time outside the office.

"… let your light shine before others, that they may see your good deeds and glorify your Father in heaven."

Matthew 5:16

TABLE OF CONTENTS

LIST OF FIGURES

LIST OF TABLES

LIST OF ABBREVIATIONS AND SYMBOLS

Abbreviations

3DPC	Three-Dimensional Point Cloud
DSE	Discontinuity Set Extractor Software
ISRM	International Society of Rock Mechanics
JS	Joint Set
RGB	Red Green Blue
RHRS	Rockfall Hazard Rating System
RMR	Rock Mass Rating System
RQD	Rock Quality Designation Index
SfM	Structure from Motion
SMR	Slope Mass Rating System
TLS	Terrestrial Laser Scanning
UAV	Unmanned Aerial Vehicle

Symbols

A	Plane equation first parameter (normal vector component)
B	Plane equation second parameter (normal vector component)
C	Plane equation third parameter (normal vector component)
C_h	Convex hull
Cl	Cluster
D	Plane equation fourth parameter: perpendicular distance from the origin
F_1	First adjustment factor for SMR
F_2	Second adjustment factor for SMR
F_3	Third adjustment factor for SMR
F_4	Fourth adjustment factor for SMR
k	Threshold parameter for merging clusters
S	Normal spacing
X	Coordinate of a point in x-axis of a cartesian coordinate system
Y	Coordinate of a point in y-axis of a cartesian coordinate system
Z	Coordinate of a point in z-axis of a cartesian coordinate system
σ	Standard deviation
β	Dip angle of a joint set
α	Dip direction of a joint set

1. INTRODUCTION

1.1. Background

Among natural hazards, rockfalls represent a serious threat for rock slopes and mountainous areas close to human settlements and infrastructure near the foot of the slope (Gigli et al., 2014). It is often recorded in the literature events of detached blocks rolling down steep slopes and causing damage to roads, houses, and infrastructure (Abellán et al., 2006; Sarro et al., 2018). The triggering factors that can lead to instability of the rock slope and therefore detachment of blocks are either natural or human-induced (Figure 1-1). For the first case, most commonly are intensive rainfall increasing pore water pressure in the joints, freeze-thaw actions, temperature change, ground shaking due to earthquakes and growing vegetation in the discontinuities planes. As for the second, dynamic vibration due to mine blasting, road cutting, and tunnelling on the foot slope. The basic principle behind these triggering factors is that they reduce the shear strength of rock mass, up to a point where the forces and moments preventing a slope fail become weakened enough to cause the failure of rock mass either by planar, wedge or toppling failure mechanism.

The identification of source areas prone to rock detachment, or slope instability, constitute the Rockfall Susceptibility Assessment, one of the fundamental elements for a Rockfall Hazard Assessment. There are several approaches for source area identification and rock slope stability analysis depending on the scale (local or regional), including kinematic feasibility tests, limit equilibrium methods, and the use of indexes such as the Slope Mass Rating (SMR). This latter is a rock mass classification system that provides information on the quality of rock slope in terms of probability of failure and failure mechanism. SMR has been used over the last years in regional scale (thousands of square meters) through Geographic Information System (GIS) for mapping slope quality and also as a parameter for quantifying rockfall susceptibility (Romana et al., 2015) For the local scale (up to hundreds of square meters), the approaches used for Rockfall susceptibility assessment commonly require the characterization of the rock mass, which includes the geomechanical properties such as discontinuities set, orientation, persistence, spacing, roughness and average block size or volume (Figure 1-1).

Besides the susceptibility, the other major elements for a Rockfall Hazard Assessment are the estimated volume of a detached block (magnitude), their trajectory and run-out (propagation), the impact velocity or energy of falling blocks (intensity) and the expected number of events for a given period (frequency) (Figure 1-1). One of the widely known methodology for Rockfall Hazard Assessment, the Rockfall Hazard Rating System (RHRS), was developed by Pierson (1991) to reduce risk in roads and highways in the mountains state of Oregon (USA). RHRS, as a qualitative approach, consider several parameters such as estimated block size, rockfall history (few to constant falls), discontinuity orientation (favourable to adverse orientation), climate and presence of water to give a score for a section of slope along highways and thus rank them into different hazard levels (9 categories). This methodology provided to transportation agencies across the country a systematic way to allocate their limited repair funds in areas of higher risk and opened the way for the development of other qualitative methods worldwide.

At the same time, qualitative approaches help to prioritize sections of a slope that are more prone to rockfall and thus require further detail investigation, the classification of this section may also have a great level of uncertainties since the parameters are subjectively estimated and dependent on knowledge of evaluator (Ferrari et al., 2016). On the other hand, the quantitative approaches that provide a more accurate estimation rely on a numerical dataset that is commonly expensive to obtain, might be incomplete or even unavailable, a common situation in many sites worldwide (Ferrari et al., 2016).

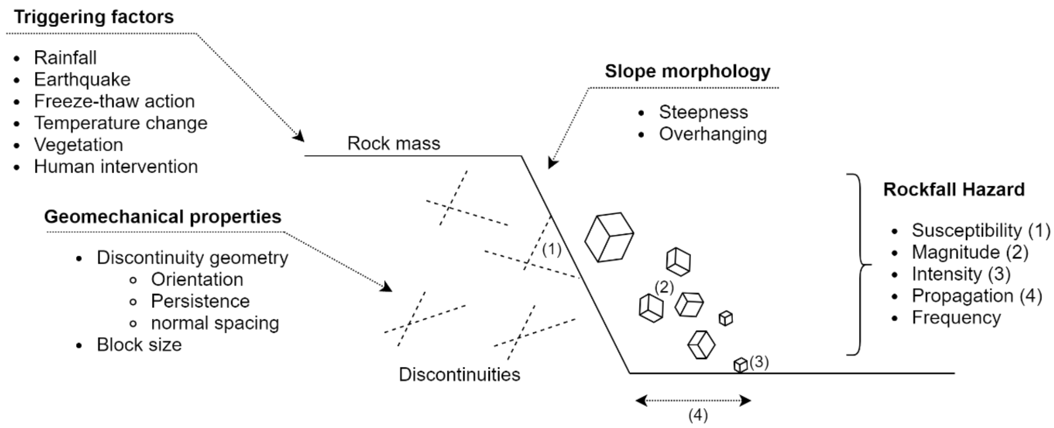

Figure 1-1. Conceptual framework of Rockfall Hazard. Source: own authorship.

1.2. Remote Sensing for Rockfall Susceptibility and Hazard Assessment

Advances of remote sensing techniques in the last decades have allowed the generation of high-resolution 3D model of the slope surface and extraction of geometric information. Terrestrial Laser Scanning (TLS) is one of the techniques that has been largely used in geohazard studies, especially on rockfalls and rock slope monitoring (Abellán et al., 2016). By setting this equipment in distance up to 1000m from the rock mass, it can be digitally recorded in the form of 3D Point Cloud (Abellán et al., 2006). From the point-cloud, the geomechanical properties can be extracted using different processing algorithms, software and methods such as Hough Transformation, Least Squares and Principal Component Analysis (Guta, 2017; Slob, 2010), Random Sample Consensus Shape detection algorithm - RANSAC (Wang et al., 2019), Discontinuity Set Extractor software - DSE (Riquelme et al.,), firefly algorithm - FA and the fuzzy c-mean algorithm - FMC (Guo et al., 2017).

A recent example of TLS application for Rockfall Susceptibility Assessment is the Rockfall Activity Index -RAI by Dunham et al. (2017). Based on a logic tree algorithm, the centimetric accurate TLS point cloud is classified into rock slope morphologic units, according to overhanging, slope angle, discontinuity spacing, and mass wasting fragments (talus). Each classified unit is then correlated with an estimated instability rate, obtained by annual change detection measurements of the slope surface. The instability rate is multiplied by the kinetic energy to calculate the RAI along the slope: the higher RAI value, the more susceptible to rockfall. Matasci et al., (2018) also performed a Rockfall Susceptibility Assessment on steep and overhanging slopes but using the discontinuities orientation retrieved from TLS point cloud instead of surface change detection. The discontinuities orientation and slope surface orientation were used in kinematic stability analysis to evaluate susceptibility for failure mechanism in the slope (planar, toppling, wedge, and exfoliation-type failure). The results of both studies were displayed in the TLS point cloud in a range of numerical values, representing different susceptibility levels.

Despite the fact of its long-range and precise measurements up to 4mm (Abellán et al., 2006), TLS has some drawbacks: high cost of operation, limited portability due to its heavy weight, untextured point cloud and occlusion, areas that are not reached by a laser beam (Guta, 2017; Sarro et al., 2018). Due to its variable distance-to-target, easier portability, and rock slope texture incorporation, there has been an increase in recent years of Unmanned Aerial Vehicle (UAV) based point cloud for Rockfall Hazard Assessment (Abellán et al., 2016). Point cloud generation from images taken from an UAV platform is done through a photogrammetric method known as Structure from Motion (SfM): 3D scene reconstruction based on overlapping images from multiple view angles (Westoby et al., 2012).

The most recent applications of rock mass geomechanical properties derived from UAV point clouds have been as input for rockfall simulations (Sarro et al., 2018), kinematic rock slope stability analysis (Menegoni et al., 2019; Wang et al., 2019) and Rockfall Susceptibility mapping in augmented reality (AR) environment (Zhang et al., 2019). In this latter, the authors developed a pioneer AR mapping methodology for an on-site visualization in a 2D screen (e.g tablet) of the rock mass discontinuities and rockfall susceptibility mapping on the natural slope, allowing an accurate location and zoning of potential rockfalls.

1.3. Research Problem

Rock mass characterization based on features extracted from 3D point cloud (TLS or UAV) allows high resolution and quantitatively accurate information. Nevertheless, research dealing with the application of UAV technology for Rockfall Susceptibility and Hazard Assessment is still in its early developments. The transition from a regional scale to a local scale using the extracted features are not well established in a step by step methodology. Automatic or semi-automatic methodologies for rockfall susceptibility assessment directly on the 3D models, at a local scale, are still poor compared to raster-based susceptibility assessment methods at a regional scale, and in most cases, it takes place manually based on user observations.

To the present moment, the approaches adopt mainly the discontinuity orientation for kinematic stability analyses and overhanging to define areas in the point cloud that are more susceptible to rock detachment. Few attempts have been made to identify these source areas directly on the point cloud. Additionally, the estimation of the rock size or volume in the identified prone areas for rock detachment is not taken into consideration. In the case of overhanging for instance, the greater the area or extension, the more likely to be unstable since it translates to a lack of support in the rock mass.

To develop a methodology for Rockfall Susceptibility assessment to be applied directly on UAV based 3D models of the slope, there should be a step by step procedure on how the features extracted from UAV point cloud can be used as indicators of source areas for rock detachment. A further effort should be made on how to incorporate these local features into a regional scale (e.g urban environment and transportation corridors). Traditionally for regional scales, only macro terrain characteristics used such as geology, slope angle, faults, and triggering factors whereas the local characteristics of rock mass are rarely incorporated (Saroglou, 2019).

1.4. Research Objective and Questions

The main research objective of this work is to develop a methodology for Rockfall Susceptibility Assessment using features extracted from UAV 3D Point Cloud (3DPC). To achieve this objective, the following specific research objectives and its related research questions are presented:

1) Develop a step by step procedure for feature extraction from UAV 3DPC. Focus will be given to geomechanical properties of the rock mass such as discontinuity geometry (orientation, persistence, spacing), block volume, and overhanging.
   a. How can the geomechanical properties of the rock mass be extracted from a UAV point cloud?
   b. Among them, which ones are extracted automatically and which ones manually?
   c. For those extracted manually, is it possible to automatize? If yes, what are the procedures to follow?

2) Determine indicators derived from UAV 3DPC for Rockfall Susceptibility Assessment:
    a. Which methods available in the literature for Rockfall Susceptibility Assessment can be adapted to use features extracted from the 3DPC?
    b. Which indicators can be developed using the extracted features from 3DPC?
    c. How can these indicators be quantified in a reproducible way?
3) Develop an index for Rockfall Susceptibility Assessment combining the chosen indicators:
    a. What is the weight of each indicator?
    b. How can the output of this index be classified?
    c. How can this index be fed back in the 3DPC, showing areas with different susceptibility levels?
    d. How to calibrate and validate this index with data collected in the study area?
    e. What are the assumptions and limitations to apply this index in other study areas?

1.5. Thesis Outline

This thesis is structured in the following chapters:

Chapter 1: Background information of Rockfall Susceptibility and Hazard Assessment, including the conceptual framework of its elements (susceptibility, magnitude, intensity, propagation, and frequency - Figure 1-1) and how it has developed over time. An overview of the recent applications of remote sensing techniques for rock mass characterization and its application to rockfall studies is briefly described. Afterward, it proceeds with the identified research problem followed by the main research objective and its related questions addressed in this work.

Chapter 2: Literature review of rock mass characterization and the conceptual framework adopted in this thesis (Figure 2-1), including the basic terminology of geomechanical properties. Additionally, a review of the rock mass classification system RMR and slope stability SMR index, as well as the previous works applying 3DPC for Rockfall Susceptibility Assessment.

Chapter 3: Description of the geographic location of the study area, geological settings in terms of lithologies and macro structures present in the surroundings based on literature and local description of the studied rock slope in terms of size, lithology, joint set system, weathering, and failure mechanism.

Chapter 4: The methodological framework is presented (Figure 4-1) where the 4 sequential blocks are briefly described: UAV photogrammetry, feature extraction, slope stability, and rockfall susceptibility assessment. Each block has a dedicated section with a step by step procedure of approaches and methods taken, limitations, inputs, and outputs for each step and software used.

Chapter 5: Application of the methodology in the studied rock slope and results obtained for feature extraction, slope stability, and rockfall susceptibility assessment. In this latter, the proposed Rockfall Susceptibility Index (final output) is applied on the 3DPC of rock slope.

Chapter 6: Discussion of the results of the Rockfall Susceptibility Index, including validation, potential, and limitations. An explanation of the lack of uncertainties is also presented.

Chapter 7: Summary of the main findings of this study including the answers to the research questions and suggestions for further improvements.

2. LITERATURE REVIEW

2.1. Rock mass characterization

Wherever excavation and construction in rocks take place, the characterization of a rock mass is of primary importance since all the design and further implementation of an engineering project will heavily depend on this initial step (further explained in Section 2.2). Thus it is relevant to clarify some basic terminology used in rock mechanics and engineering that will also be often cited in this thesis.

In simple terms, rock mass is a system composed of intact rock blocks separated by discontinuities, in which all the elements influence as a unit the mechanical behaviour of this system (Palmström, 2001). The process of giving quantitative description to rock mass elements either through observation or measurement constitutes the rock mass characterization (Palmström, 2001).

The two elements of a rock mass, i.e. discontinuity and intact rock blocks have their characteristics and particularities (Figure 2-1). Intact rock blocks, also known as rock materials, are the smallest element not cut by any discontinuity (Singh & Goel, 2011b). They have physical characteristics such as mineralogy and chemical composition, texture, color, grain size, shape, and porosity as well as mechanical characteristics such as strength, hardness, plasticity, and brittle behaviour.

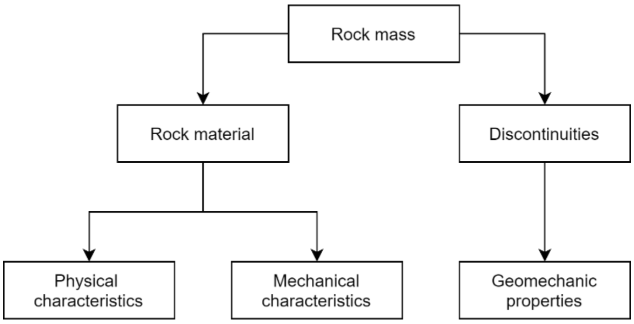

Figure 2-1. Conceptual framework of rock mass adopted in this thesis. Source: modified from Singh & Goel (2011b). Rock material characteristics are not addressed in this work.

Discontinuities are surfaces of weakness that cut the rock mass and as a result, produce intact rock blocks in between. This is a broader term that includes all the following types of discontinuities according to ISRM (1978): joints, weak bedding planes, weak schistosity planes, weak zones, and faults. For the scope of this thesis, joints and bedding planes are the most common type of discontinuity in the studied area and thus deserves a further explanation:

Joints: a break of geological origin in the rock mass where no visible displacement took place (ISRM, 1978). A group of joints that are parallel constitutes a joint set and a rock mass can have more than one intersecting joint set, which is called a joint system. Joints are formed due to various tensile stress a rock is submitted to such as thermo-elastic strain due to heating and cooling of exposed rock surfaces and chemical weathering resulting in mineralogical alteration (contraction and expansion) within the rock fabric (Slob, 2010).

Bedding planes: layers of sedimentary rocks formed in a horizontal surface due to deposition and lithification of sediments in the geologic time. These layers reflect the conditions of sedimentation taking place in the environment (lake, river, estuary, ocean) in terms of climate and energy of transport and thus imply difference in grain size, shape, and mineralogy. Once the layers are lithified, in other words, become part of a sedimentary rock, tectonic process can cause faults and folding to tilt the layers. In this scenario, they are no longer horizontal.

From this point onward, the term joint will be used as a synonym for discontinuity, unless stated otherwise. The main geomechanical properties of joints used in this thesis are the number of sets, orientation, spacing, persistence, roughness, aperture, infilling, block size and are described according to ISRM (1978):

1. **Number of sets**: number of joint sets composing the joint system. It is also possible to have random joints intersecting the rock mass which do not belong to any joint set.
2. **Orientation**: describes by the orientation relative to the magnetic north (dip direction) and the dip of the line with the steepest inclination in the plane of a joint (dip angle). Example: 210°/10°, where 210° is the dip direction and 10° the dip angle.
3. **Spacing**: normal (perpendicular) distance of adjacent joints. Within a joint set, the spacing is often regular and the average is referred to as set normal spacing (Figure 2-2a).

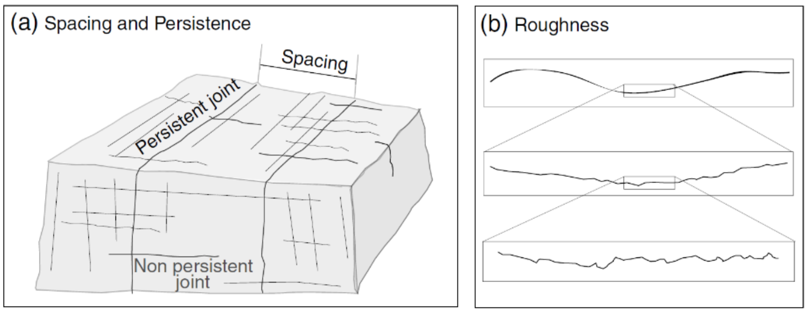

Figure 2-2.(a) 3D rock mass with persistence and spacing. (b) 2D joint profiles on different scales with roughness. Source: Abellán et al., (2014)

4. **Persistence**: size of a joint in terms of area of exposed surface or as a line, also referred to as trace length. The persistence can be terminated in solid rock, by intersecting another joint or also due to rock bridges, i.e parts of intact rock in the joint surface (Figure 2-3). In these scenarios it is called non-persistent joint, i.e. do not have a large extension. In an opposite scenario, where it has a large extension it is referred to as persistent joint (Figure 2-2a).

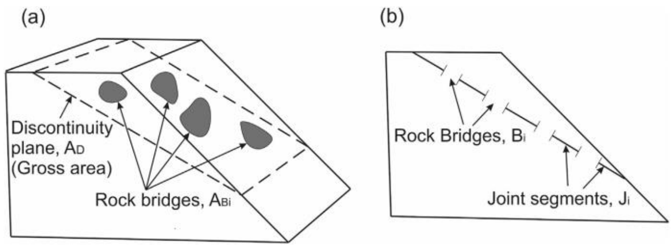

Figure 2-3. (a) 3D Rock slope with a discontinuity plane containing rock bridges. (b) Profile of the slope where the discontinuity is interrupted by the rock bridges, originating joint segments (i.e trace length). Source: Shang et al. (2018).

5. **Roughness**: surface waviness or roughness of the joint plane (Figure 2-2b). The two main classification systems are from ISRM (1978) – Appendix C or Joint Roughness Coefficient (JRC) from Barton & Choubey (1977) – Appendix D.
6. **Aperture**: perpendicular distance between adjacent rock walls of a joint. The space between this rock wall is only air or water.
7. **Infilling**: when instead of air or water (no infilling), the aperture is filled with material usually weaker than the rock material. Examples are sand, silt, clay, breccia, gouge, thin mineral coating, quartz, and calcite veins.

8. **Block size**: block rock dimensions defined in terms of normal set spacing and orientation of intersecting joint sets (Section 4.2.4). Larger spacing between joints will often result in bigger block volumes.

In addition to the above mentioned joint set characteristics, there is also the concept of overhanging. It is the surface of a joint below a block of rock with no continuation of rock mass due to failure mechanism and erosion. The presence of overhanging implies that the portion of rock above the overhanging lacks support and as a consequence is more susceptible to rockfall (Figure 2-4).

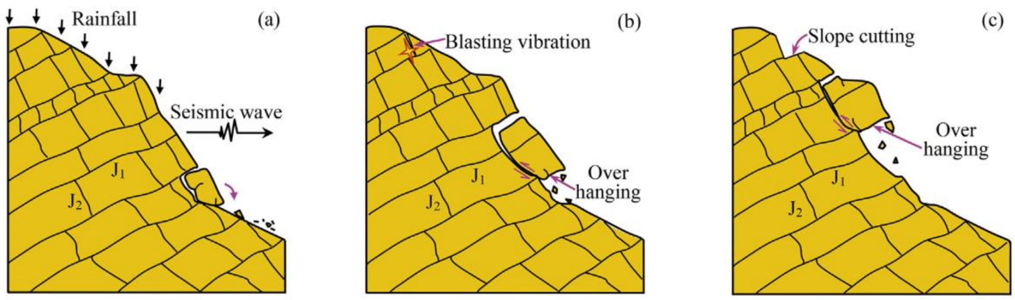

Figure 2-4. Progressive rockfall caused by failure mechanisms in a rock mass. (a) Rockfall induced by rainfall and seismic wave generates a lack of support in the base of the rock mass (overhanging-J_1). Blasting vibration (b) and slope cutting (c) causes rockfall above of the overhanging. Source: H. Li et al (2019).

2.2. Rock mass classification

Rock mass classification systems are schematic ways to zonate a rock mass in different compartments based on their geomechanical properties and as a consequence, their mechanical behaviour (i.e strength and deformability) (Bieniawski, 1973). It is commonly applied in the planning and design stages of a complex engineering project involving rock mass when only a conventional site characterization is available to describe the rock mass (Hoek, 2007). These classifications systems provide a quantitative data as input for real engineering problems such as to estimate the support requirement for excavation as well as to facilitate the communication among the technicians involved on the project (engineers, geologist, designer, contractor) by giving common grounds and terminology (Bieniawski, 1973).

Rock engineers and geologists have gathered experience over 100 years in underground works or rock slopes in different sites to develop these classification systems (Hoek, 2007). Throughout this period, it has been successfully applied in design stages in Austria, South Africa, United States, Europe, and India on projects related to hydroelectric power plants, bridges, caverns, tunnels, silos, building complexes, rail tunnels and hill roads (Singh & Goel, 2011a).

Some of the common rock mass classification systems are the Rock Quality Designation (RQD), Rock Tunnelling Quality Index (Q), Rock Mass Rating (RMR), Slope Mass Rating (SMR), and Geological Strength Index (GSI). Each one has its limitations, applicability for a particular scenario (weak or good rock mass for instance), and emphasizes a particular set of geomechanical properties (i.e. different weights) (Hoek, 2007). For the scope of this thesis, the RMR and SMR are briefly described.

2.2.1. Rock Mass Rating System

One of the most worldwide used classification systems in rock engineering is the Rock Mass Rating (RMR) system. It was originally named Geomechanical Classification and developed by (Bieniawski, 1973) based on his own experience on tunnelling in South Africa, on a detailed study of all the available classification system at that time and also based on discussion with world specialists in the field. The primary purpose of RMR is to use geomechanical parameters of a jointed rock mass to divide it into different zones in terms of strength (or quality). This zonation into good or low-quality rock mass allows rock engineers to appropriately design tunnelling support systems for each zone and the excavation approach. Since the original publication, some readjustments have been proposed to the RMR throughout the years and nowadays one of the most used version is of Bieniawski (1989) (as cited in Hoek, 2007, p. 70), where the following parameters are considered: Uniaxial compressive strength of rock material, Rock Quality Designation (RQD), Spacing of discontinuities, Condition of discontinuities, Groundwater conditions, Orientation of discontinuities

These six parameters are classified into ranges (Table 2-1.A,B,E) and summed to provide the RMR value, which lies into 5 categories in decreasing level of rock mass strength (or quality): class I – very good rock to class V – very poor rock (Table 2-1.C). Based on the class, specific excavation methods and support systems are recommended.

Table 2-1. Rock Mass Rating System after Bieniawski (1989). Source: modified from Hoek (2007).

A.Classification Parameters and rating

<table>
<tr><th colspan="3">Parameter</th><th colspan="7">Range of values</th></tr>
<tr><td rowspan="3">1</td><td rowspan="2">Strength of intact rock material</td><td>Point-load strength index</td><td>>10 MPa</td><td>4 - 10 MPa</td><td>2 - 4 MPa</td><td>1 - 2 MPa</td><td colspan="3">For this low range - uniaxial compressive test is preferred</td></tr>
<tr><td>Uniaxial comp. strength</td><td>>250 MPa</td><td>100 - 250 MPa</td><td>50 - 100 MPa</td><td>25 - 50 MPa</td><td>5 - 25 MPa</td><td>1 - 5 MPa</td><td>< 1 MPa</td></tr>
<tr><td colspan="2">Rating</td><td>15</td><td>12</td><td>7</td><td>4</td><td>2</td><td>1</td><td>0</td></tr>
<tr><td rowspan="2">2</td><td colspan="2">Drill core Quality RQD</td><td>90% - 100%</td><td>75% - 90%</td><td>50% - 75%</td><td>25% - 50%</td><td colspan="3">< 25%</td></tr>
<tr><td colspan="2">Rating</td><td>20</td><td>17</td><td>13</td><td>8</td><td colspan="3">3</td></tr>
<tr><td rowspan="2">3</td><td colspan="2">Spacing of</td><td>> 2 m</td><td>0.6 - 2 . m</td><td>200 - 600 mm</td><td>60 - 200 mm</td><td colspan="3">< 60 mm</td></tr>
<tr><td colspan="2">Rating</td><td>20</td><td>15</td><td>10</td><td>8</td><td colspan="3">5</td></tr>
<tr><td rowspan="2">4</td><td colspan="2">Condition of discontinuities (See E)</td><td>Very rough surfaces
Not continuous
No separation
Unweathered wall rock</td><td>Slightly rough surfaces
Separation < 1 mm
Slightly weathered walls</td><td>Slightly rough surfaces
Separation < 1 mm
Highly weathered walls</td><td>Slickensided surfaces
or Gouge < 5 mm thick
or Separation 1-5 mm
Continuous</td><td colspan="3">Soft gouge >5 mm thick
or Separation > 5 mm
Continuous</td></tr>
<tr><td colspan="2">Rating</td><td>30</td><td>25</td><td>20</td><td>10</td><td colspan="3">0</td></tr>
<tr><td rowspan="4">5</td><td rowspan="3">Groundwater</td><td>Inflow per 10 m tunnel length (l/m)</td><td>None</td><td>< 10</td><td>10 - 25</td><td>25 - 125</td><td colspan="3">> 125</td></tr>
<tr><td>(Joint water press)/ (Major principal σ)</td><td>0</td><td>< 0.1</td><td>0.1, - 0.2</td><td>0.2 - 0.5</td><td colspan="3">> 0.5</td></tr>
<tr><td>General conditions</td><td>Completely dry</td><td>Damp</td><td>Wet</td><td>Dripping</td><td colspan="3">Flowing</td></tr>
<tr><td colspan="2">Rating</td><td>15</td><td>10</td><td>7</td><td>4</td><td colspan="3">0</td></tr>
</table>

B. Rating adjustment for discontinuity orientation

<table>
<tr><th colspan="2">Strike and dip orientations</th><th>Very favourable</th><th>Favourable</th><th>Fair</th><th>Unfavourable</th><th>Very Unfavourable</th></tr>
<tr><td rowspan="3">Ratings</td><td>Tunnels & mines</td><td>0</td><td>-2</td><td>-5</td><td>-10</td><td>-12</td></tr>
<tr><td>Foundations</td><td>0</td><td>-2</td><td>-7</td><td>-15</td><td>-25</td></tr>
<tr><td>Slopes</td><td>0</td><td>-5</td><td>-25</td><td>-50</td><td></td></tr>
</table>

C. Rock mass classes determined from total rating

Rating	100 ← 81	80 ← 61	60 ← 41	40 ← 21	< 21
Class number	I	II	III	IV	V
Description	Very good rock	Good rock	Fair rock	Poor rock	Very poor rock

E. Guidelines for classification of discontinuity conditions

Discontinuity length (persistence) Rating	< 1 m 6	1 - 3 m 4	3 - 10 m 2	10 - 20 m 1	> 20 m 0
Separation (aperture) Rating	None 6	< 0.1 mm 5	0.1 - 1.0 mm 4	1 - 5 mm 1	> 5 mm 0
Roughness Rating	Very rough 6	Rough 5	Slightly rough 3	Smooth 1	Slickensided 0
Infilling (gouge) Rating	None 6	Hard filling < 5 mm 4	Hard filling > 5 mm 2	Soft filling < 5 mm 2	Soft filling > 5 mm 0
Weathering Ratings	Unweathered 6	Slightly weathered 5	Moderately weathered 3	Highly weathered 1	Decomposed 0

RMR can also be used to estimate other rock mass properties such as cohesion and angle of internal friction, average stand-up time for an arched roof, modulus of deformation and shear strength (Singh & Goel, 2011a). A novel application was carried out by Li et al. (2019) in the excavation of a drill-and-blast tunnel in China. The authors developed a comprehensive method for automatic characterization of rock mass in 3DPC (either from TLS or camera photogrammetry) in terms of discontinuity orientation, spacing, trace length, persistence, roughness, and aperture. The results were then applied to calculate RMR (and GSI) in the front of excavation as an alternative to the traditional manual discontinuity mapping.

2.2.2. Slope Mass Rating System

Romana (1985 as cited in Romana et al., 2015, p. 3) developed adjustment ratings empirically determined to the RMR parameters to use it for a preliminary evaluation of slope stability since this latter was created for assessing rock mass quality of underground excavation (i.e tunnels). Later on, Romana (1993) proposed a new geomechanical classification for rock slopes based on this adjustment factor, the Slope Mass Rating (SMR):

$$SMR = RMR_b + (F_1 \ x \ F_2 \ x \ F_3) + F_4 \qquad (1)$$

Where, RMR_b is the basic parameters of discontinuities A1 to A5 (Table 2-1.A,E) and F_1 to F_4 are the adjustment factors as follows (Romana, 1993):

F1: express the angular relationship between the dip direction of a joint and dip direction of the slope (Figure 2-5). The range is from 1.00, when they are near parallel (almost 0° angle between), to 0.15 when the angle between is greater than 300° (Table 2-2.A).

F2: express the joint dip angle in a planar failure mode (Figure 2-5). The range is from 1.00, when the angle is 45°, to 0.15 when it is less than 20° (Table 2-2.A). In other words, it shows the joint shear strength. For a toppling failure mode, its value is 1.00.

F3: express the angular relationship between the dip angle of a joint and dip angle of the slope (Figure 2-5). For a planar failure mode, it reflects the probability of a joint to intersect the slope as to come out of the rock mass (a term known as '*daylight*', being exposed). When the angular difference is almost 0° (near parallel joint to slope), a more stable condition is reached whereas for angular difference greater than 10° the slope is unstable. The range of values is from 0 to – 60 (Table 2-2.A). For toppling failure mode, unfavourable and very unfavourable situation cannot occur since sudden failure is rare, and toppled slopes can frequently remain standing.

F4: accounts for the method of excavation on the slope, in the following decreasing order of stability (Table 2-2.B): natural slopes, pre splitting, smooth blasting, normal blasting or mechanical excavation, and deficient blasting.

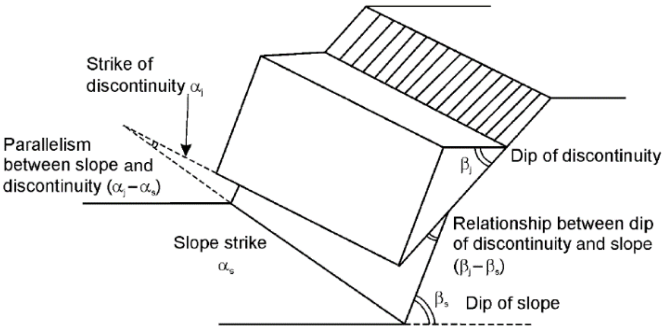

Figure 2-5. Planar failure mechanism and angular relationships between discontinuity (joint) and slope orientation. Dip = dip angle and Strike = dip orientation. Source: Singh & Goel (2011c).

Table 2-2. Slope Mass Rating System after Romana (1993), slightly modified.

A. Angular adjustment factors							
Relationship	Failure	Angular condition	Very favourable	Favourable	Normal	Unfavourable	Very unfavourable
Dip direction Parallelism (slope & joint)	P	$\lvert \alpha_j-\alpha_s \rvert$	>30°	30-20°	20-10°	10-5°	5°
	T	$\lvert \alpha_j-\alpha_s-180° \rvert$					
	P/T	**F_1**	**0.15**	**0.40**	**0.70**	**0.85**	**1.00**
Dip angle (joint)	P	β_j	<20°	20-30°	30-35°	35-45°	45°
	P	**F_2**	**0.15**	**0.40**	**0.70**	**0.85**	**1.00**
	T		**1**	**1**	**1**	**1**	**1**
Dip angle (slope & joint)	P	β_j - β_s	>10°	10-0°	0°	0-(-10°)	<(-10°)
	T	β_j + β_s	<110°	110-120°	>120°	-	-
	P/T	**F_3**	**0**	**-6**	**-25**	**-50**	**-60**

B. Excavation Method					
	Natural Slope	Presplitting	Smooth blasting	Blasting or mechanical	Deficient blasting
F_4	**+15**	**+10**	**+8**	**0**	**-8**

P: Planar , T: Toppling , Dip direction: α_j joint, α_s slope, Dip angle: β_j joint, β_s slope

Adjustment ratings F1 to F3 are classified into 4 categories from very favorable to stability (i.e stable) to very unfavourable to stability (i.e unstable) based on the above mention angular conditions (Table 2-2.A). The rating is then applied with F4 in Eq. (1) for SMR computation. Romana (1993) also provides a tentative description of SMR classes in terms of stability, failure mechanism, and needed support for stabilization (Table 2-3).

Table 2-3. SMR classes descriptions. Source: Romana (1993).

Class	SMR	Description	Stability	Failure	Support
I	100-81	Very good	Completely stable	None	None
II	80-61	Good	Stable	Some blocks	Occasional
III	60-41	Normal	Partially stable	Some joints or many wedges	Systematic
IV	40-21	Bad	Unstable	Planar or big wedges	Important/corrective
V	20-0	Very bad	Complete unstable	Big planar or soil-like	Reexcavation

During the last 30 years of its development, the SMR has been applied and validated in many countries, incorporated in textbooks and university curriculums on civil engineering courses and related fields, modified to fit specific applications and included in technical regulations as a quality index of slope (Romana et al., 2015). A recent application was done by Riquelme et al. (2016) using 3DPC coupled with fieldwork data to characterize slope stability by means SMR index. The joint set orientation was extracted from 3DPC derived from TLS and UAV photogrammetry and used as input for the adjustment factor calculation using the open-source SMRTool software, programmed in MATLAB by the authors. Complementary, the fieldwork data was used to calculate the RMR_b. and applied in Eq.(1) to obtain SMR index

2.3. Rockfall Susceptibility Assessment

The main objective of a rockfall susceptibility assessment is to determine areas in a rock mass (cliff or slope) that are more prone to rock detachment compared to surrounding parts. This identification will influence the follow-up analyses of the hazard assessment such as block volume estimation, rockfall simulation (trajectory, energy, rebound height) and thus is of primary importance. A variety of approaches are used to fulfill this objective depending on the scale (regional or local). For instance, at a regional scale (thousands of square meters), a morphometric approach is commonly used where the susceptible areas correspond to a given slope angle threshold or rock cliff exposure in the studied region (Fanos & Pradhan, 2018). This can lead to identifying source areas as lines for the rockfall simulation that although conservative, is not often accurate procedure since it can consider sources areas that eventually are stable and will not generate block detachment (Matasci et al., 2018). For more reliable rockfall simulation results, a more accurate characterization of the rock mass is required (Gigli et al., 2014) and lies within the local scale susceptibility assessment (hundreds of square meters).

In this context, the cm or mm accuracy and high amount of information obtained by 3DPC in recent decades have brought a new perspective for rockfall studies, starting by one of the pioneers Abellán et al (2006). They used a long-range TLS for a detailed study of a rockfall event in Vall de Nuria, Eastern Pyrenees (Spain). The problem definition stated by the authors was that the Digital Elevation Model (DEM) derived from Aerial Laser Scanning (ALS) had a coarse resolution when applied to steep slopes due to the low point cloud density, and thus less applicable for rockfall studies such as source identification and trajectory simulation. Therefore, they used TLS to obtain a higher point cloud density for manual geometrical characterization of the rock slope (joint sets orientation and volume of a detached block), source area identification of previous rockfall events and higher DEM resolution. These results were used as input for a rockfall simulation (trajectory, energy, rebound height) and the obtained trajectory was compared to the real one and also to one obtained using a coarser DEM from ALS. The conclusion was that a TLS provided a more accurate trajectory.

In the following years, applications of 3DPC derived from TLS and UAV for rockfall studies increased significantly. New approaches, algorithms and software were developed for more accurate and/or automatic characterization of rock slopes, such as joint set orientation (Riquelme et al., 2014; Slob, 2010), spacing (Slob, 2010; Riquelme et al., 2015), persistence/trace length (Guo et al., 2019; Riquelme, et al., 2018; Sturzenegger et al., 2011), roughness (Ünlüsoy & Süzen, 2020) and block volume (Buyer et al., 2020; Chen et al., 2017; Sturzenegger et al., 2011). Researchers also have used these geometrical properties for kinematic rock slope stability (Alameda-Hernández et al., 2019; Menegoni, et al., 2019; Wang et al., 2019), magnitude-frequency relationship (Olsen et al., 2015; van Veen., 2017), rockfall simulations (Sarro et al., 2018), multi-approach hazard assessment combining TLS and UAV derived data to apply in RHRS (Pérez-Rey et al., 2019) or rockfall hazard zonation in regional scale combining TLS and ALS in a 3D GIS modelling environment (Fanos & Pradhan, 2019). For the rockfall simulations, the source area of potential rock detachment which is usually defined as lines in rock slopes (and cliffs) have now the possibility to be locally refined, providing more reliable results.

Although multiple authors used features derived from 3DPC as input for rock slope stability, rockfall susceptibility and hazard assessment, few attempts have been made to identify directly on the point cloud possible source areas of rockfall susceptibility. The most 3 recent publications dealing with this research gap are Dunham et al., (2017), Matasci et al. (2018) and Zhang et al. (2019).

Dunham et al. (2017) developed the Rockfall Activity Index (RAI), a slope morphology-based index derived from TLS point cloud. Based on a simple logic tree algorithm, the authors classify the cm accurate point cloud into rock slope morphologic units, including features such as overhanging, slope angle, discontinuity spacing and mass wasting fragments (talus). Each classified unit is correlated with an estimated instability rate (a measurement of erosion) to calculate the RAI along the slope. The output is a profile of the outcrop with areas on the point cloud with different values of rockfall activity: the higher the value, the more susceptible to rockfall that area is.

According to the authors, the advantages of this method is that: (i) the only needed input is a high-resolution point-cloud (cm or mm accuracy) regardless of the remote sensing acquisition technique, including SfM and (ii) the algorithm is simple and computationally efficient and therefore can be applied in rock slopes of any size. The automatic classification of RAI was qualitatively validated with field observations in 15 sites in Alaska. However, the authors also acknowledge the following limitations: (i) the range of instability rates to be applied for each classified unit has a high degree of variability and uncertainty, and (ii) RAI does not take into consideration discontinuities geometry such as orientation (dip direction and dip angle) and persistence.

Matasci et al., (2018) developed a routine to quantify rockfall susceptibility at cliff scale in TLS 3DPC (hundreds to thousands of square meters), including overhanging portions of slopes. Their approach is based on the angular relationship between discontinuities and the orientation of local cliff surface (i.e dip angle and direction) for computation of where planar, wedge and toppling failure mechanisms are geometrically possible on the cliff. For each mechanism, the condition of overhanging slopes is incorporated. Afterward, an index is created for each failure mechanism using an equation that includes: (i) average joint set normal spacing and trace length, measured manually using virtual scanline on the point cloud, (ii) mean incident angle between the joint set and slope surface, (iii) slope angle of each joint set and (iv) angle between two joint sets for wedge failure. Finally, these failure mechanism indexes were then summed as having equal weight to provide a final rockfall susceptibility index for each point in the 3DPC. The authors validated this approach in two steep landscapes (Yosemite Valley in the USA and Mont-Blanc massif in France) and obtained a good correlation between the identified potential source areas and past rockfall sources (inventory and scars).

Zhang et al., (2019) went a step further by applying Matasci et al., (2018) routine of rockfall susceptibility on a UAV based 3DPC in an augmented reality (AU) environment. They focused on how to fill the gap between the correlation of real rock slope on the field and the rockfall susceptibility analyses done back in the computer office. The AU allows a straightforward on-site visualization of the rockfall sources area superimposed on the rock slope using a mobile device such as a table. In practical terms, this was done via a novel approach proposed by authors of edge-based tracking of the rock mass target for AU: (i) identification of prominent edges in photo-realistic rendered slope images and (ii) extracting of structural planes of the slope that best correspond to those prominent edges.

Despite these recent publications, there are still unsolved problems. The methodology proposed by Dunham et al., (2017) has not been applied for UAV derived point cloud and depends on the instability rate for the computation of RAI, which has a large degree of variability and uncertainty. Additionally, discontinuity orientation and persistence are not taken into account. Matasci et al. (2018) do not incorporate the extension of overhanging in their susceptibility indexes, which would allow distinguishing areas with a greater lack of support than others and thus an indication of a greater unstable block volume. Moreover, joint set spacing and persistence are manually measured. Zhang et al. (2019) also do not use any indicator to account for the extension of unstable block volumes.

This thesis lies within the context of the 3 above-mentioned publications providing new approaches to overcome these challenges.

3. STUDY AREA

The geographic location of the rock slope is in the broader context of Samaria Gorge National Park, in Crete (Greek Island). World's Biosphere Reserve by UNESCO in 1981, this park is located in western Crete in the southern slope of the White Mountain (Figure 3-1a), also known as Lefka Ori (S. Karagiannis & Apostolou, 2004). Tectonic activity, erosion process and karstification shaped this mountainous landscape (I. Vogiatzakis & Rackham, 2008) creating plenty of narrow, tall and vertical rock slopes, which has the Samaria Gorge as the steepest, tallest and narrowest opening (Spanos et al., 2008).

The geological setting is of high pressure-low temperature metamorphic rocks from the Plattenkalk unit overlain by the Phyllite-Quartize unit (Seidel, 2003). Regionally, the Plattenkalk unit includes the Mavri formation (Lower Liassic) in the lower part of the stratigraphic column up to the Aloides formation (Eocene) in the upper part (Manutsoglu et al., 2003) and consists mainly of cherty calcite marbles, dolomite, phyllite and a calcareous metaflysh (Seidel, 2003). A large geologic structure, an anticlinal, strikes SSW-NNE with its axis dipping to NNE (Manutsoglu et al., 2003).

Locally, the rock slope is on a road cut approximately 1620 m above mean sea level, between the entrance of the Gorge and Kallergis mountain refugee (Figure 3-1b), a place to host hikers and climbers. The rock slope is approximately 14 m height, 46 m lateral extension and is inclined 51° towards the road (Figure 3-1c). It consists of dark grey platy limestone with bedding planes of decimetres thickness and sometimes with centimetric intercalation of quartz or calcite. It has a joint system with 4 major joint sets as exposed surfaces that commonly intersect almost perpendicularly, forming cubic shaped rocks, as well as several random joints as trace length inside the rock mass. The more representative joint set is the bedding plane with the same dip as the slope surface (51°). The block fragments detached from the rock mass have a volume ranging from $0.064m^3$ to $0.001m^3$, or dimensions from 40cm to 5cm. The chemical weathering is not prominent and no seepage was observed during the fieldwork. Instead, small rockfalls constitute the main process of mass wasting, especially on overhanging areas. The detached rocks slide through the slope surface and thus planar failure mechanism occurs. Vegetation is abundant above the slope and some small bushes are present in the slope surface.

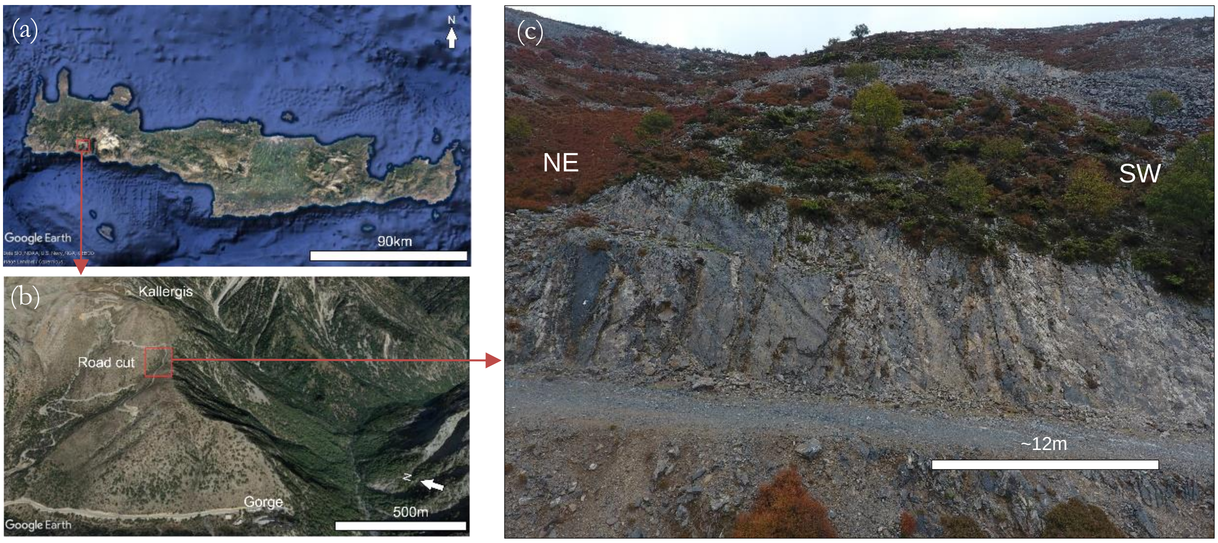

Figure 3-1. (a) Study area in red located in western Crete, Lefka Ori mountain. (b) Study area (road cut) on a road between entrance to the Gorge and Kallergis refugee. (c) UAV RGB image covering partly the rock slope. Source: (a) and (b) Google Earth.

4. METHODOLOGY

The methodological framework proposed in this thesis consists of 4 sequential blocks (Figure 4-1): (i) UAV Photogrammetry - Section 4.1, (ii) Feature Extraction – Section 4.2 (iii) Slope Stability Assessment – Section 4.3 and (iv) Rockfall Susceptibility Assessment – Section 4.4. The UAV photogrammetry deals with reconstructing the 3D model in the form of point cloud of the rock slope out of the RGB images taken by UAV in the field using SfM technique (part of image processing). The second block deals with extracting geomechanical properties/features of the 3DPC rock slope, namely the number and orientation of joint set, joint set normal spacing, persistence and block volume. In this stage, the points are first assigned to a given joint set so that the previous RBG 3DPC is now classified into different colours according to the identified joint set. Additionally, the points of rock surface are segmented into clusters that represent a joint. These clusters are the basic elements for computing the spacing and persistence for each joint set and also used for the novel semi-automatic approach proposed in this work for block volume calculation. On the Slope Stability Assessment block, the extracted features from the 3DPC as well as those obtained by field and photographs observation are rated according to the Rock Mass Rating System (RMR) as the first step to evaluate the quality of the rock mass. Afterward, the RMR score together with the angular relationship between the joint set and slope (orientation and dip) are applied for the computation of Slope Mass Rating (SMR). This is the second step to assess the slope stability kinematically. Finally, the last block provides a novel approach for visualization and integration of all the rock slopes geomechanical properties (spacing, persistence, SRM, overhanging) and stability conditions above-mentioned as indicators for a 3D Rockfall Susceptibility Assessment. For each block, a step by step procedure is given explaining the inputs, outputs and description of methods, software and approaches used.

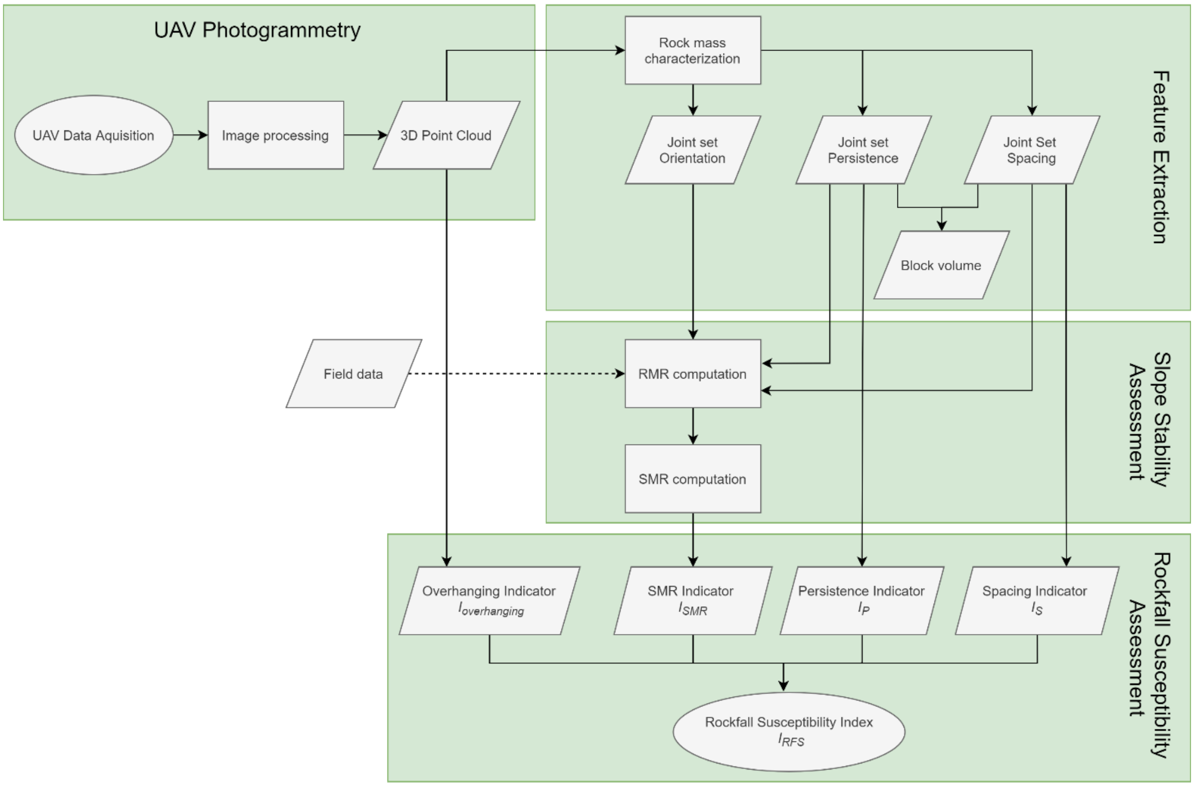

Figure 4-1. Proposed methodological framework in this thesis.

4.1. UAV Photogrammetry

4.1.1. UAV Data Acquisition

The involved data and procedure are:

Input: UAV flight to capture RGB images.

Output: RGB images of the rock slope.

The UAV data collection of RBG images was carried out using a quadrocopter DJI Phantom 4 (Table 4-1). The main procedures adopted while flying the UAV are summarized into the 2 main categories: (i) flight mode and (ii) flight height.

(i) Flight mode: manual flight in which the UAV stops in the air to take the picture and then moves to the next spot to acquire the next image, instead of taking pictures while moving. This procedure reduces the chance of having motion-blurred images. Also to avoid noise, they were acquired during a non-rainy time. Moreover, the images were acquired in oblique view of the rock slope because it enables to create a more complete 3D model (point cloud), for the given geological structure, thus avoiding occlusion. As, the flight distance from the slope face is relatively small, and the rock slope relief is abrupt, it is safer to have a manual flight rather than an automatic to avoid hitting the surface of the slope as well as, again, to minimize occlusion (areas not imaged due to view angle). This is particularly important in this case study as to capture the overhanging areas of the slope, as they are needed for the rockfall susceptibility assessment (Section 4.4)

(ii) Flight height: few meters (less than 15 m), close to the rock slope to increase the level of detail/ resolution of features to be visualized in the images. This resolution, called Ground Sampling Distance (GSD), is highly dependent on the flight height: the closer to the object (in this case the rock slope), the more centimetric features will be distinguishable in the images and possibly extracted for the rock mass characterization.

A total of 236 RGB images were acquired and after a visual quality assessment, 221 were used for image processing. The images with low contrast and/or highly blurred were not considered from this point onwards.

Table 4-1. DJI Phantom 4 technical specifications. Source: DJI, (n.d.)

Category	RGB Camera
Sensor	Effective pixel:12.4 MP 1/2.3” CMOS
Lens	FOV 94° 20 mm (35 mm format equivalent) f/2.8 focus at ∞
ISO Range	100-1600 (photo)
Image size	4000×3000 pixel
Photo format	JPEG, DNG (RAW)
Satellite Positioning Systems	GPS/GLONASS

4.1.2. Image Processing

The involved data for image processing are:

Input: RGB images of the rock slope. This is the output of UAV data acquisition (Section 4.1.1)

Output: *txt.* file of 3D points, in which each point *P* has *X,Y, Z* coordinates and RGB values

The 221 RGB images were used as input for the 3DPC generation in Pix4Dmapper version 4.3.31 (2019). This process is performed automatically by this photogrammetric software in 2 steps: (i) initial processing and (ii) 3D dense point cloud generation. Before running each step, image properties and processing parameters were user-defined as later explained. The third step in the image processing consists of vegetation removal, filtering and cropping in *CloudCompare* software (2020).

(i) Initial Processing

This step consists of image orientation. In other words, it solves the X, Y position and Z altitude of the camera and images through internal and external (relative and absolute) orientation. The internal orientation relates to the definition of camera parameters (focal length, principal point and projection center). The exterior orientation deals with relative orientation among images (relative orientation) and to georeferencing them in a known coordinates system on the real world (absolute orientation). Due to the overlap of images, common points among them are extracted as key points via image matching algorithms for further reconstruction of rock slope geometry (step iii) The main images properties and chosen processing parameters are summarized in Table 4-2.

Table 4-2. Image processing and processing parameters for the initial processing of RGB images.

Properties & Parameters	Setting
Coordinate System	WGS 84/UTM 34N (EGM 96 Geoid)
Detected template	3D Model
Keypoint image scale	Full, image scale: 1
Matching image pair	Free flight, terrestrial
Keypoint extraction	Automatic

Although no ground control points (GCP) were used in this step, the satellite positioning system in the UAV was considered to provide scale and orientation for the point cloud as well as georeferencing. Without GCP, the georeferencing accuracy is between 5 to 10 meters according to the generated Quality Report of Pix4Dmapper instead of centimeters. In this work, however, the aim is not to perform accurate surveying of the rock slope surface for hazard mitigation measures but rather the methodology to assess rockfall susceptibility in 3DPC, regardless of its accurate geographic location. Buyer et al. (2020) also did not use GCP for rock mass characterization in their study.

(ii) 3D Dense Point Cloud Generation

This step reconstructs the position and geometry of the object of interest in 3D (i.e rock slope) based on the extracted key points on the Initial Processing. The standard processing parameters where chosen (Table 4-3) to enable a faster processing time and keep a reasonable quality of the 3DPC. Moreover, setting some parameters to the higher capacity such as the full image scale does not improve the results to a significant level ("Pix4D documentation," n.d.). The generated 3DPC is in the *.las* format and its main characteristics are summarized as results in Table 4-3.

Table 4-3. Main parameters for 3DPC generation and results

	Description	Setting & Value
Parameters	Image scale	Multiscale, ½ half image size
	Point density	optimal
	Minimum # of matches	3
Results	# of 3D Densified Points	11,195,455
	Average density	22,278.00 points/m^3
	Point spacing	< 1 cm
	GSD	0.526 cm/pixel

(iii) Vegetation removal, filtering and cropping

The 3DPC in *.las* was loaded in *CloudClompare* for the manual removal of vegetation first. This is an important procedure for two reasons. Firstly it reduces the size of the file since points are eliminated and thus speeds up the processing time of feature extraction (Section 4.2). Secondly, it improves the results of joint set extraction (Menegoni et al., 2019; Riquelme et al., 2018). If points belonging to vegetation are not removed, they will be introduced in the stereogram analysis and could wrongly influence the pole density function (step ii.a – Section 4.2.1). In other words, this can cause a small swift in the orientation of maximum poles and thus also a small swift in the orientation of joint sets to be extracted.

Most of the dense vegetation was removed in the upper part of the slope but also some small bushes originated from inside the rock mas were deleted and this explains the empty areas without 3D points in the rock slope surface. After this procedure, points disconnected from the slope surface the main scene (i.e. in the air) were filtered and deleted by using *Connected Components*, applying octree level 9 (grid step = 0.101775) and minimum points per component of 5. Finally, the area of interest was cropped to remove points belonging to the road in the bottom of the rock slope and those belonging to soil and rock fragments in the surrounding. The final 3DPC contains 5,228,097 points and was converted to *.txt* file for the feature extraction.

4.2. Feature Extraction

The extracted features on the 3DPC of rock slope considered in this work are the joint set number and orientation (dip direction and dip angle), persistence, normal set spacing and block volume. They were obtained using the open-source software Discontinuity Set Extractor[1] (herein referred DSE) programmed in MATLAB by Riquelme et al., (2014). The complete methodology to derive these features (except block volume) is presented in Riquelme et al., (2014) for joint set extraction, Riquelme et al. (2015) for normal set spacing and Riquelme et al. (2018) for persistence, including validation, calibration and sensitivity analyses on the results. Therefore, the aim of this work is rather the application of these approaches for a rockfall susceptibility assessment on 3DPC.

4.2.1. Joint Set Orientation

In the DSE software, the joint set extraction is obtained semi-automatically in 3 steps following the methodology of Riquelme et al. (2014) and summarized below: (i) local curvature calculation, (ii) statistical analyses of the planes and (iii) cluster analysis.

[1] Available on http://personal.ua.es/en/ariquelme/

(i) Local curvature calculation

The data for this step are:

Input: *.txt* file of 3D points, in which each point *P* has *X,Y, Z* coordinates. This is the output of the Image Processing, and the RGB values are not needed (Section 4.1.2)

Output: *.txt* file of 3D points in which each *P(X,Y,Z)* is assigned to a subset of coplanar points with plane equation parameters (A,B,C,D) – Eq. (2)

This first step is subdivided into 3 stages: (a) nearest neighbour searching, (b) coplanarity test, (c) plane adjustment and calculation of the normal vector.

(a) **Nearest neighbour searching**: for each *P,* the nearest neighbouring points Q_i are found based on a Euclidian distance via the MATLAB algorithm *knnsearch*. The user defines the minimum number of points Q_i that will be considered.[2]

(b) **Coplanarity test**: given a point *P* and its nearest neighbouring points Q_i, this stage checks whether or not this subset of points are coplanar. This is done by Principal Component Analysis (PCA) via function *princcomp* on MATLAB. This function expresses how relevant the error associated with this subset is to form a flat surface. In other words, if the error is too large it means that the subset does not fit properly to the proposed flat surface. The threshold that indicates if this error is acceptable to define the subset Q_i as coplanar is the user-defined parameter tolerance ηmax: if a subset Q_i has a η such that $\eta > \eta max$, then this subset is rejected, otherwise if $\eta \leq \eta max$, subset Q_i is accepted as coplanar.

(c) **Plane adjustment and normal vector calculation**: once a subset Q_i is accepted as coplanar, this stage calculates the best fitting plane to all the points belonging to Q_i. This is done also by PCA, in which a plane equation for the subset is given as:

$$Ax + By + Cz + D = 0 \qquad (2)$$

Where *A, B, C* are the components of the normal vector of the plane and *D* is the position of the plane in a 3D space, relative to the origin (perpendicular distance). Therefore, each subset Q_i has a local curvature (normal vector) as exemplified by α and β in Figure 4-2.

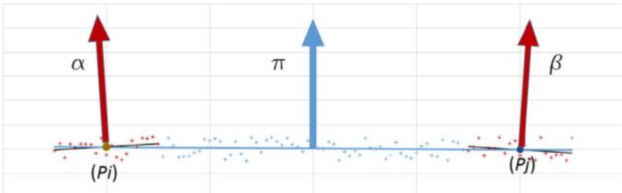

Figure 4-2. Schematic profile of a 3DPC. Point P_i has neighbouring points Q_i (left) and normal vector a whereas point P_J has Q_j as neighbouring points (right) and normal vector β. In blue is a hypothetical plane with π as normal vector representing a joint set. If a, β and π are parallel, then all the points of Q_i and Q_j are assigned to this joint set. Source: Riquelme et al. (2014).

2

(ii) Statistical analyses of the plane

For this step, the involved data are:

Input: *.txt* file of 3D points in which each $P(X,Y,Z)$ is assigned to a subset of coplanar points Q_i with plane equation parameters (A,B,C,D) – Eq. (1)

Output: *.txt* file of 3D points in which each P and its neighbouring coplanar points Q_i are assigned to a particular joint set.

This second step defines which subsets in the 3DPC are parallel and which joint set best fits them. As illustrated in Figure 4-2, if the normal vector α of subset Q_i and the normal vector β of subset Q_j has high parallelism, then they should belong to a joint set defined by a normal vector π that is also parallel to them. To achieve that, 2 main stages are performed: (a) density estimation, (b) semi-automatic set identification.

(a) **Density estimation**: first, the normal vectors of each point P and its correspondent subset Q are plotted in a stereographic projection as poles (Figure 4-3b). Then, the DSE software estimates the probability density function of poles based on Kernel Density Estimation (KDE), via function *kde2d* on MATLAB. This allows the identification of many peaks (or local maximums) of poles and their orientation in the stereogram (Figure 4-3c,d). These peaks represent the main orientations of poles (called principal poles) from all the points and their neighboring points in the 3DPC.

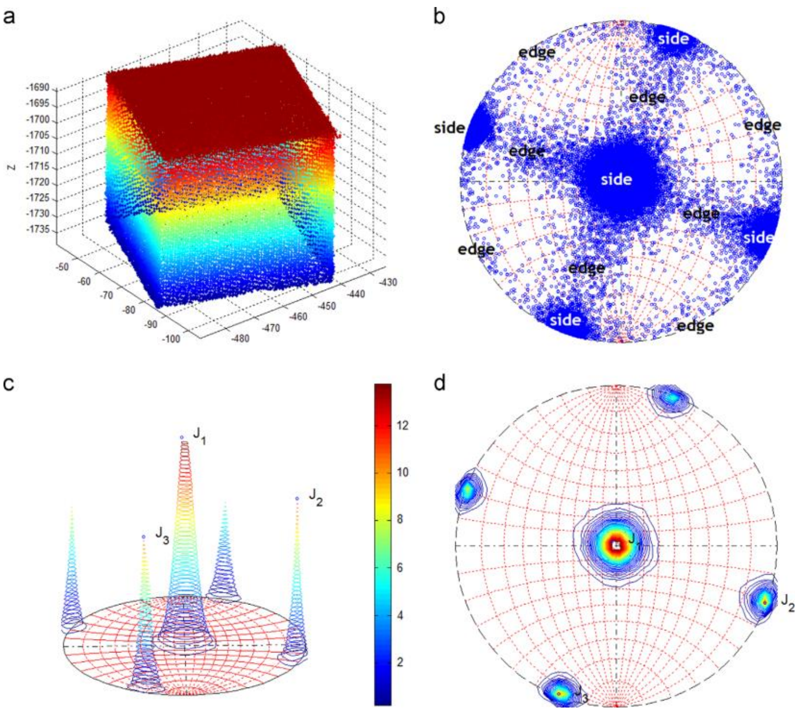

Figure 4-3 – (a) Synthetic 3DPC of a cube for illustration. (b) Representation of the normal vector pole of each point in a stereogram. (c, d) Kernel density estimation of poles in b, showing the local maximums. Source: Riquelme et al. (2014).

(b) **Semi-automatic set identification:** once the local maximums are identified, this stage first filters those local maxima with higher value which represent principal poles. This is done by two user-defined filters: the minimum angle between principal poles γ_1 and the maximum number of principal poles. The first filter γ_1 excludes the principal poles that have an angle lower than the chosen value whereas the second limits the number of principal pole to a number that represents the actual observed joint sets in the fieldwork. So far, the main principal poles of joint sets have been established. The second part of this stage assigns the pole of each point P to the closest principal point of a joint set based on a maximum angle, the cone filter γ_2 (Figure 4-4). If the angle between a pole of a point *P* and its closest joint set is greater than γ_2, this point remains unassigned.

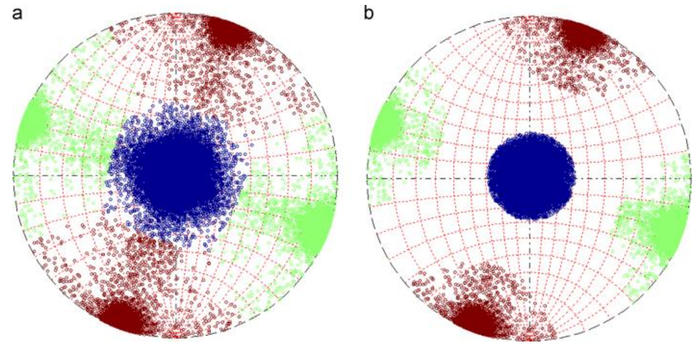

Figure 4-4. Difference in assigning poles to a joint set (blue, green or brown) if the cone filter γ_2 is used (a) or not (b). (a) All the poles of the cube in Figure 4-3b are assigned to one of the 3 main joint sets without cone filter γ_2. (b) Only those poles whose angle to the closest joint set is below γ_2 are assigned to a joint set. Source: Riquelme et al. (2014).

(iii) Cluster Analysis

Input: *.txt* file of 3D points in which each *P* and its neighbouring coplanar points Q_i are assigned to a particular joint set.

Output: *.txt* file of 3D points (X, Y, Z) in which each *P* and a group of neighbouring points of many parallel subsets *Q* are assigned to a particular joint set (JS id) and to cluster (Cl id) defined by *A, B, C, D* parameters.

This step is divided into 3 stages: (a) clustering, (b) plane generation and (c) error fitting checking.

(a) **Clustering**: the subsets of points that are parallel and belong to the same joint set are merged into one cluster. As exemplified in step (ii), the subset of points Q_i parallel to a subset of points Q_j would be merged in one cluster. This process is performed via the "Density-Based Scan Algorithm with Noise" DBSCAN develop by Ester et al., 1996 (as cited in Riquelme et al. 2014. p. 44). In the DSE software, this algorithm is implemented in a way that allows the user only to modify the minimum number of points per cluster (ppc). For one given joint set, many clusters can be generated.

(b) **Plane generation**: once a cluster is defined, this stage generates the plane equation (Eq. (2)) that best fits all the points *P* belonging to the cluster using PCA, similar to the description in step (i.c). The parameter *D* is calculated via the least square method. Every point in a cluster has the same plane equation parameters.

(c) **Error fitting checking**: this stage evaluates how well the plane fits the points of a cluster by point-plane distance and its standard deviation σ. The lower these values are, the better is the fitting.

In summary, once all the three aforementioned steps are performed via DSE software, the original RGB 3DPC becomes colourized where each colour represents one of the main joint sets. Each joint set is composed of many clusters (surfaces) defined by *A, B, C, D* parameters. Since a joint set is assumed to be composed by a group of approximately parallel joints in engineering geology (same dip direction and angle), the clusters belonging to a given joint set have all the same *A, B, C* parameters, in other words, same normal vector orientation (Riquelme et al., 2018). They differ however in the *D* parameter, unique for each cluster, reflecting their difference in position in the 3D space. This concept will be further elaborated in the joint set spacing methodology (section *4.2.3*).

The main limitation of this approach is that only the 3D points belonging to exposed surfaces of the rock slope are classified into a joint set. This implies that information of trace length is not extracted and thus not used for joint set persistence (section *4.2.2*) nor spacing analysis (section *4.2.3*). Moreover, the clusters are not planes in reality but rather surfaces with roughness and waviness (Riquelme et al., 2018).

4.2.2. Joint Set Persistence

The computation of joint set persistence is automatically performed using the DSE software given the output of the joint set extraction process as the input (section 4.2.1). The methodology described below was developed by Riquelme et al. (2018) and implemented in the DSE software (except i.a). It consists of two steps: (i) analysis of coplanarity of clusters and (ii) computation of persistence.

(i) Analysis of coplanarity of clusters

Input: *.txt* file of 3D points in which each *P (X, Y, Z)* are assigned to a particular joint set (JS id) and a cluster (cl id) defined by the plane equation parameters *A, B, C, D*. This is the output of joint set orientation (Section - 4.2.1)

Output: *.txt* file of 3D points in which each *P (X, Y, Z)* are assigned to a particular joint set (JS id) and to a cluster (cl id) defined by the plane equation parameters *A, B, C, D'*, where *D'* is modified to have the same value as its coplanar clusters.

This step consists of three stages: (a) visual assessment of persistence, (b) determination of coplanar clusters and (c) merging coplanar cluster

(a) **Visual assessment of persistence**: this assessment should be carried out to establish which joints in the rock slope are persistent or non-persistent (Riquelme et al., 2018), as to set k parameter described in stage (b). In this thesis, the approach proposed can be applied in slopes of larger extension (hundreds of meters), providing a faster way to visually evaluate the persistence condition of a joint set. It consists of the distribution of clusters in 3D space as follows:

    1. All the cluster of a given joint set should be plotted (colourized) in the 3D space, without the other joint sets. If a rock slope has 4 joint sets, for instance, each one is checked individually.
    2. Visual inspection of the cluster distribution is space. If the cluster is randomly distributed in the space and is not continuous, they are non-persistent. Otherwise, they are persistent.
    3. Distribution of all the points of a given joint set in a histogram. It is expected that for non-persistent clusters, the points should be more homogeneously distributed among the clusters. If only fewer clusters have the majority of the points of the joint set, they are most probably persistent.

(b) **Determination of coplanar clusters**: Riquelme et al. (2015) have previously determined mathematic criteria to check the coplanarity of clusters. Given cluster 1 and cluster 2, they will be coplanar if:

$$|D_1 - D_2| \leq k\ x\ (\sigma_1 + \sigma_2) \qquad (3)$$

Where σ_1 and σ_2 are the standard deviation of the normal distance of all the points to the best fitting plane of cluster 1 and 2 respectively, D_1 and D_2 are the parameter of cluster position (2), and K is the parameter that controls the sensitivity of the analysis. This inequation expresses the relationship of the standard deviation to the position in space of the clusters: if they are placed almost in the same plane so that their difference in position is smaller than the sum of their standard deviation, they will be merged and therefore considered as only one plane for the computation of persistence. This coplanarity check can only be applied if the clusters have the same parameter A, B and C (normal vector orientation).

As for k, Riquelme et al. (2018) propose the following conditions to determine its value:

$$s_{coplanar-cluster} \ll k\ x\ (\sigma_1 + \sigma_2) \ll S \qquad (4)$$

$$s_{coplanar-cluster} = |D_1 - D_2| \qquad (5)$$

Where $s_{coplanar-cluster}$ is the normal spacing of two coplanar clusters and S is the mean normal spacing of the joint set which the clusters belong to. The $s_{coplanar-cluster}$ (Eq. (4)) is the difference in the position of two cluster that should be coplanar but due to the small variations of point to plane distances have a slightly different D. This implies that k must have a value as to keep the mean normal spacing much larger compared to the standard deviation of the considered clusters.

Setting a value for k =0 makes every cluster of a joint set a unique plane not coplanar with any other cluster of that joint set (Riquelme et al., 2018), regardless of how close they might be in terms of parameter D. This situation should be used when the joints are non-persistent, in other words when they are not connected due to the presence of rock bridges (Figure 2-3) or because they are intersected with joints belonging to another set in the rock slope (Figure 2-2a).

(c) Merging coplanar clusters: the clusters identified as coplanar (3) are merged by replacing their D parameter as to be equal. This will place them in the same position in space. Furthermore, the coplanar cluster will be considered as 1 unified new merged cluster for the computation of persistence.

(ii) Computation of persistence

Input: *.txt* file of 3D points in which each *P (X, Y, Z)* are assigned to a particular joint set (JS id) and to a cluster (cl id) defined by the plane equation parameters *A, B, C, D'*, where *D'* is modified to have the same value as its coplanar clusters.

Output: *.txt* file in which each line has the identification of the merged cluster (mc id), the joint set it belongs to (JS id), the persistence in dip and strike direction (meters), max length (meters) and area of the convex hull (m^2)

In this step, two mains stages are performed: (a) calculation of rigid transformation matrix and (b) extraction of measurements.

(a) Calculation of rigid transformation matrix: this stage uses the dip angle, dip direction and normal vector of each joint set to make them become the new X', Y', Z' axis of a new coordinate system, respectively. Riquelme et al. (2018) apply the transformation matrix R as:

$$R = \begin{bmatrix} \cos(\beta)\sin(\alpha) & -\cos(\alpha) & \sin(\beta)\sin(\alpha) \\ \cos(\beta)\cos(\alpha) & \sin(\alpha) & \sin(\beta)\cos(\alpha) \\ -\sin(\beta) & 0 & \cos(\beta) \end{bmatrix} \qquad (6)$$

Where β is the dip angle and α is the dip direction of the joint set. Afterward, R is applied to every cluster of a given joint set.

(b) Extraction of measurements: in the new coordinate system (Figure 4-5), the persistence is calculated in the direction of dip (O'X'), the direction of strike (O'Y'), maximum length (O'X'Y') and in terms of area (Riquelme et al., 2018):

$$Persistence_{Dip} = \max(x) - \min(x) \quad (7)$$

$$Persistence_{Strike} = \max(y) - \min(y) \quad (8)$$

$$Persistence_{max} = \max \text{length}(C_h(MC)) \quad (9)$$

$$Persistence_{Area} = \text{area}\,(C_h(MC)) \quad (10)$$

Where min and max are the minima and maxima coordinates of a point P in the merged clusters MC either in plane OX (dip) or plane OY (strike), $\max \text{length}(C_h(P))$ is the maximum length calculated in the area of the convex hull of merged clusters, this latter being $\text{area}\,(C_h(MC))$. The convex hull is obtained in MC using the function *convhull* in MATLAB.

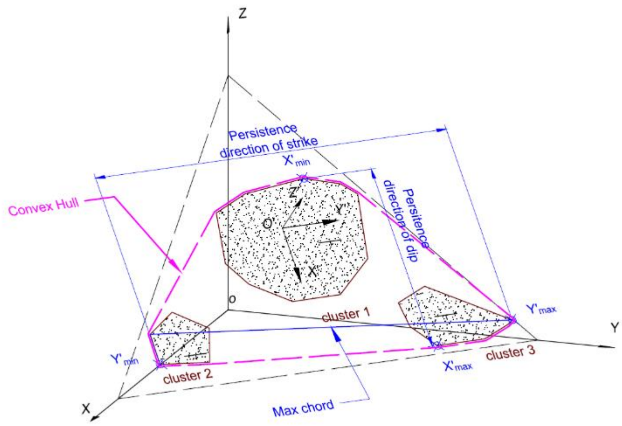

Figure 4-5. Illustration of a 3D space with 3 merged clusters in the new coordinates system O'X'Y'Z' after applying rigid transformation matrix R. The convex hull is delineated in pink and the calculated persistence in blue: direction of dip in O'X', direction of strike O'Y' and maximum length (cord) in plane O'X'Y. Source: Riquelme et al. (2018).

In summary, this process will provide at the end for every cluster (if k=0) or merged cluster (if k >0) in a joint set, the information of persistence calculated in the direction of dip, strike, maximum length and the area of the convex hull. This information is not plotted in the 3D space, therefore visualization is not straightforward. In Section 4.4, an improvement in the methodology will be presented useful not only for visualization but also as an indicator for rockfall susceptibility assessment.

As previously stated, the fact that only exposed surfaces are extracted as joints (clusters as planes) no information of trace length (lines) is available for persistence computation.

4.2.3. Joint Set Spacing

An algorithm developed by Riquelme et al. (2015) and implemented in the DSE software allows the automatic normal spacing calculation given the output of the joint set extraction process (section 4.2.1) as the input. This methodology can be briefly described visually and afterward explained in terms of the proposed algorithm by the authors.

Visual representation

The main assumption is that the clusters of a given joint set are parallel and consequently have the same *A, B, C* parameters (normal vector orientation). The parameter D is different however for each cluster of that joint set as it represents the position of the cluster (joint) in space. If the clusters are considered as persistent joints (Figure 4-6a), they are infinite planes that intersect a perpendicular virtual scanline at a given point. Then the distance of these intersecting points is calculated as the normal spacing between clusters (Riquelme et al., 2015). If the cluster is considered as non-persistent joint (Figure 4-6b), no virtual scanline is taken into account and the perpendicular distance between the closest cluster is computed as the normal spacing. In Figure 4-6 for instance, for the first scenario (persistent), the normal spacing is calculated from cluster 1 to cluster 2 (8,1 units) whereas for the second scenario (non-persistent), the normal spacing from cluster 1 is to cluster 3 (31.7 units) and from cluster 2 to cluster 4 (29,9 units). These individual differences reflect in the mean normal spacing for all the cluster of a joint set, in other words, the joint set normal spacing: for a persistent scenario, the joint set normal spacing is 16,28 units whereas for the non-persistent scenario it is almost twice as large, 27,16 units (Riquelme et al., 2015).

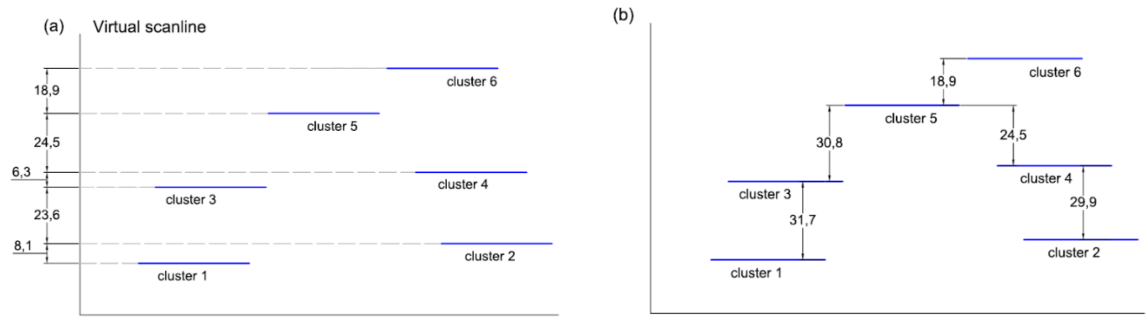

Figure 4-6. 2D representation of clusters (in blue) of a given joint set. (a) Normal spacing calculation considering clusters as persistent joints. (b) Normal spacing calculation considering clusters as non-persistent joints. Source: Riquelme et al. (2015).

Algorithm

Input: *.txt* file of 3D points in which each *P (X, Y, Z)* and a group of neighbouring points of many parallel subsets *Q* are assigned to a particular joint set (JS id) and a cluster (cl id) defined by the plane equation parameters *A, B, C, D*. This is the output of joint set extraction (Section 4.2.1)

Output: *.txt* file in which each line has the identification (id) of the joint set (JS id), the two clusters used for the normal spacing computation (cl 1 id and cl 2 id), the normal spacing value between them and the parameter D of each cluster (cl 1 D and cl 2 D).

Riquelme et al. (2015) have implemented this aforementioned visual description for normal spacing calculation as an algorithm with the following steps (Figure 4-7):

(i) For a given joint set, all the clusters are ascending sorted in a list *Dsorted* using their position in space (parameter D).

(ii) From the *Dsorted* list, a subset of clusters *R* is created excluding the first cluster Cl_1 and its points *P*.

(iii) For each point *P* of Cl_1, the perpendicular distance to the closest point P_i belonging to a cluster Cl_i in subset *R* is computed. This distance is the normal spacing between Cl_1 and Cl_i. If there is another point *P* of Cl_1 close to a point P_j of Cl_j , the distance is also considered as the normal spacing between Cl_1 and Cl_j. Consequently, a single cluster can have the normal spacing calculated to two or more neighbouring clusters.

(iv) Steps (ii) and (iii) are repeated for the second cluster Cl_2 in the *Dsorted* list: it is excluded from the subset of clusters *R* and the perpendicular distance to the closet point belonging to a cluster Cl_k is computed. This distance is the normal spacing between Cl_2 and C_k.

(v) When all the clusters have been used for distance calculation, the algorithm stops.

```
procedure SPACING CALCULATION
  Input: Point Cloud P=(X, Y, Z, DS id, cl id, A, B, C, D)
  Output: Spacing = (DS id, cl1 id, cl2 id, spacing, cl1 D, cl2 D)
  counter = 1
  for each joint set i do
    Pi ← P                                    ▷ P: points member of DS id i
    Pi ← Sort Pi by D parameter                     ▷ in ascending order
    Dsorted ← D values of all the points of Pi
    Dsortedid ← cluster ids of all the points of Pi
    create group R ≡ P(points members of Pi except cluster id Dsortedid(1))
    for each cluster j do
      create group Q ≡ Pi(points members of Pi and cluster id Dsortedid(j))
      Dist ← Distance from all the points of Q to all the points of R
      p ← nearest point from Q to R
      pid ← id of the cluster that contains the point p
      D1 ← D parameter of the cluster that contains the cluster id Dsortedid(j)
      D2 ← D parameter of the cluster id pid
      spacing(counter) ← [DS i, cl Dsortedid(j), pid, |D1 − D2|, D1, D2]
      create group R ≡ R(points members of R except cluster id Dsortedid(i))
      counter ← counter + 1
```

Figure 4-7. Pseudocode of the algorithm for normal spacing calculation. Source: Riquelme et al. (2015).

In summary, the normal spacing calculation in DSE software provides a list of the neighbouring cluster and the perpendicular distance between them. This distance does not depend on the location of the virtual scanline for a persistent joint set scenario since they are assumed to be parallel. In other words, it is a non-directional dependent method (Riquelme et al., 2015). Moreover, some clusters can have more than one neighbouring cluster, especially if it has a large areal extension.

As can be noticed, this approach has 2 limitations. Firstly, if some clusters in the study are not parallel, the distance between them is directionally dependent. Consequently, unrealistic values of normal spacing can be computed, greater or lower than reality (Riquelme et al., 2015). Secondly, the only joints represented by exposed surfaces in the study area are used for this computation. Joints represented by trace length inside the rock mass, and thus not exposed surfaces, are not taken into account, even though also being useful for normal spacing calculations (Riquelme et al., 2015).

4.2.4. Block volume calculation

Block volume calculation was performed using the inputs from the DSE software in two different approaches: mean block volume for rock slope and local block volume in a given area of the 3DPC.

Mean block volume

The mean block volume was estimated using the expression proposed by Palmstrom, (2005):

$$V_b = \frac{S_1 \, x \, S_2 \, x \, S_3}{sin_{\gamma 1} \, x \, sin_{\gamma 2} \, sin_{\gamma 3}} \qquad (11)$$

Where S_1, S_2, S_3 are the mean normal set spacing of the considered joint set and $\gamma 1, \gamma 2, \gamma 3$ are the angles between them (Figure 4-8). Since the joint sets in the rock slope intersect in approximately 90°, also attested by the cubic shaped of fallen blocks in the foot slope, the expression can be simplified:

$$V_b = S_1 \, x \, S_2 \, x \, S_3 \qquad (12)$$

The estimated V_b was validated with field measurements of fallen blocks using a measuring tape. This approach of considering mean normal set spacing derived from 3DPC rock mass as input for mean block volume estimation was also used in recent studies. Sarro et al., (2018) applied the obtained block volume for rockfall simulation in a cliff close to a cultural heritage site in Cortes de Pallás (Spain) and Pérez-Rey et al., (2019) in weathered granite outcrop close the small village of Chantebrito in Galicia (Spain).

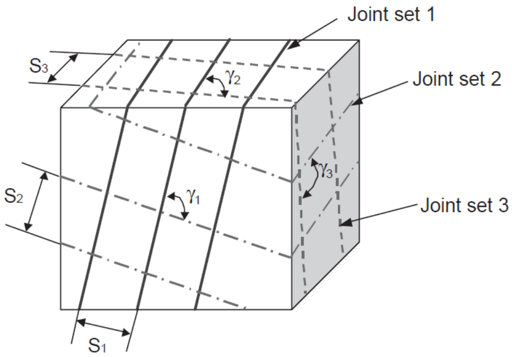

Figure 4-8. Block composed of 3 joint sets, with normal set spacing S and angle γ between them. Source: Cai et al. (2004).

Local block volume

In this work, a novel approach for estimating block volume in a particular area of 3DPC is presented. It is semi-automatic since it is based on 2 outputs obtained from DSE computation of persistence (Section 4.2.2) and normal spacing (Section 4.2.3). The block volume is estimated by multiplying the persistence of a cluster C_i as the area of convex hull $area(C_h)$ by the normal spacing S to the closest neighbouring cluster C_j:

$$V_{b,[i,j]} = \ area(C_h[C_i])\ x\ S(C_{i,j}) \qquad (13)$$

To validate this approach, the results were compared to the block volume calculated manually in the *CloudCompare:* measuring directly on the 3PDC the distance of points in the corner of a given block, and afterward multiplying to obtain the volume (Figure 4-9).

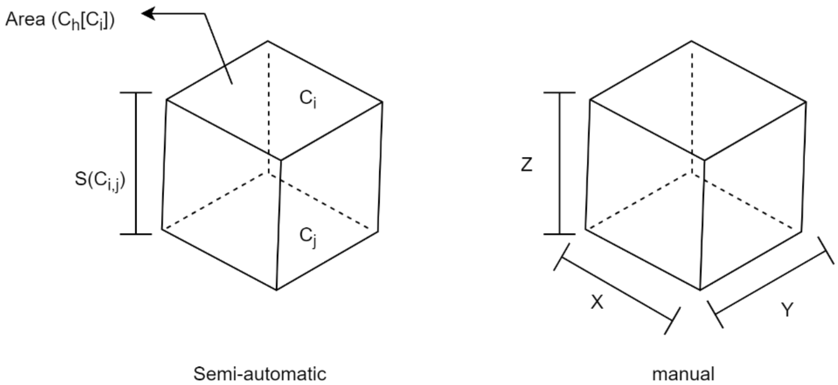

Figure 4-9. Representation of local block volume computed semi-automatically proposed in this work and manually obtained in CloudCompare. Source: own authorship.

4.3. Slope Stability Assessment

4.3.1. Rock Mass Rating

Input: a table containing for each joint set the geomechanical classification parameters (A1 to A5)

Output: a table containing for each joint set the RMR rating (0 to 100) and class (I to IV).

The assessment of rock slope quality was performed first through Rock Mass Rating (RMR) - Table 2-1, using either features extracted from the 3DPC, field observations (Appendices) or photos to obtain the five geomechanical classification parameters A1 to A5 for each joint set (Table 2-1). Parameter A2 (RQD), developed by Deere et al 1967 (as cited in Hoek, 2007, p 32) is obtained by summing the intact rock pieces longer than 100 mm in drill core logs and dividing by the total length of the core (Figure 4-10). Alternatively, it is estimated by the correlation of RQD with volumetric joint count J_V proposed by Palmstrom (2005) for cubic shape rock fragments:

$$RQD = 110 - 2.5J_V \quad (14)$$

Where the J_V is calculated as the inverse sum of (n) joint sets having each a mean joint set spacing S_n, Palmstrom (2005):

$$J_V = \frac{1}{S_1} + \frac{1}{S_2} + \cdots + \frac{1}{S_n} \quad (15)$$

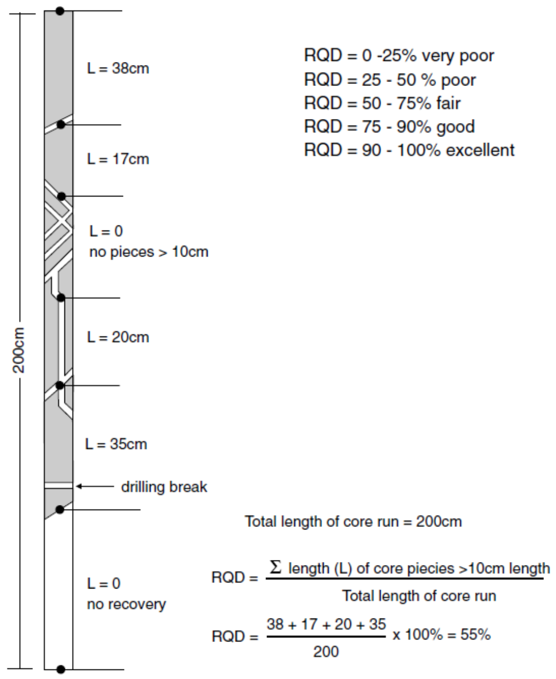

Figure 4-10. Example of RQD calculation. Source: Palmstrom (2005), slightly modified after Deere (1989).

For this case study, no drill cores were available for the calculation of RQD. Thus, this works provides another alternative to calculate the RQD directly on the 3DPC following the same procedure described by Deere et al 1967. Profiles on the slopes were selected and for each, the rock fragments exposed in the slope surface larger than 100 mm were summed and then divided by the total length of the profile. The calculated RQD was afterward validated using Eq. (14) and (15).

After establishing the five parameters, their corresponding rating was used to compute the RMR according to Bieniawski (as cited in Hoek, 2007, p.60). Even though RMR is designed to evaluate the quality of rock mass for underground excavation (i.e tunnels), it was used as an input for the Slope Mass Rating (SMR), which is properly designed to assess slope stability.

4.3.2. Slope Mass Rating

Input: a table containing for each joint set the dip direction and dip angle, RMR rating (0 to 100), auxiliary angles (*A, B, C)* and adjustment factors (F_1, F_2, F_3, F_4)

Output: table with SMR class for each joint set.

The second step to assess the rock slope stability was by means of Slope Mass Rating proposed by Romana (1993). The results of RMR rating (Section 4.3.1), the orientation of each joint set as well as the orientation of the slope (Section 4.2.1) were introduced in the *SMRTool* calculator developed by Riquelme et al (2014b) to obtain automatically the following parameters described in the section 2.2.2: auxiliary angles (A, B, C), the failure mechanism (toppling, planar or wedge) and adjustment factors (F_1, F_2, F_3,). Adjustment factor F_4 was manually introduced as a natural slope.

4.4. Rockfall Susceptibility Assessment

The DSE software allows the classification of 3DPC into joint sets, delineation of joints as planes (clusters) for each joint set, calculation of their persistence and normal spacing between neighbouring clusters. However, the normal spacing and persistence values for each cluster are given in a *.txt* file without coordinates and thus not plotted in the 3DPC for visualization. The same happens to the SMR scores calculated for each joint set using as input these geomechanical properties among others (section 4.3.2).

This thesis presents a novel approach to use these geomechanical properties for visualization in a 3D space followed by steps to integrate them as indicators for a rockfall susceptibility assessment. The final product is a methodology that can semi-automatically assess potential rockfall sources and their susceptibility to the point cloud.

In this work, for assessing the rockfall susceptibility and identifying potential rockfall sources, the following indicators are used:

- The presence of overhanging, indicating loss of support of the rock mass
- The SMR index indicating instabilities which are kinematically possible
- The joint persistence (in terms maximum length) which indicate: (i) rock mass quality and (ii) the extension of lack of support in the rock mass and thus an indication of unstable volumes: the larger the extension, the greater the volume prone to be detached.
- The joint spacing (minimum) which indicates the rock mass quality.

The sections below describe how each indicator was processed in *Excel* using the original outputs from the DSE software and combined into the Rockfall Susceptibility Index (Section 4.4.5).

4.4.1. Overhanging indicator

Input: *.txt* file of 3D points (X, Y, Z) in which each *P* is assigned to a particular joint set (JS id) and to cluster (Cl id). This is the final output of the joint set extraction process (step iii – Section 4.2.1). The parameters *A, B, C, D* are not needed.

Output: *.txt* file of 3D points (X, Y, Z) in which each *P* is assigned to a particular joint set (JS id), a cluster (Cl id) and the presence (1) of absence (0) of overhanging.

The identification of overhanging as an indicator was done manually by visual inspection of which cluster of a joint set lacks support in the rock slope RGB 3DPC and afterward transferring this information to the output file. In practical terms, this was done as follows:

(i) The first step was to overlay the clusters of each joint set on the top of the RGB 3DPC in *CloudCompare*. Then, those clusters corresponding to overhanging planes were identified by their id (Cl id).

(ii) These same clusters were selected in the input file by filtering in *Excel*, as to have all the 3D points (X, Y, Z) of these clusters also selected (each line = one 3D point). A new column was created and the value of 1 (true) was given to all these lines of the selected clusters which represent an overhanging. To all the other clusters that do not represent overhangs a value of 0 (false) was given.

(iii) Finally, for visualization, the output *.txt* file is opened in *CloudCompare* where the column of overhanging (0 or 1) is selected as a *scalar field*.

4.4.2. Persistence Indicator

Input_#1: *.txt* file in which each line has the identification of the merged cluster (mc id), the joint set it belongs to (JS id), the persistence in dip and strike direction in meters, max length in meters and area of the convex hull (m^2). This is the output from the persistence computation (step ii – Section 4.2.2)

Input_#2: 3D points (X, Y, Z) in which each *P* is assigned to a particular joint set (JS id), a cluster (Cl id) and the presence (1) of absence (0) of overhanging. This is the output of overhanging indicator (Section - 4.4.1)

Output: 3D points in which each *P* is assigned to a particular joint set (JS id), a cluster (Cl id), the presence (1) of absence (0) of overhanging and persistence as maximum length (Persis. Max).

The first step is to choose in input_#1 which of the 4 values of persistence (dip, strike, maximum length, area) of a cluster to use for the rockfall susceptibility assessment. As expressed in the rating of persistence for the RMR (Table 2-1), joints with higher persistence have a lower rating for the RMR and so contribute towards a poorer quality rock mass as well as for a greater lack of support in the overhanging, favouring rock detachment. To account for a conservative scenario, the maximum length of persistence was selected. The degree in which this assumption is conservative or realistic has to be verified by observation of the study site in situ on virtually on the point cloud.

The second step is to assign this chosen persistence to all the 3D points (X, Y, Z) of that cluster for a given joint set. As an illustration, suppose a given joint set JS_1 has a total number of clusters Cl_n and a cluster Cl_1 has numbers of 3D Points P_n. If the persistence of Cl_1 is 20 m, then the value of 20 is given to all P_n. In practical terms, this is done in the following procedure:

(i) Opening the input_#2 in *Excel* and filtering out the joint set by each cluster so that only the cluster Cl_1 and its 3D points P_n is selected. Then the persistence (20) of Cl_1 in input_#1 is copied and pasted in a new column to all the lines of Cl_1 in input_#2, (each line = one 3D point X, Y, Z of Cl_1). This new column will have the persistence information

(ii) The process in (i) is repeated, sorting out the next cluster Cl_2 in input_#2 of a joint set and pasting in the new column of all its lines the persistence of Cl_2 from input_#1. After all the C_n clusters have their correspondent persistence values in input_#2, the process stops for that joint set.

(iii) Then process (i) and (ii) restarts for all the cluster of the next join set JS_2. After all the clusters from all the joint sets have their corresponded persistence in input_#2, the process ends.

(iv) Finally, for visualization, the output *.txt* file is opened in *CloudCompare* where the column of persistence (Persis. Max) is selected as a *scalar field*.

4.4.3. Spacing Indicator

Input_#1: *.txt* file in which each line has the identification (id) of the joint set (JS id), the two clusters used for the normal spacing computation (cl 1 id and cl 2 id), the normal spacing value between them and the parameter D of each cluster (cl 1 D and cl 2 D). This is the output from the normal spacing computation (Section 4.2.3)

Input_#2: *.txt* file of 3D points in which each *P* is assigned to a particular joint set (JS id), a cluster (Cl id), the presence (1) of absence (0) of overhanging and persistence as maximum length (Persis. Max). This is the output from the persistence indicator (Section - 4.4.2).

Output: *.txt* file of 3D points (X, Y, Z) in which each *P* is assigned to a particular joint set (JS id), a cluster (Cl id), the presence (1) of absence (0) of overhanging, a persistence as maximum length (Persis. Max), and the minimum normal spacing (Spac. Min).

In input_#1, a cluster can have more than one normal spacing value if it has more than one neighbouring cluster (step iii of Spacing calculation algorithm – Section 4.2.3). As an illustration, suppose that Cl_1 has the normal spacing S computed to 3 other cluster Cl_2, Cl_5 and Cl_7 such that the values are S_{12} =X, S_{15} =3X and S_{17}=5X. The first step is to choose which value of spacing to use for the rockfall susceptibility assessment. Differently from persistence, the less spacing between joints favour a poor rock mass quality (Table 2-1). Thus, as to account for a conservative scenario, the smallest spacing was used. For the illustration, it would then be S_{12} =X. A realistic result to exemplify this idea will be later presented in Section 5.3.2.

The second step is to assign this chosen normal spacing to all the 3D points (X, Y, Z) of that cluster for a given joint set. This is a similar procedure as described for the second step of the persistence indicator (i, ii and iii), being the only difference a new column for spacing is created (Spac. Min). Finally, for visualization, the output *.txt* file is opened in *CloudCompare* where the column of spacing (Spac. Min) is selected as a *scalar field*.

4.4.4. SMR indicator

Input_#1: table with SMR class for each joint set. This is the output from Slope Mass Rating (Section 4.3.2)

Input_#2: *.txt* file of 3D points (X, Y, Z) in which each *P* is assigned to a particular joint set (JS id), a cluster (Cl id), the presence (1) of absence (0) of overhanging, a persistence as maximum length (Persis. Max), and the minimum normal spacing (Spac. Min).

Output: *.txt* file of 3D points in which each *P* has a particular joint set (JS id), a cluster (Cl id), the presence (1) of absence (0) of overhanging, persistence as maximum length (Persis. Max), the minimum normal spacing (Spac. Min) and the SMR class (SMRc)

The procedure here is to assign the SMR class of each joint set to all its clusters and corresponded 3D points (X, Y, Z), similarly as it was done for the persistence and spacing indicator, slightly simpler. As an illustration, suppose a given joint set JS_1 has a total number of clusters Cl_n and a cluster Cl_1 has numbers of 3D Points P_n. If JS_1 is class I(1), then to all the Cl_n cluster the value of 1 will be given. It is simpler because it does not require the filtering per cluster, only per joint set since all its cluster will have the same value. In practical terms, this is done as follows:

(i) opening the input_#2 in *Excel* and filtering out each joint set individually. In this way, all the clusters (and 3D Points) of this first JS_1 will be selected.

(ii) Then, the SMR Class value (1) in input_#1 is copied and pasted in a new column to all the selected lines of JS_1 in input_#2 (each line = one 3D point X, Y, Z of a cluster). After all the C_n clusters of a JS_1 have the same SMR class value (1) in input_#2, the process stops for this joint set.

(iii) The process restarts for the next joint set JS_2. After all the clusters from all the joints set have their corresponded SMR class values in input_#2, the process ends.

(iv) Finally, for visualization, the output *.txt* file is opened in *CloudCompare* where the column of SMR class (SMRc) is selected as a *scalar field.*

In summary, at the end of the aforementioned steps for all the indicators, the final output is a *.txt* file (Figure 4-11) in which each cluster and its 3D points have its information of spacing, persistence, SMR and overhanging (or not). The advantage of this approach is that it is localized information in 3D space, where no interpolation of values is performed. Moreover, it is also similar to the approach of Riquelme et al. (2014) where the original 3DPC is used from the beginning and throughout all the process as new information is added as a column, without the need for mesh generation (interpolation). The only indicator that can be said to be an averaging is the SMR because all the clusters of a given joint set have the same value, differently from spacing, persistence and overhanging which are per cluster. Even in this case, a careful evaluation using fieldwork observation is done to be as much realistic as possible (further explained in section 5.2).

	A	B	C	D	E	F	G	H	I
1	x	y	z	JS id	cl id	overhang.	Persi. Max	Spac. Min.	SMRc
2	766197	3912555	1510.77	2	1	0	2.56	0.41	1
3	766197	3912555	1510.76	2	1	0	2.56	0.41	1
4	766197	3912555	1510.76	2	1	0	2.56	0.41	1
5	766197	3912555	1510.77	2	1	0	2.56	0.41	1
6	766197	3912555	1510.75	2	1	0	2.56	0.41	1
7	766197	3912555	1510.76	2	1	0	2.56	0.41	1
8	766197	3912555	1510.75	2	1	0	2.56	0.41	1
9	766197	3912555	1510.77	2	1	0	2.56	0.41	1
10	766197	3912555	1510.76	2	1	0	2.56	0.41	1
11	766197	3912555	1510.76	2	1	0	2.56	0.41	1
12	766197	3912555	1510.75	2	1	0	2.56	0.41	1

Figure 4-11. Screenshot of .txt file in Excel containing the information of 3D points of the rock slope in this case study. It shows partially some of the 3D points (11 out of 4.420) of joint set 2, cluster 1, that is not an overhanging (0), has a maximum persistence of 2.56 m, minimum spacing to other clusters of 0.41 m and was classified as SMR class 1 (completely stable).

4.4.5. Rockfall Susceptibility Index

Input: *.txt* file of 3D points (X, Y, Z) in which each P is assigned to a particular joint set (JS id), a cluster (Cl id), the presence (1) of absence (0) of overhanging, persistence as maximum length (Persis. Max), the minimum normal spacing (Spac. Min) and the SMR class (SMRc). This is the output SMR indicator, shown in Figure 4-11 (Section 4.4.4).

Output: *.txt* file of 3D points (X, Y, Z) in which each P is assigned to a particular joint set (JS id), a cluster (Cl id), a persistence indicator (I_P), spacing indicator (I_S), the SMR indicator (I_{SMR}), overhanging indicator ($I_{Overhanging}$) and the Rockfall Susceptibility Index (I_{RFS}).

At this stage, all the indicators are assigned to individual clusters of a joint set. The next stage consists of integrating them in a way to highlight the areas on the 3DPC which are more prone to rockfall, in other words, potential source areas of block detachment. The approach proposed in this work requires 3 main steps: (i) scoring system definition, (iii) calibration, and (iii) integration into a Rockfall Susceptibility Index.

(i) Scoring system definition: consists of giving each indicator a score of 0, 1 or 2 based on how they contribute for the quality of the rock mass (spacing and persistence), stability of the slope (SMR) and lack of support for overlaying rocks masses (overhanging). For instance, lower values of normal spacing and higher values of persistence decrease the rock mass quality, as described in the RMR system (Table 2-1), and therefore receive a higher value in the scoring for susceptibility. In addition, joints with SMR classes considered as unstable according to Romana (1993) will be also given a high value of scoring as well as the presence of overhanging.

(ii) Calibration: the thresholds to define if an indicator is 0, 1 and 2 were established using areas on the 3DPC of the rock slope with different rockfall susceptibility levels based on visual observation. For instance, suppose an overhanging part of a slope (high susceptibility) has all the joints with normal spacing below 0.30 m, a more stable area has the joints with normal spacing below 1m and a complete stable area has all the joints above 1m of normal spacing. Hence, the threshold for the spacing indicator I_S can be set as high for I_S < 0.30m, moderate for 0.30m < I_S < 1 m and low for I_S > 1 m. This procedure allows the calibration of the indicators via an interactive trial and error process, similarly to the approach of Mavrouli et al. (2019) for calibration of indicator for a rockfall frequency index applied to rocky slopes of the Basque Country.

(iii) Integration into a Rockfall Susceptibility Index: once each indicator is scored (0,1 or 2), they are summed up with the same weight as I_S (spacing), I_P (persistence), I_{SMR} (SMR) and $I_{Overhanging}$ (overhanging) to give the Rockfall Susceptibility Index I_{RFS}:

$$I_{RFS} = I_S + I_P + I_{SMR} + I_{Overhanging} \qquad (16)$$

This same weight approach is an equivalent strategy used by Matasci et al. (2018) when combining their failure indexes for the final rockfall susceptibility index in 3DPC and by Mavrouli et al. (2019) for combining indicators for rockfall frequency index for slope stability assessment in fieldwork. Even though this index provides a numerical value, the differentiation of susceptibility levels (high, moderate and low) depends on the specific site characteristics of a given slope and thus requires a user evaluation. Additionally, a higher index in a particular area in the slope does not guarantee that a rock detachment will occur in the future, but rather it is an indication of areas in the slope more prone than others based on the considered indicators (overhanging, spacing, persistence and SMR). These highlighted areas can be afterward used for a more detailed hazard studied including block volume calculation (as performed in this thesis), intensity and trajectory of fallen blocks as also suggested by Matasci et al. (2018).

In practical terms, steps (i) and (iii) are done in the input *.txt* file (Figure 4-11) using *if* (if condition) or *ifs* (if else condition) function in *Excel* as to reclassify the original values of indicators into the scores (0,1 or 2) and further summing all the columns (indicators) to obtain I_{RFS} (Figure 4-12). At the end of this process, all the 3D points have a I_{RFS} and can be visualized in *CloudCompare* as a *scalar field*.

	A	B	C	D	E	F	G	H	I	J
1	x	y	z	js	cl	I_S	I_P	I_{SMR}	$I_{overhang.}$	I_{RFS}
2	766197	3912555	1510.77	2	1	2	2	0	0	4
3	766197	3912555	1510.76	2	1	2	2	0	0	4
4	766197	3912555	1510.76	2	1	2	2	0	0	4
5	766197	3912555	1510.77	2	1	2	2	0	0	4
6	766197	3912555	1510.75	2	1	2	2	0	0	4
7	766197	3912555	1510.76	2	1	2	2	0	0	4
8	766197	3912555	1510.75	2	1	2	2	0	0	4
9	766197	3912555	1510.77	2	1	2	2	0	0	4
10	766197	3912555	1510.76	2	1	2	2	0	0	4
11	766197	3912555	1510.76	2	1	2	2	0	0	4
12	766197	3912555	1510.75	2	1	2	2	0	0	4

Figure 4-12. Screenshot of .txt file in Excel containing the scoring of indicators ($I_S, I_P, I_{SMR}, I_{Overhanging}$) and rockfall susceptibility index (I_{RFS}) of some 3D points of the rock slope in this case study.

5. APPLICATION TO A ROCK SLOPE IN SAMARIA GORGE NATIONAL PARK, CRETE (GREECE)

The methodologic workflow described in Chapter 4 was applied to a rocky slope on the road cut leading to the refugee Kallergis (Figure 3-1c), where the risk is related to vehicle passengers. Although this road is not highly transited, this slope was selected as an example for the application of the method and the processing of the point cloud, to be further extended to cut and natural slopes where risk is higher, and detailed susceptibility and hazard analysis are required. The sections below describe the results obtained in each of the 4 sequential blocks of the proposed methodology (Figure 4-1).

5.1. Feature Extraction

5.1.1. Joint Set Orientation

According to the literature, different values for the input parameters have been used in the DSE software (Buyer et al, 2020; Menegoni et al, 2019; Riquelme et al., 2014; Riquelme et al., 2018). Riquelme et al. (2014) for instance defined optimal values of nearest neighbor k_{nn} = 30 points and coplanarity test η_{max} = 0.2 when using known geometric objects (cube and icosahedron) for validation and sensitivity analyses of the results. Nevertheless, when applying the method for joint set extraction of a real rock slope, these authors changed the values of some parameters to best fit the real outcrop point cloud (k_{nn} was set to 20). Riquelme et al. (2014) also acknowledged that the user should have a good background on rock mechanics and engineering geology as to evaluate what values should be used for each case.

Taking this recommendation into account, different combinations of parameters were tested in the rock slope point cloud in this study, including the optimal values of knn and η_{max}. After visual validation of the extracted joints of each attempt with the observation that correspond to ground truth, the settings of input parameters that best represent the observed joins sets in the field were finally defined as summarized in Table 5-1. The parameter k, which determines if clusters should be merged or not, does not interfere with the extraction of joint sets. However, it does influence the computation of persistence as further discussed in section 5.1.2.

Table 5-1. Input parameters used for joint set extraction in the rock slope point cloud in this study.

Parameter	Value
K nearest neighbour – k_{nn}	20 points
Tolerance for the coplanarity test - η_{max}	0.3
Number of bins for the density analysis - nbin	64
User-defined number of joint sets - JS	4
Minimum angle between principal poles – γ_1	20°
Maximum angle between a pole and its principal pole (cone filter) – γ_2	30°
Minimum number of points per cluster - ppc	100 points
Cluster distribution threshold for cluster alignment - k	1.5

A total of 4 joint sets were extracted (Figure 5-2) with their corresponding dip direction and dip angle of the principal pole, the number of clusters and the total number of points assigned for each of them (Table 5-2). The principal pole of each joint set considered in this study takes the cone filter γ_2 of 30 degrees, which implies that all the poles of the normal vectors of points that have dip direction and dip angle within 30 degrees of this principal pole orientation are assigned to this family (set) of joints. This is why the values of principal poles are followed by ± 30 degrees in Table 5-3.

JS 1 is the most representative joint set in the slope with the majority of points (3,459,156). It corresponds to the slope surface and also the bedding plane of the geological layers in the study site. JS 3 and JS 4 correspond to the overhanging, and JS 2 is almost a sub-vertical joint bounding the lateral sides of the overhanging surfaces (Figure 5-3).

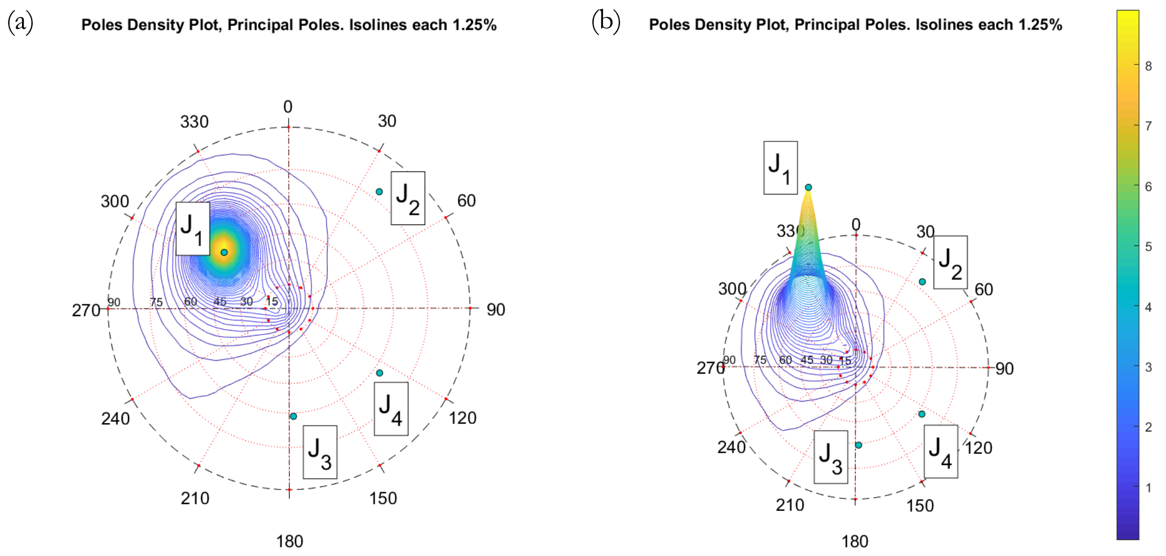

Figure 5-1. (a) Stereogram with the principal pole of extracted joint sets and (b) density estimation via kernel of poles in the point cloud for each joint set. The higher density of J1 corroborates the more exposed slope surfaces compared to any other surface in the point cloud.

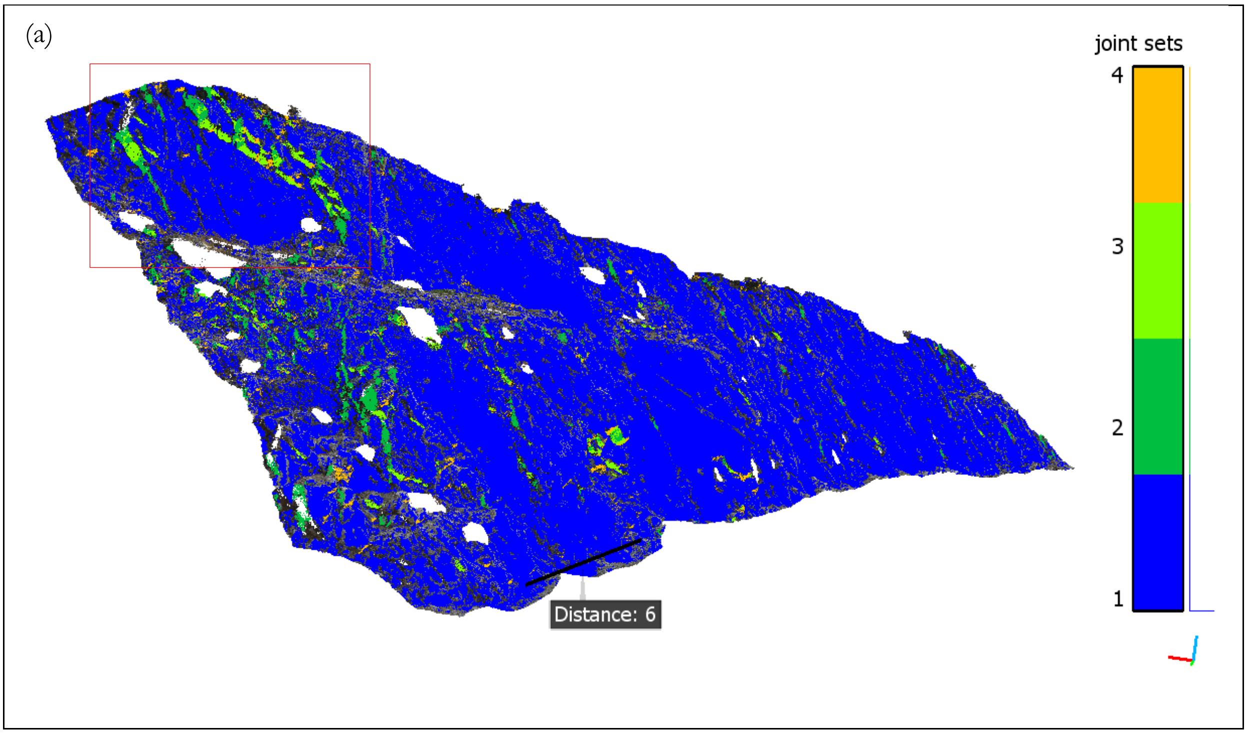

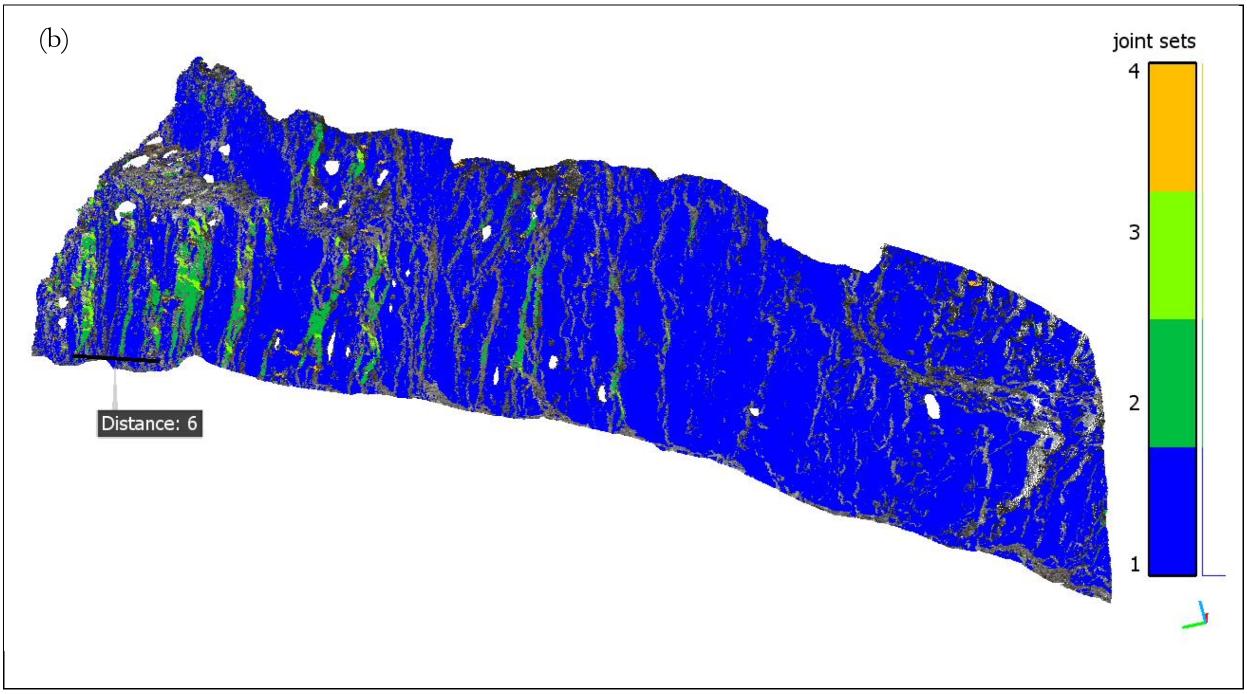

Figure 5-2. Point Cloud of rock slope classified into 4 joint sets in different view angles (a) and (b). The red box in (a) is enlarged as Figure 5-3. Distance is in meters.

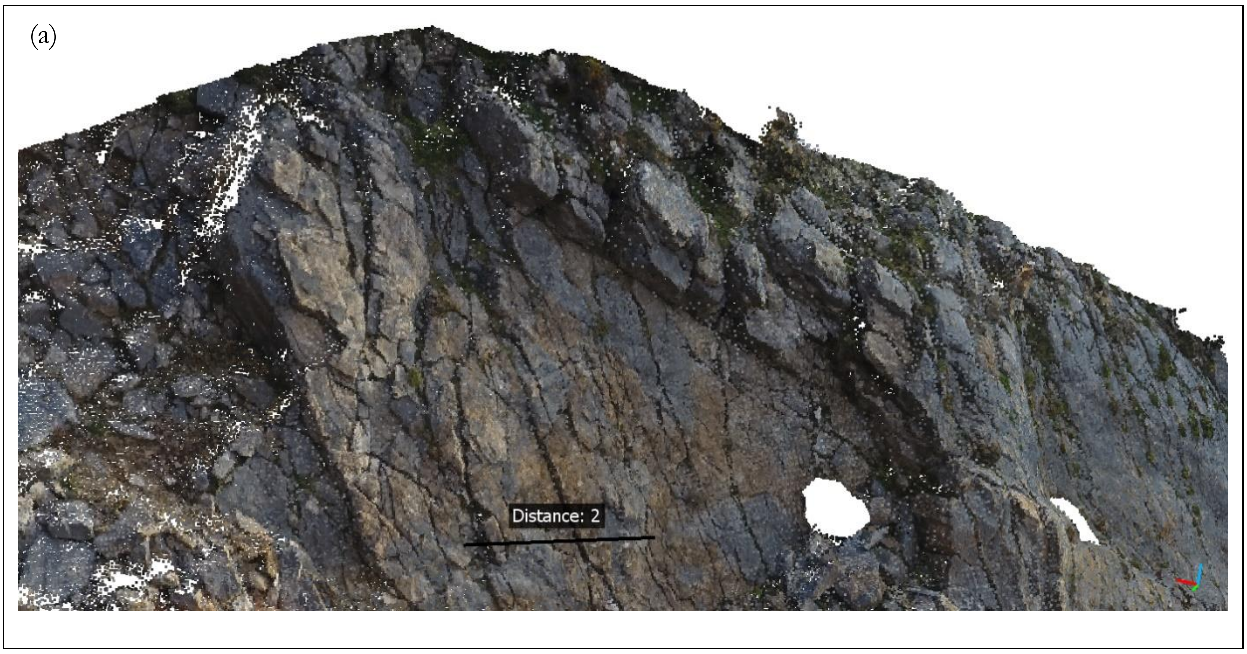

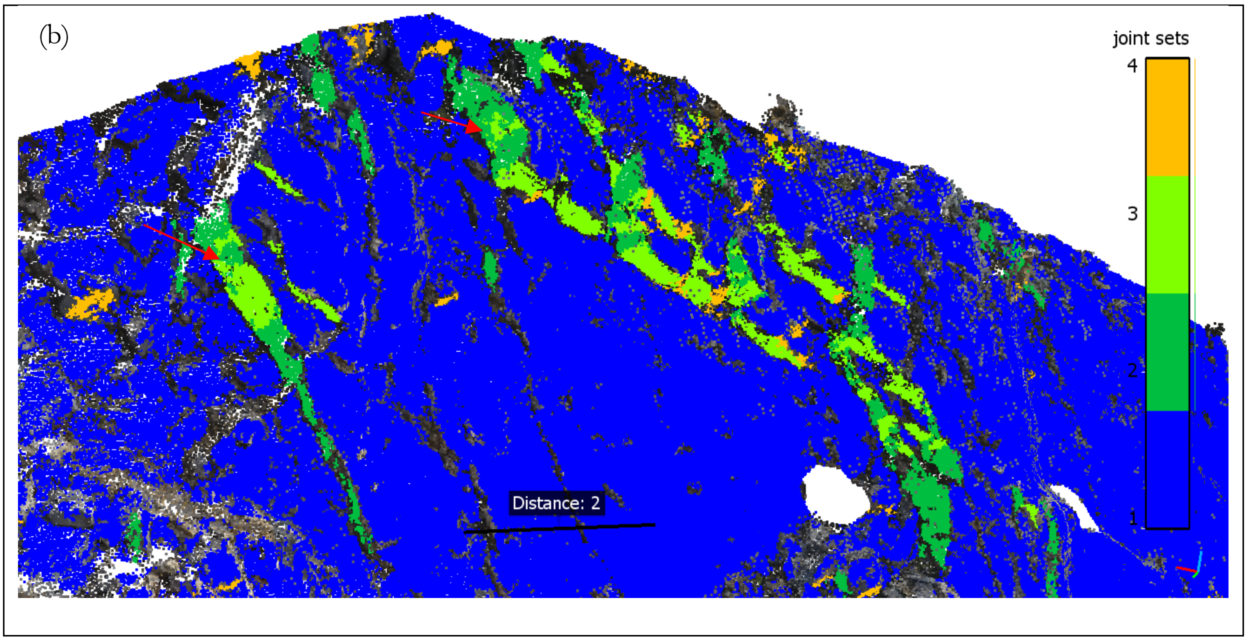

Figure 5-3. Upper part of the rock slope highlighting the overhanging (J3, J4) in RGB point cloud (a) and classified into joint sets (b). Notice the waviness of some surfaces resulting in points assigned both to J2 and J3 (red arrows). Distance is in meters.

Table 5-2. Summary of extracted joint sets information.

Joint set	Dip direction (°)	Dip angle (°)	Number of clusters	Number of points
JS_1	311	51	190	3,459,156
JS_2	38	78	269	106,408
JS_3	178	62	143	39,530
JS_4	126	63	162	40,361

On one hand, joint sets represented by planar surfaces are well characterized by this method and the points on these surfaces are correctly assigned to their corresponding joint sets. On the other hand, one limitation of this method is that points belonging to less planar surfaces (i.e. waviness or roughness) can often be assigned to two different joint sets as noted in some parts for J2 and J3 (Figure 5-3). This fact also explains why J2 has a slightly higher difference of 14 degrees in the dip direction and J3 of 12 degrees in dip angle compared to the values obtained in the field with the compass-clinometer (Table 5-3, Appendix B). It should be noted that field measurements using a compass-clinometer are also subjective to error mainly due to: human bias in the plane chosen for collecting the orientation, in other words, whether it is representative or not of that joint set (especially if it is a wavy surface), and the compass inherent precision of one degree (Slob, 2010). Given the aforementioned considerations, the values for joint set dip direction and angle using the DSE software are similar to those obtained in the field.

Table 5-3. Comparison of joint sets orientation using DSE software and compass in the field. The latter considers only one measure in a plane in the rock slope for each joint set. No statistical analysis was carried out for the field measurements since the objective was not to validate this approach, rather guide in the decision of input parameter values.

Joint set	DSE Dip dir./Dip angle (°)	Field data - Compass Dip dir./Dip angle (°)	Difference Dip dir./Dip angle (°)
JS_1	311/51 ± 30	320/55 ± 1	9/4
JS_2	38/78 ± 30	24/85 ± 1	14/7
JS_3	178/62 ± 30	180/50 ± 1	2/12
JS_4	126/63 ± 30	Not available	Not available

5.1.2. Joint Set Persistence

The first step before the computation of persistence of a given joint set is to evaluate visually in the point cloud if that joint set can be considered as persistent or non-persistent, as illustrated in Figure 2-2a. In case it is persistent, the parameter k for merging clusters should be applied as proposed by A. Riquelme et al., (2018). Otherwise, the cluster should not be merged and considered therefore as individual planes. The results for visual evaluation for each joint set are as follows:

For JS 1, approximately 96% of all the points are assigned to only 6 out of the 190 clusters in total (Figure 5-4b). These 6 clusters have a large extension in area, greater than 20 m^2 (Figure 5-4a), in other words, are persistent.

For JS 2, 50% of all the points are assigned to 40 clusters while the other 50% are assigned to the other 229 clusters (total of 269) (Figure 5-4d). The visual inspection also shows the clusters do not have a continuous extension in the 3D space but are rather interrupted (Figure 5-4c), with lower extension in area, less than 2 m^2.

For JS 3, approximately 50% of all the points are assigned to 31 clusters while the other 50% are assigned to the other 113 clusters (total of 143)(Figure 5-4f). Similarly to JS 2, the visual inspection also shows that the clusters of JS 3 do not have a continuous extension in the 3D space but are rather interrupted (Figure 5-4e), with lower extension in area, less than 1 m^2.

For JS 4, approximately 50% of all the points are assigned to 36 clusters whereas the other 50% are assigned to the other 126 clusters (Figure 5-4h). Visual inspection also shows that the clusters of JS 4, similar to JS 2 and 3, have a lower extension in area (Figure 5-4g), less than 0.5 m^2.

In summary, after visual inspection and statistical analysis via histograms, the joint sets in the rock slope can be classified concerning their persistence as J1 persistent, and J2, J3 J4 as non-persistent.

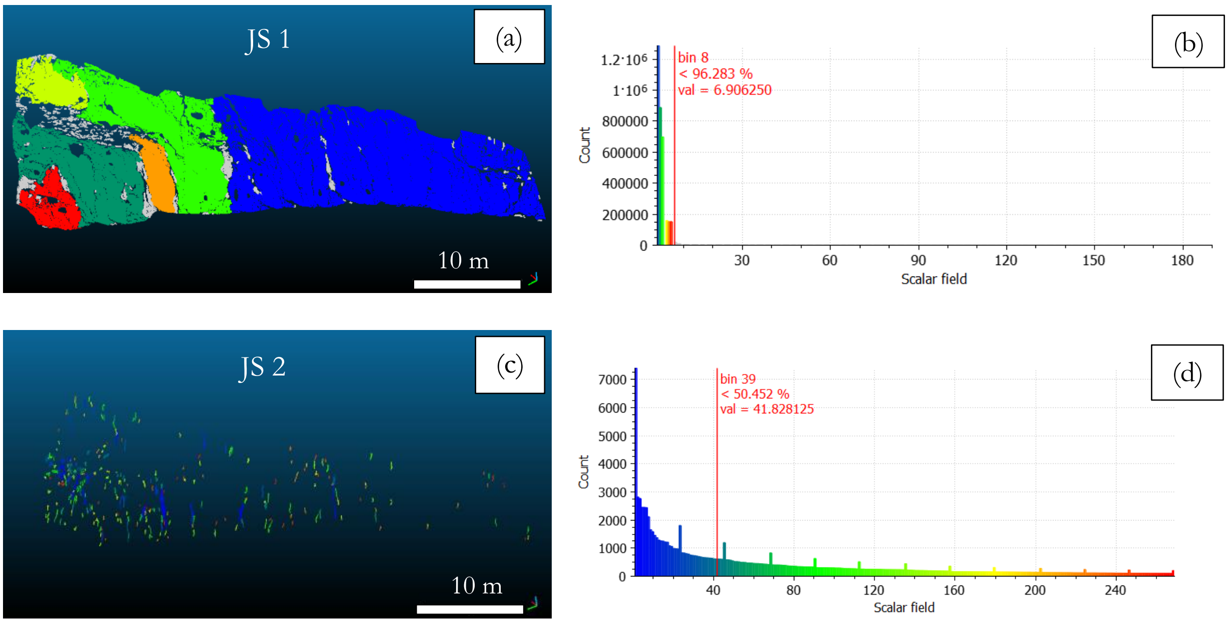

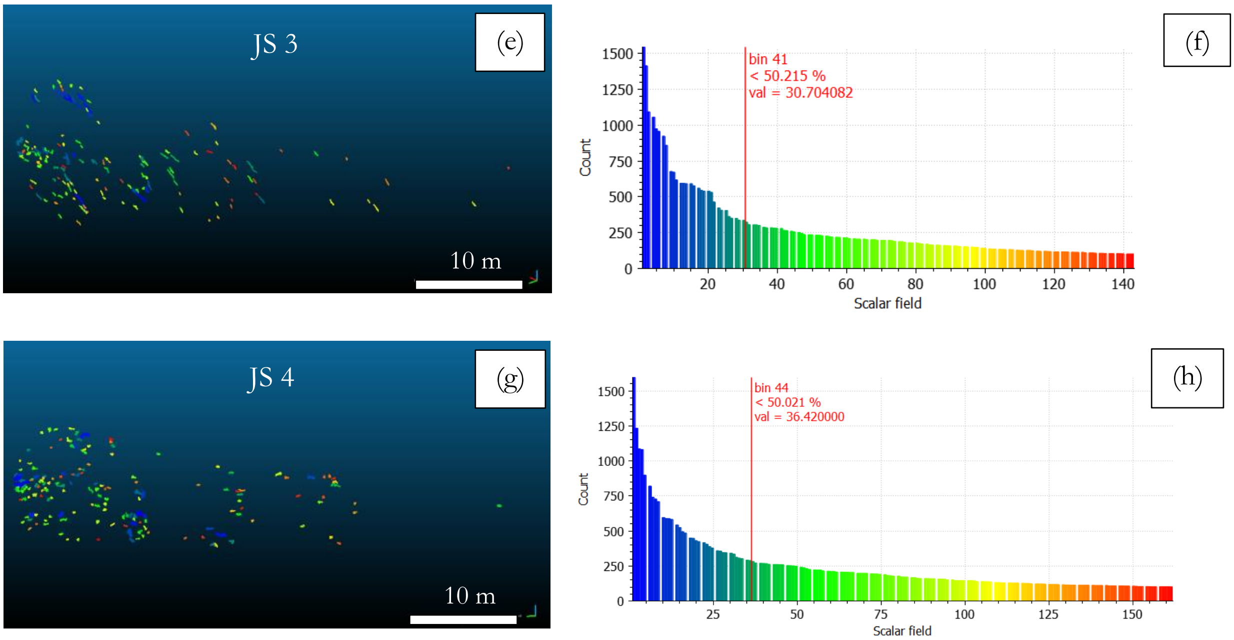

Figure 5-4. Left images show the distribution of clusters in 3D space for each joint set. Right images show the histogram of points for each cluster of a joint set, where the y-axis is the number of points (count) and the x-axis is the cluster id (scalar field): JS 1 (a, b), JS 2(c, d), JS 3 (e, f), JS 4(g, h). Note that for JS 1, 6 clusters colourized in (a) represent the majority of points, approximately 96% (b).

The second step is to determine the k threshold to merge the cluster of JS 1 (Eq. (4) and (5)), as it is considered to be persistent. This condition can be tested for this case study in two large clusters of JS 1, clusters 3 and 8, that are coplanar since D parameter are very similar, D_3= -1.533.583,7852 m and D_8= -1.533.583,8610 m. Given their standard deviations[3] as σ_3 = 0.2675 m and σ_8 = 0.0805 m respectively and the mean normal spacing of JS 1 as 0.311 m, k can be first set as 1 to evaluate the influence of standard deviation alone:

$$|D_3 - D_8| \ll 1\, x\, (\sigma_3 + \sigma_8) \ll S \qquad (17)$$

$$0.0758 \ll 1\, x\, 0.348 \ll 0.311 \qquad (18)$$

On the one hand, the first part of the inequation (18) is fulfilled as the $s_{coplanar-cluster}$ is smaller then the sum of the standard deviations $\sigma_3 + \sigma_8$. On the other hand, the second part is not fulfilled as the standard deviation is not smaller than the normal spacing S, instead it is greater. A possible explanation of the large values of standard deviations is the large extension of cluster 3: the bigger the cluster, the more likely the points will have a larger distance to the best fitting plane and as consequence, a large standard deviation. By setting k =1, these two coplanar clusters would be merged resulting in only one plane for computing the persistence, but at the cost of merging smaller clusters that are might not be coplanar. These processes would result in the unrealistic computation of persistence (larger than expected) and therefore is not adopted in this case study. It is preferred to consider JS 1 as non-persistent (k=0) and compute the persistence of all the clusters separately, similarly to the approach for the other joint sets, even though the visual observation shows evidence that JS 1 is persistent.

Based upon the aforementioned considerations, the persistence of each cluster of a given joint set in the direction of dip, strike, maximum length and the area of convex hull was calculated in the DSE software. That implies that for each cluster, 4 calculations were performed (dip, strike, maximum and area) as

[3] The standard deviation of each cluster is provided in a *.txt* file by the DSE software after the joint set extraction process (Section 4.2.1). Due to great amount of clusters (190), it is not practical to show all the results here.

illustrated in Figure 5-5. Thus, for JS 1 with 190 clusters, 760 values of persistence were obtained. For JS 2 with 269 clusters, 1,076 values of persistence, JS 3 (143 clusters) 572 values and JS 4 (162 clusters) a total of 648 values of persistence. The summary of statistical analyses is presented in Table 5-4 and the histograms in Figure 5-6 and Figure 5-7.

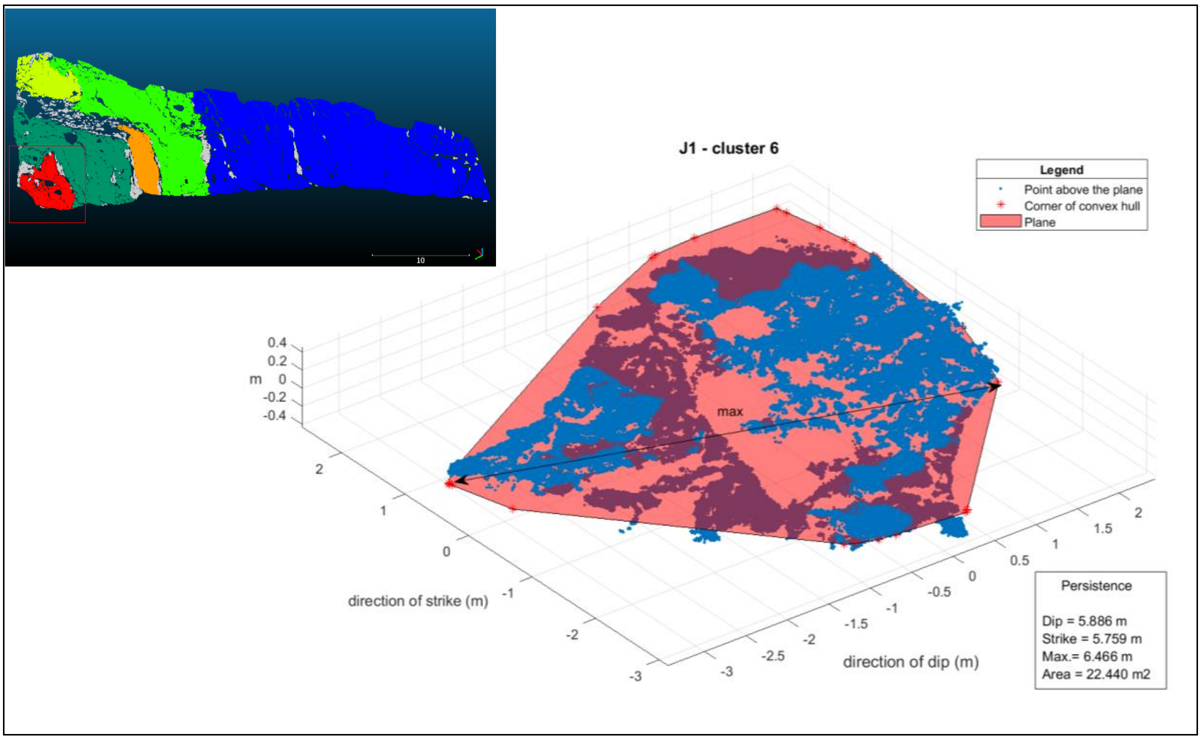

Figure 5-5. Calculation of persistence in the direction of dip, strike, maximum length and area of the convex hull for cluster 6 of JS 1 in DSE software. The purple points are below the best-fit plane whereas the blue is above.

As expected, JS 1 has the maximum values of persistence and area (Table 5-4). Nonetheless, the mean values are similar to the mean values of other joint sets. This happens because out of 190 clusters, only 6 clusters have the persistence from 5 to 32 m and area from 22 to 265 m², whereas the other 184 clusters have persistence and area inferior than 3 m and 3 m². Thus, when calculating the mean it lowers the values influenced by the great amount of smaller clusters. Cautions should then be taken to use the mean values for this particular joint set, keeping in mind it does not express properly the persistence for this joint set since it underestimates the influence of the 6 major clusters. JS 2 and JS 3 have a similar range of persistence, concentred up to 2.5 meters and area below 0.50 m² (Figure 5-6 and Figure 5-7). Their mean values of persistence are also similar (Table 5-4). Finally, JS4 has the lowest persistence mainly up to 1m as well as the smallest areas, mainly up to below 0.10 m² (Figure 5-7).

As explained in Section 4.2.2, these persistence values are calculated for joints represented by exposed surface (not trace length) and thus do not provide insights on what happens inside the rock mass.

Table 5-4. Statistical summary of persistence on the dip (= dip angle), strike (=dip direction), maximum length and area of the convex hull for the extracted joint sets.

JS_1	dip (m)	strike (m)	max. (m)	area (m²)
min	0.058	0.074	0.110	0.004
max	14.179	30.770	32.453	265.214
mean	0.657	0.778	0.992	3.024
mode	0.250	0.362	0.531	0.087

JS_2	dip (m)	strike (m)	max. (m)	area (m²)
min	0.093	0.078	0.146	0.008
max	2.424	2.272	3.182	1.723
mean	0.437	0.442	0.574	0.117
mode	0.355	0.477	0.437	0.039

JS_3	dip (m)	strike (m)	max. (m)	area (m^2)
min	0.089	0.131	0.139	0.008
max	1.382	1.372	1.862	0.773
mean	0.375	0.422	0.511	0.094
mode	none	0.343	0.334	0.141

JS_4	dip (m)	strike (m)	max. (m)	area (m^2)
min	0.073	0.133	0.161	0.008
max	0.689	1.397	1.434	0.388
mean	0.225	0.342	0.378	0.054
mode	0.189	0.259	0.521	0.031

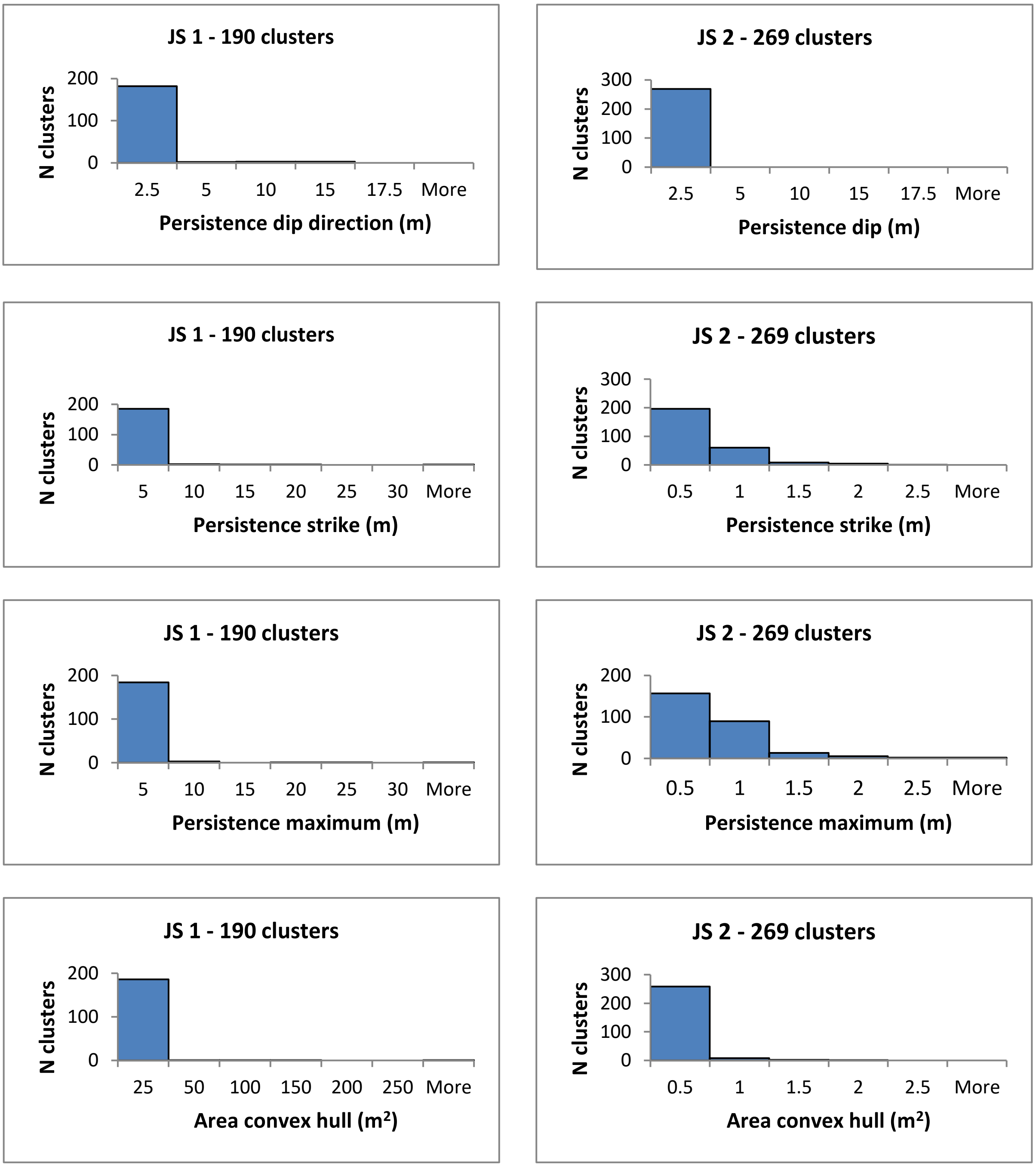

Figure 5-6. Histograms for persistence on the dip, strike, maximum length and area of the convex hull for joint sets 1(left side) and 2 (right side).

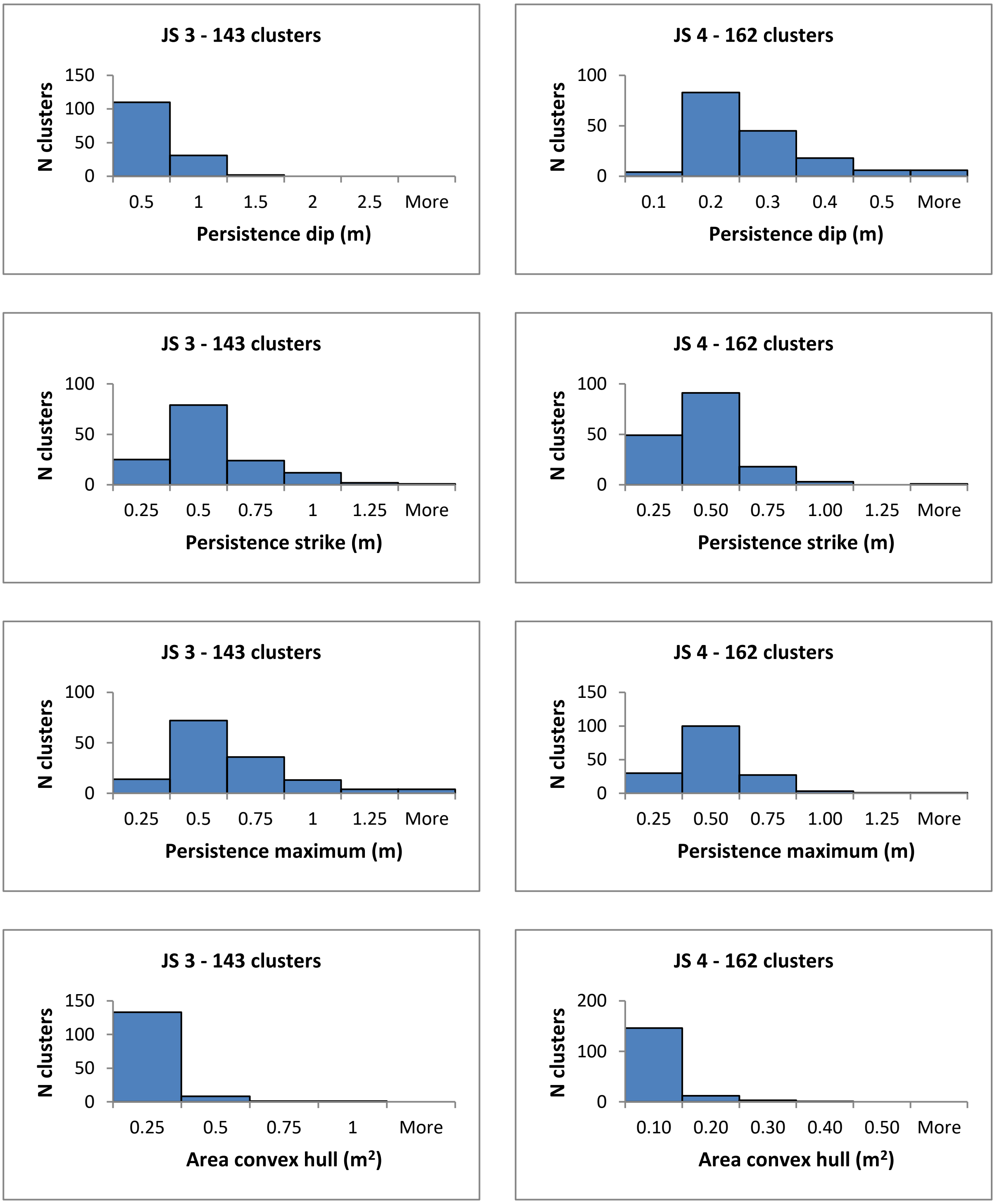

Figure 5-7. Histograms for persistence on the dip, strike, maximum length and area of the convex hull for joint sets 3(left side) and 4 (right side).

5.1.3. Joint Set Spacing

After evaluating the persistence condition of each joint set, the normal spacing is calculated using the DSE software. For each cluster, the normal distance is measured to the closed cluster and the values of spacing are therefore for a pair of clusters. For instance, the normal distance of cluster 1 from JS1 was measured to cluster 122, cluster 2 to cluster 29, cluster 3 to cluster 98 and so on. The total number of values is therefore the number of identified clusters of each respective joint set minus 1. As a result, for JS 1 (190 clusters), a total of 189 values of spacing were measured, JS 2 (269) a total of 268 values, JS 3 (143) a total of 142 and JS 4 (162) a total of 161 values of normal spacing. The statistical population is summarized in Table 5-5 and the histogram in Figure 5-8.

Table 5-5. Statistical population for the normal spacing of the extracted joint sets.

Statistical population	JS 1	JS 2	JS 3	JS 4
	Non-persistent	Non-persistent	Non-persistent	Non-persistent
Minimum (m)	0.000[A]	0.004	0.009	0.001
Maximum (m)	2.293	4.329	5.057	3.096
Mode (m)	none	0.136	none	0.114
Mean (m)	0.311	0.481	0.620	0.514
Standard deviation (m)	0.461	0.606	0.832	0.507
Number of cluster	190	269	143	162

A – The actual measurement is $4.86.10^{-5}$ m with no rounding.

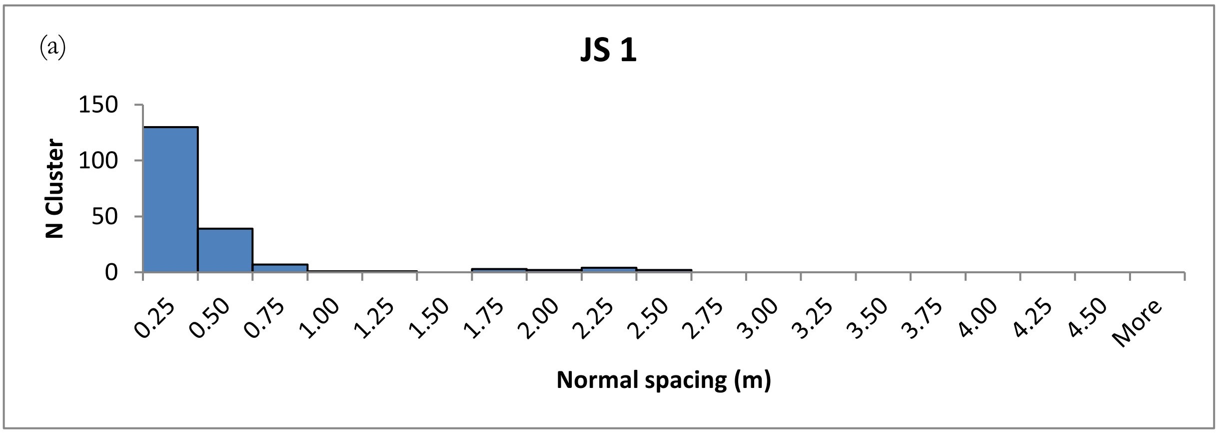

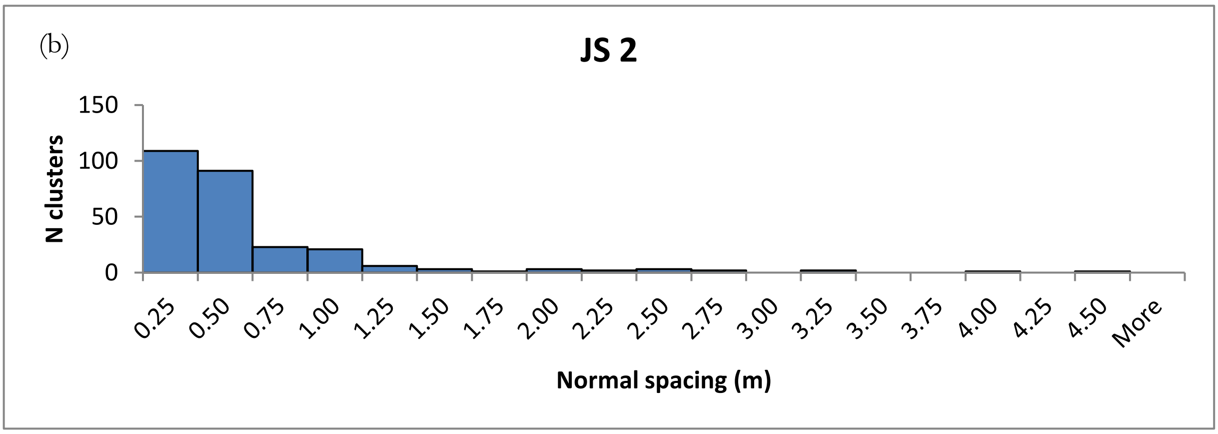

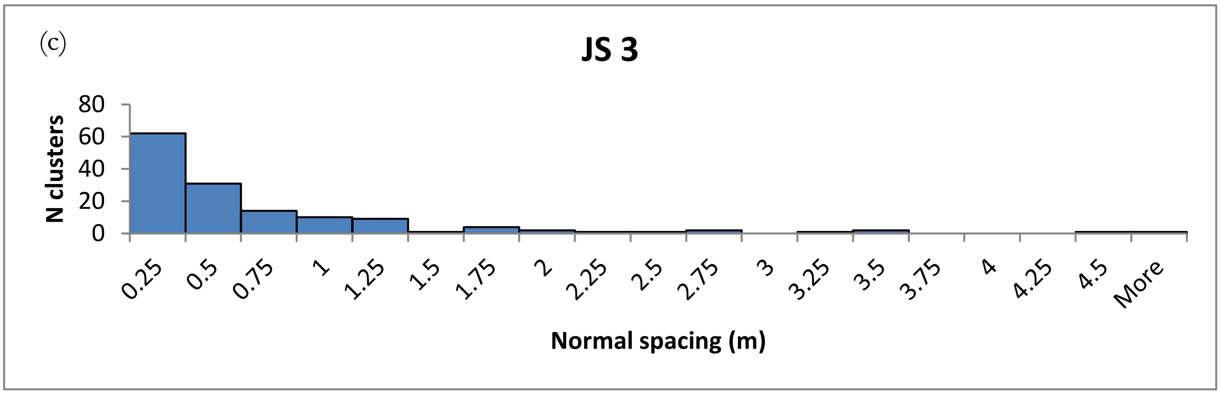

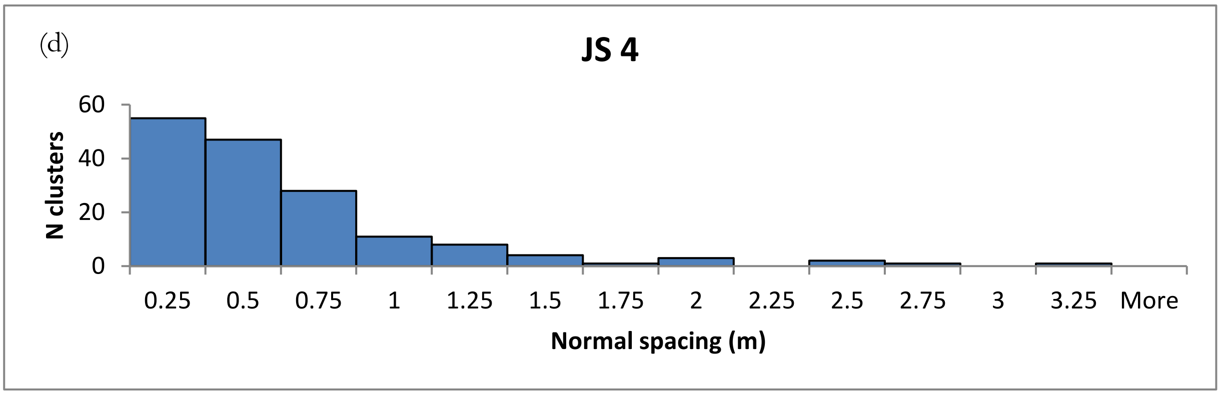

Figure 5-8. Histogram for normal spacing for extracted joint sets considering a non persistent condition: JS 1 (a), JS 2 (b), JS 3 (c) and JS 4 (d).

As observed in the histograms, the majority of values for normal spacing for all joint sets lies from 0 to 1.25 m. Joint set 3 has the highest maximum spacing as well as the highest mean spacing, whereas joint set 1 has the lowest (double the difference). JS 1 represents the slope surface but also the bedding plane of the geological layers. As a result, the main spacing of this joint set (0.311 m) represents on average the spacing between the bedding planes, which are corroborated by field observation as in the scale of few decimetres (0.20 to 0.30 m) (Figure 5-9). The minimum spacing of JS 1 of 0.000 m is the rounding of $4.86.10^{-5}$ m. The reason for such small value is explained by the fact that the clusters 5 and 11 where the measurement was done have a very similar D parameter (position in space – Eq. (2)). In other words, they are almost coplanar and therefore the normal distance is practically zero. In case a k threshold was used, they would be merged and form only one plane.

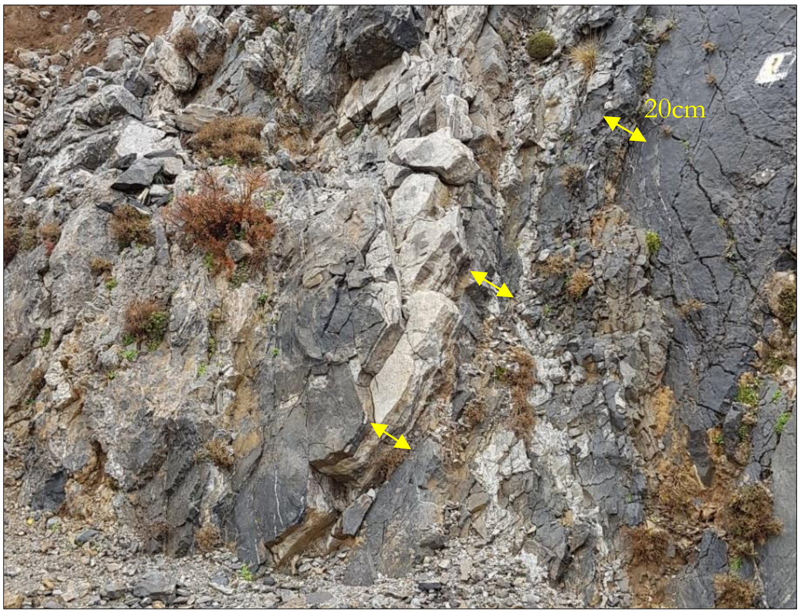

Figure 5-9. Bottom part of the rock slope with exposed bedding planes of decimetres thickness (yellow arrows).

5.1.4. Block volume calculation

The first approach is to calculate the mean block volume V_b for the rock slope using Eq (11). The predominant intersecting joint sets in the overhanging which delineate blocks are JS 1, 2 and 3 (Figure 5-2). The mean normal spacing of Table 5-5 is then used to calculate V_b:

$$V_b = 0.311\,m\,x\,0.481\,m\,x\,0.620\,m = 0.093\,m^3 \quad (19)$$

The calculated V_b (0.093 m^3) is 34 % larger than the measured block volume (0.064 m^2) of the biggest fallen block found approximately 2,5 m below the overhanging, in a small Plato (Figure 5-10). Considering that the computed normal spacings are correct, this difference can be explained either: (i) due to small fragmentation process when a fallen block impacts the surface, breaking into smaller pieces and thus reducing its size or (ii) freeze-thaw process on the fallen blocks leading to cracks and breakage. This latter is a reasonable assumption since this rock slope is located in a mountainous area (Chapter 3), thus susceptible to temperature variation.

Figure 5-10. Fallen blocks below overhanging joints in the upper part of the rock slope. Note cracks in a block (white dashed line), leading to breakage. Scale: geologic hammer is approximately 40 cm.

The second approach is to estimate block volume locally in a given area of the 3DPC, taking as input the persistence (area of convex hull) multiplied by the spacing between to clusters (Eq. (13)). The overhanging in the upper part of the slope was selected to test this approach. The first attempt was done using the clusters of JS 2 (Figure 5-11a): cluster 16 (area) and normal spacing (S) to cluster 19, cluster 25 (area) and normal spacing (S) to cluster 115, cluster 50 (area) and normal spacing (S) to cluster 115. The second attempt was done using the clusters of JS 3 (Figure 5-11b): cluster 1 (area) and normal spacing (S) to cluster 11, cluster 7 (area) and normal spacing (S) to cluster 64, cluster 13 (area) and normal spacing (S) to cluster 59, cluster 11 (area) and normal spacing (S) to cluster 128. The estimated volume for each case is compared to the expected volume obtained manually on the *CloudCompare*, with the corresponded absolute and relative error (Table 5-6).

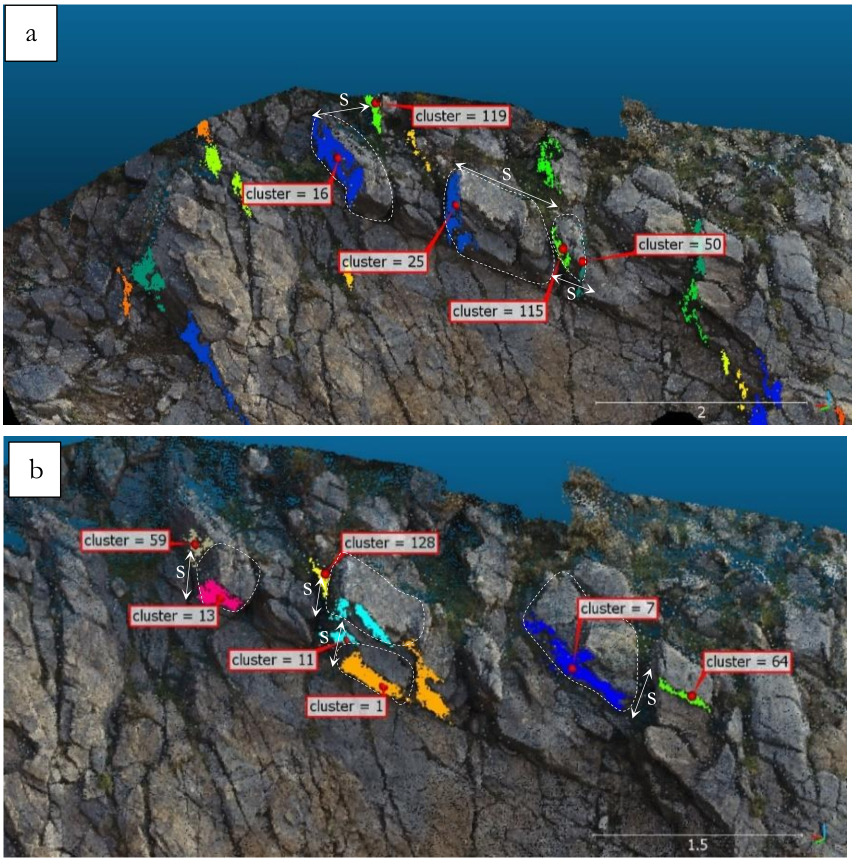

Figure 5-11. Overhanging block volume calculation using JS 2 (a) and JS 3 (b). The identified cluster id was used as the area of convex hull multiplied by the normal spacing (S) to the closest cluster. The white dashed line illustrates the expected volume of Table 5-6. Scale in meters.

The comparison shows a better agreement between the calculated and expected volume for clusters of JS 3, with a maximum relative error of 10% whereas for JS 2 the minimum relative error is 20%. An explanation for this discrepancy in JS 2 is because the lateral surface of the clusters considered as an area for the volume calculation is not as flat as the base surface (overhanging) of clusters from JS 3. For instance, cluster 16 of JS 2 shows a wavy surface (Figure 5-11a) and this can produce an area of the convex hull that does not match the real area. This is an intrinsic limitation of persistence calculation of DSE software that computes the area of convex hull based on the best fitting plane to the points of a given cluster (Figure 5-5). For wavy surfaces, the points will either lie above or below the fitted plane (greater standard deviation of point-to-plane distance) and the computed area might not be as realistic as a scenario where points fit better on a flat surface (smaller standard deviation). For the above mention example, the calculated volume (0.142 m^3) is greater than the expected (0.093 m^2) by 34%.

Therefore, this second approach provides more realist results of local block volume calculation for flat exposed surfaces in a 3DPC.

Table 5-6. Comparison of local block volume estimated in the 3DPC compared to manually calculated in CloudCompare (expected).

JS	Cluster [i] id	Cluster [j] id	Area [i] (m^2)	Spacing [i,j] (m)	Volume [i, j] (m^3)	Volume expected (m^3)	Absolute error (m)	Relative error (%)
2	16	119	0.413	0.343	0.142	0.093	0.049	34
	25	115	0.295	0.932	0.275	0.190	0.085	31
	50	115	0.184	0.197	0.036	0.044	0.007	20
3	1	11	0.325	0.080	0.026	0.024	0.002	6
	7	64	0.272	0.069	0.019	0.021	0.002	10
	13	59	0.108	0.200	0.022	0.022	0.000	1
	11	128	0.196	0.195	0.038	0.039	0.001	3

5.2. Rock Slope Stability Assessment

5.2.1. Rock Mass Rating

Firstly, the results of the five geomechanical classification parameters for the RMR are described individually and summarized in Table 5-8. The rating of each parameter is then used to compute the RMR (Table 5-9). Although the score of each joint set is slightly different (63 – 75), they summed scores fall within the same class II, corresponding to good quality rock.

Strength of Intact Rock Material - A1

The strength of intact rock material was estimated in the field by using a geologic hammer to fracture the rock. Since the specimen required from 2 to 5 blows to be fractured and is limestone as lithology, the estimated Uniaxial Compressive Strength lies in the range 50 to 100 MPa according to Brown 1981 (as cited in Hoek, 2007, p.195).

Rock Quality Designation (RQD) – A2

As previously stated in section 4.3.1, drill cores were not available for this study site. To overcome this data limitation, the proposed approach herein was to select 3 vertical to sub-vertical sections on the 3DPC that show different fracture patterns (Figure 5-12) and apply the RQD directly on the 3DPC as if they were core drills: sum rock fragments larger than 100 mm, divided by the total length (Figure 5-13). In this procedure, the rock fragments are portions of rock intersected by joints on the surface of the slope.

The RQD calculation yields from 85 to 90% (Table 5-7), which falls within the range from 75 to 90% of the RMR. Considering the mean joint set spacing $S_1 = 0.311$ $S_2 = 0.481$, $S_3 = 0.620$, $S_4 = 0.514$ (Table 5-5), the result for J_V is 8.72 joints/ m^3 (Eq. (15) and thus RQD is 88% (Eq.(14), in agreement with the previous results from 85 to 90%.

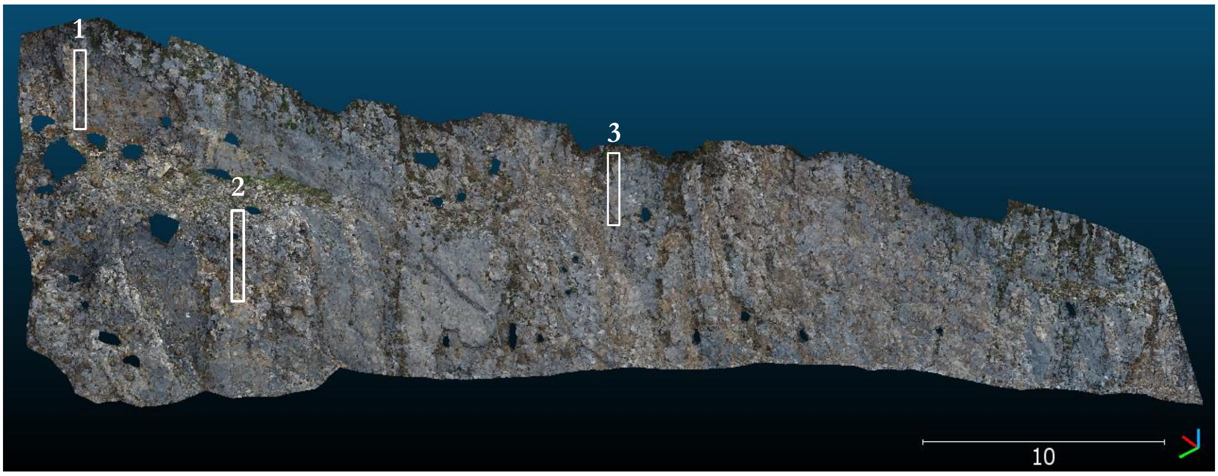

Figure 5-12. Approximate location of the 3 sections in the rock slope used for RQD calculation. Scale in meters.

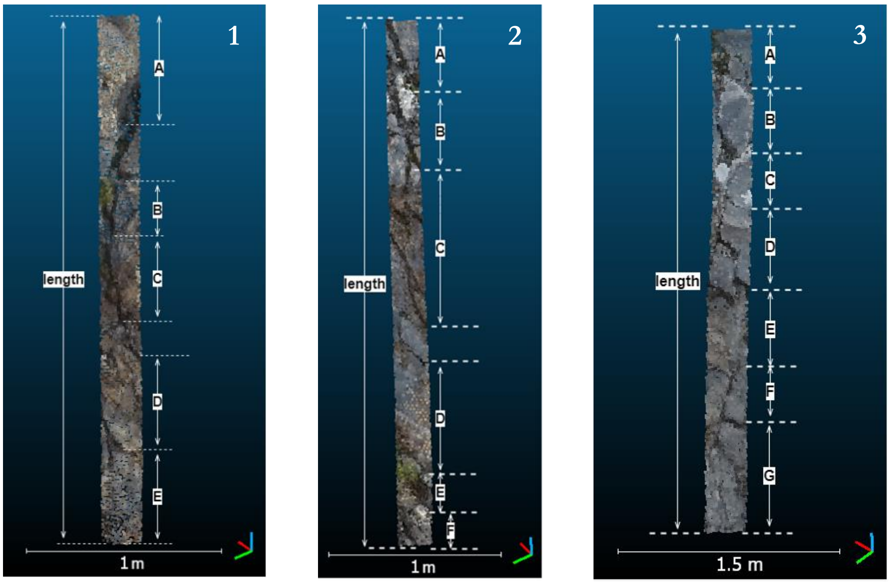

Figure 5-13. Sections on the 3DPC for the calculation of RQD. Rock fragments greater than 10 cm are highlighted with letters as well as the total length of each section (1,2 and 3).

Table 5-7. Length values measured in 3DPC for each section and its calculated RQD.

Section 1	
Fragments	Length (m)
A	0.66
B	0.26
C	0.38
D	0.49
E	0.52
Sum fragments	2.33
Total length	2.69
RQD	86%

Section 2	
Fragments	Length (m)
A	0.27
B	0.40
C	0.90
D	0.64
E	0.17
F	0.22
Sum fragments	2.58
Total length	3.03
RQD	85%

Section 3	
Fragments	Length (m)
A	0.46
B	0.28
C	0.35
D	0.44
E	0.50
F	0.35
G	0.61
Sum fragments	2.99
Total Length	3.33
RQD	90%

Spacing - A3

The normal spacing for each joint set considered is the mean value extracted from the 3DPC (Table 5-5). It is reasonable to use the mean instead of the maximum or minimum because it represents better the frequency peaks in the histograms for each joint set (Figure 5-8)

Condition of discontinuities - A4 and groundwater -A5

The persistence for joint sets 2, 3, and 4 considered is the mean value of all the maximum lengths from the clusters extracted from the 3DPC (Table 5-4). Instead of using the persistence in the direction of dip or strike (Figure 5-5), using the maximum length allows a conservative estimation of the rock mass quality.

Since JS 1 is mainly represented by 6 major clusters as explained in section (5.1.2), their mean value of maximum length was chosen (15.351 m) instead of the mean value considering all the 190 clusters together (0.992 m).

The remaining geomechanical parameters that describe the conditions of discontinuities - A4 (aperture, roughness, infilling, weathering) and condition of groundwater - A5 were acquired either via observation during the fieldwork or from photographs afterward (Appendices). It is worth noticing that for the roughness characterization, the only joint set that presents a uniform description is JS 1 as smooth. The others joint sets present a variety of roughness either in macro-scale (stepped, undulating and planar) and microscale (rough, smooth) according to the definition by ISRM (1978) or as the ranges of Joint Roughness Coefficient-JRC values (from 2 to 10, 14-16 and 18-20) according to the definition by Barton & Choubey (1977). Therefore, an intermediate description of slightly rough was chosen for JS 2, 3, and 4 for calculation of the RMR.

Table 5-8. Geomechanical classification parameters of each joint set for the RMR calculation.

Joint sets	A1	A2	A3	A4 - Conditions of Joint Sets					A5
	Strength (MPa)	RQD (%)	Spacing (m)	Persis. (m)	Aper. (mm)	Rough.	Infill.	Weath.	Groundwater
J_1	50 -100	83	0.311	15.351	> 5	Smooth	None	Unweath.	None
J_2	50 -100	83	0.481	0.574	> 5	Slightly rough	None	Unweath.	None
J_3	50 -100	83	0.620	0.511	> 5	Slightly rough	None	Unweath.	None
J_4	50 -100	83	0.514	0.378	> 5	Slightly rough	None	Unweath.	None

Table 5-9. Rating of geomechanical parameters for computation of RMR.

Joint sets	A1	A2	A3	A4 – Conditions of Joint Sets						RMR_b Rating	RMR_b Class
J_1	7	17	10	1	0	1	6	6	15	63	II
J_2	7	17	10	6	0	3	6	6	15	70	II
J_3	7	17	15	6	0	3	6	6	15	75	II
J_4	7	17	10	6	0	3	6	6	15	70	II

5.2.2. Slope Mass Rating

The input parameters for SMR calculation and the results for each joint set applying the *SMRTool* calculator are shown in Table 5-10. Although wedge and toppling failures were automatically computed, they were not considered for this case study since visual inspection of the rock slope did not show evidence of these types of failure.

Table 5-10. Parameters for SMR calculation and results for each joint set. P – planar failure, T – toppling failure.

Joint sets	Dip dir. (°)	Dip angle (°)	RMR_b	A (°)	B (°)	C (°)	Failure	F_1	F_2	F_3	F_4	SMR	Class
J_1	311	51	63	0	51	0	P	1	1	-25	15	53	III
J_2	38	78	70	87	78	27	P	0.15	1	0	15	85	I
J_3	178	62	75	47	62	113	T	0.15	1	-6	15	89	I
J_4	126	63	70	5	63	114	T	0.85	1	-6	15	80	II

In contrast from the RMR, the joint sets were assigned to different classes: JS 2 and 3 as class I (completely stable), JS 4 as class II (Stable), and JS 1 as class III (partially stable). JS 1 configures a more unsafe situation compared to others because its orientation is parallel to the slope orientation, indicated by F_1=1. In other words, the bedding plane of the geologic layer has the same dip direction and angle as the sliding plane of the slope, which naturally favours instability (Figure 5-14a). It is worth noticing that JS 3 that represents overhanging configures a safer situation compared to JS 1, but only in terms of failure mechanism. This can be explained because JS 3 is not parallel to the slope orientation but rather it dips towards the slope (Figure 5-14b). However, this joint set as well as JS 4 are lateral cracks and overhangs in the rock mass and contribute to an unsafe situation due to lack of support in the rock mass. The blocks detached in these areas slide on the slope surface and account for rockfall susceptibility. Therefore, these joint sets will be also considered as indicators of overhanging in the susceptibility analysis. (Section 5.3.1)

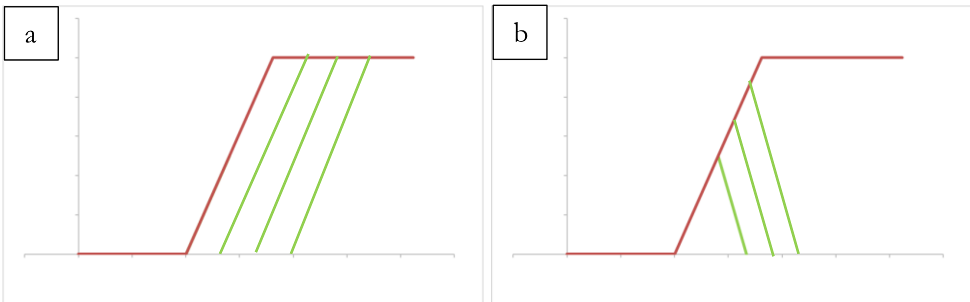

Figure 5-14. Schematic profile of the slope (red) and the joint set orientation (green). JS 1 (a) is parallel to the slope and therefore configure a more unstable situation compared to JS 3 in terms of failure mechanism alone (b). No scale.

5.3. Rockfall Susceptibility Assessment

The rockfall susceptibility assessment in this work uses the following indicator: minimum normal spacing between joints, joint persistence in the maximum length, SMR, and the presence of overhanging (Section 4.4). First, the results of each indicator are presented separately in the 3DPC according to the methodology described in section 4.4 followed by their integration as scoring for the susceptibility assessment. All the joints were used for this analysis except those belonging to JS 1. The reason why is that these joints are the most dominant in the slope (Figure 5-1b and Table 5-2) and represent the sliding plane, as the platy limestone detaches in platy layers. Thus, given that majority of the slope consists of sliding planes (unstable) it would not be useful to distinguish susceptibility levels. This is valid only for this case study, but for others were the slope surface is different than the sliding plane it would make sense to include all the joints.

5.3.1. Overhanging Indicator

There are 3 main overhanging areas located on the left side of the rock slope (Figure 5-15): one in the upper part, almost 14 m height (Figure 5-16a), and two close to the bottom below 3 m height (Figure 5-16b). The surfaces of overhanging are well delineated in most of the cases, except for less flat surfaces as shown in few parts in the bottom. The joint sets which contain overhanging are JS 3 with 11 clusters and JS4 with 9 clusters, manually classified with *scalar field* 1.

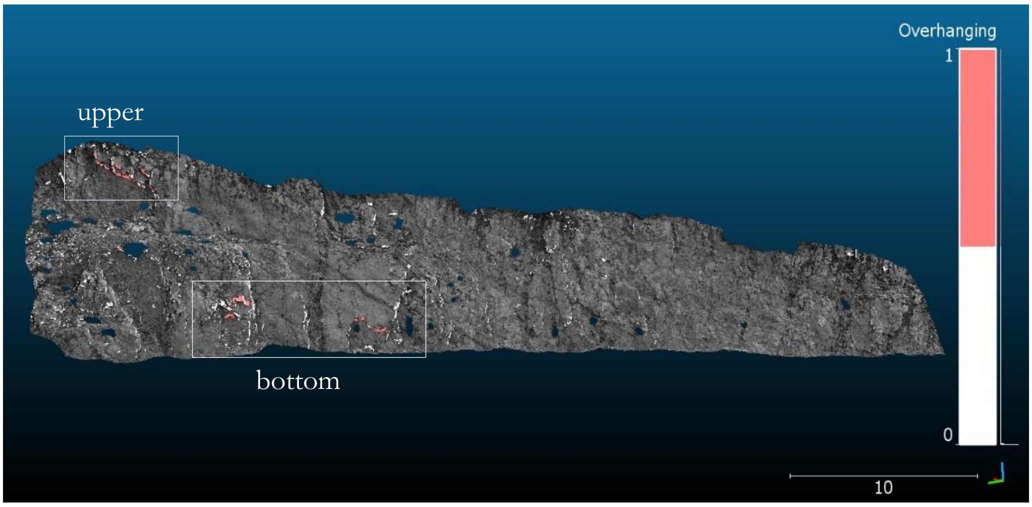

Figure 5-15. RGB 3DPC with the location of joints as overhanging (red-1) compared to non-overhanging joints (white – 0). Scale in meters.

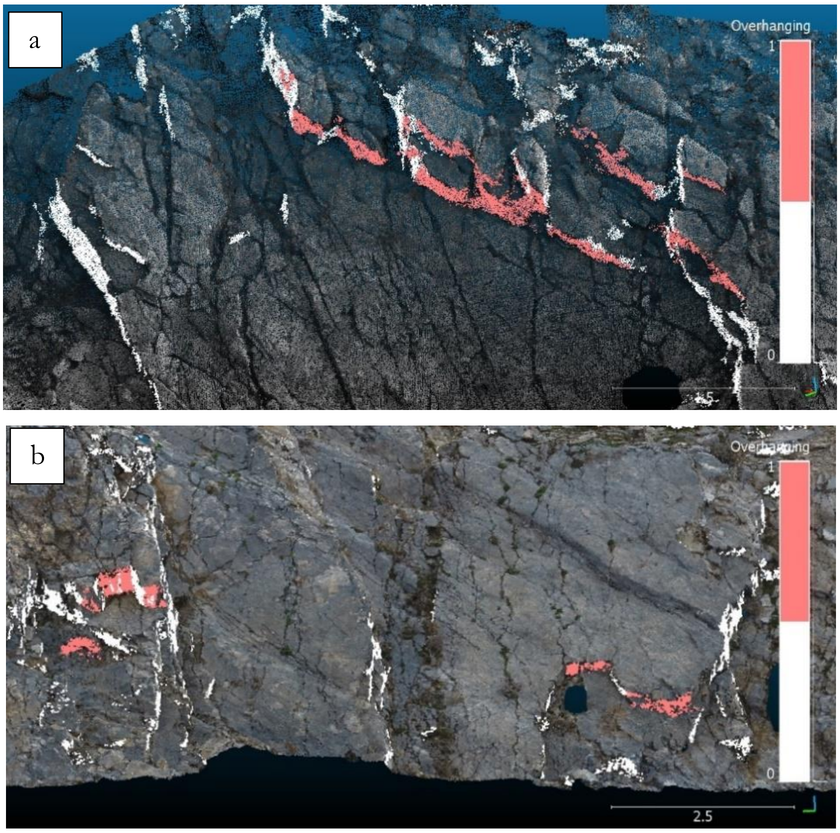

Figure 5-16. Closer view of the upper overhanging (a) and the two lower overhanging (b) areas in pink(1). In white (0) are all the non-overhanging joints. Scale in meters.

5.3.2. Spacing Indicator

In terms of rock mechanics, the less the spacing between the joints set the more fragmented the rock mass will be and thus of poor quality. This can lead to rock detachment and therefore configures a higher rockfall susceptibility compared to larger spacing between joint set. To account for the worst-case scenario, the minimum normal spacing was considered whenever a cluster presented more than one value. This situation can be more easily understood in taking cluster 26 of JS 2 as an example. The DSE software computed to normal spacing for cluster 26 to cluster 118 on its right side (0.48 m) and to cluster 18 on the left side (2.26 m). If the minimum spacing is used for cluster 26, all its points will be reddish since it will relate to the closest cluster 118 (Figure 5-17) whereas if set as maximum spacing, cluster 26 will be yellow since it will relate to the further cluster 18 (Figure 5-18).

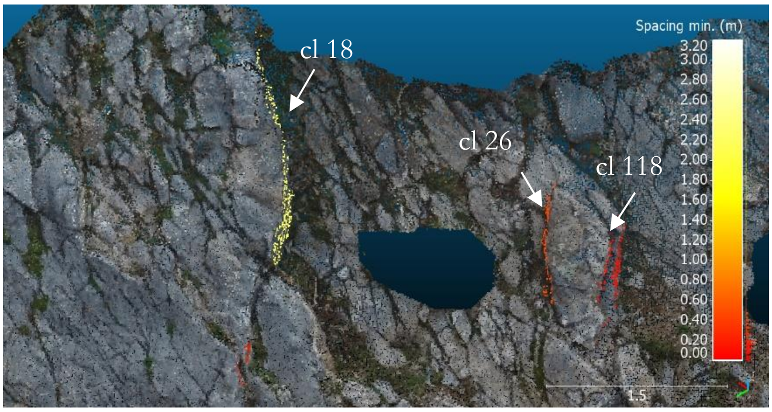

Figure 5-17. Relationship of neighbouring clusters to cluster 26. The minimum normal spacing is to cluster 118 on the right side. In this scenario, cluster 26 contributes to higher rockfall susceptibility (reddish).

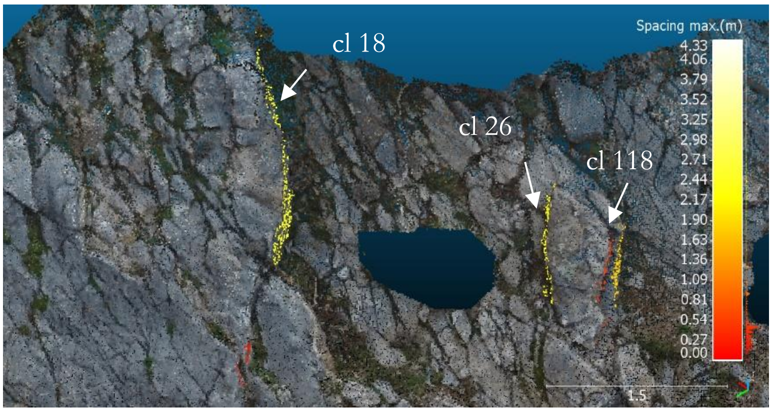

Figure 5-18. Relationship of neighbouring clusters to cluster 26. The maximum normal spacing is to cluster 18 on the left side. In this scenario, cluster 26 contributes to lower rockfall susceptibility (yellowish) compared to Figure 5-17. Scale in meters.

After applying the minimum normal spacing for each cluster for joint sets 2, 3, and 4, the final spacing indicator in a 3D space is obtained (Figure 5-19). The rock slope has the majority of the joint set with minimum normal spacing on the left side (bottom and top), mainly up to 0.32 meters. Few joints have a higher value of minimum spacing (yellowish) in the center and to the right side on the rock slope, greater than 2 meters.

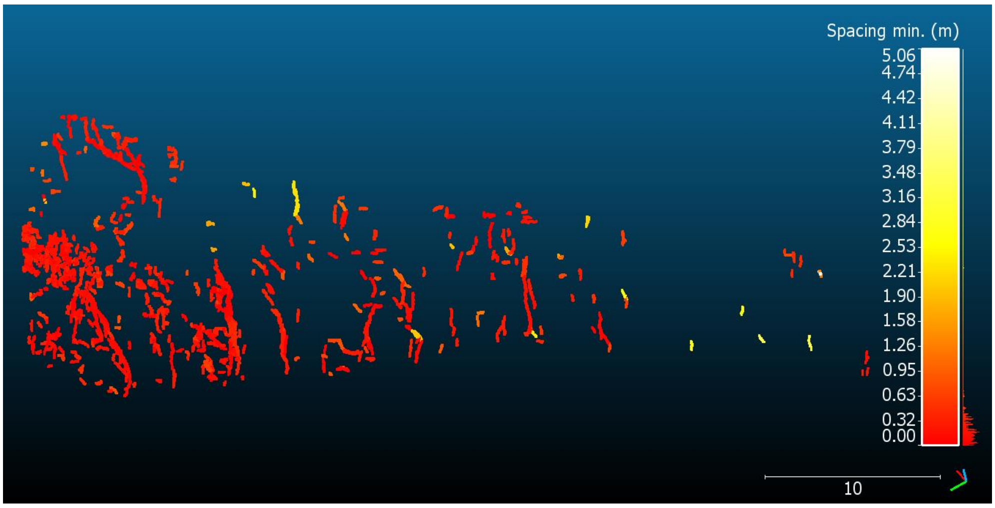

Figure 5-19. 3D distribution of joints (clusters) in the rock slope colourized by the minimum normal spacing. Lower values (red) are indicator of higher susceptibility spots for rockfall. Histogram next to the colour ramp and scale in meters.

5.3.3. Persistence Indicator

The persistence of joints inside the rock mass (trace length) also contributes to its quality since higher persistence decrease the shear strength of joints. In other words, it facilitates the breakage of rock mass since lower strength is required for joint displacement. Although only the persistence of exposed surfaces is considered in this work, the idea is to evaluate if it can also be used as an indicator for rockfall susceptibility. To account for a conservative scenario, the maximum length of persistence computed by DSE software was assigned to each cluster individual cluster of joint sets 2, 3, and 4 as *a scalar field* in *CloudCompare* (Figure 5-20). Differently from the spacing, the distribution of persistence is more spread as seen in the histogram (0.14 to 1.47 mainly) and the joints with higher persistence are in the central area of the slope.

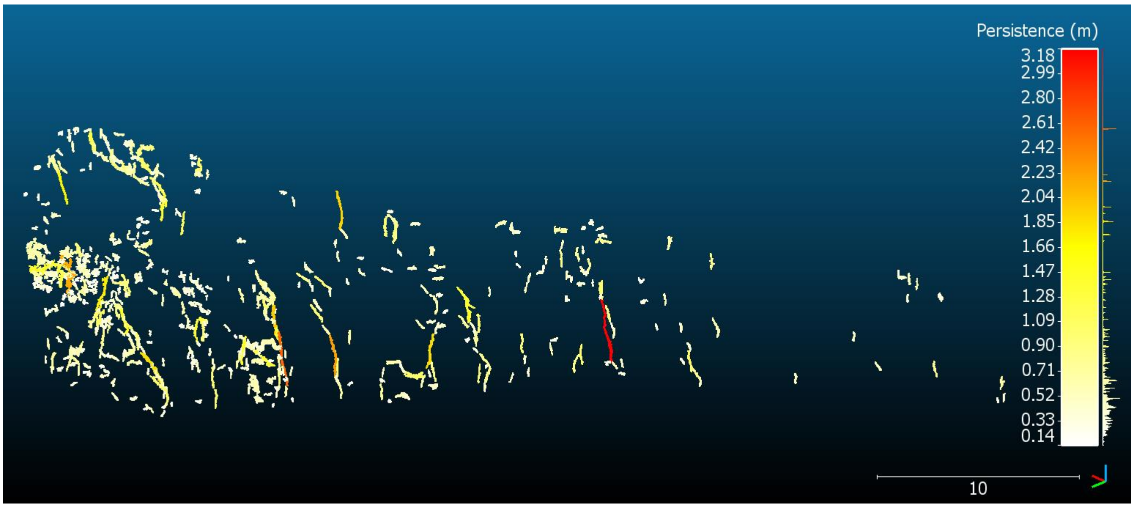

Figure 5-20. 3D distribution of joints (clusters) in the rock slope colourized by the maximum persistence. Higher values (red) are indicator of higher susceptibility spots for rockfall. Histogram next to the colour ramp and scale in meters.

5.3.4. SMR indicator

The SMR is also useful as an indicator for rockfall susceptibility because it assesses the stability of a slope according to the angular relationship between joints to the slope surface (parameter F_1, F_2, and F_3 – Table 5-10). After calculating the SMR using the SMRTool, the results are as follows: classes I for JS 2 and JS 3 (completely stable) and class II for JS 4 (stable). In this methodology, all the clusters (joints) belonging to

JS 2 and JS 3 were assigned also as class I, and all the clusters of JS 4 were assigned as class II (Figure 5-21). The rock slope has both classes I and II, mainly concentrated on the left side, indicating the possibility of planar failure (Table 5-10). This is plausible because even thought classified as stable, some of these classes account for overhanging (Figure 5-22): on the upper part, the overhanging has both classes (Figure 5-22a) while in the lower part it mainly has class II (Figure 5-22b, c).

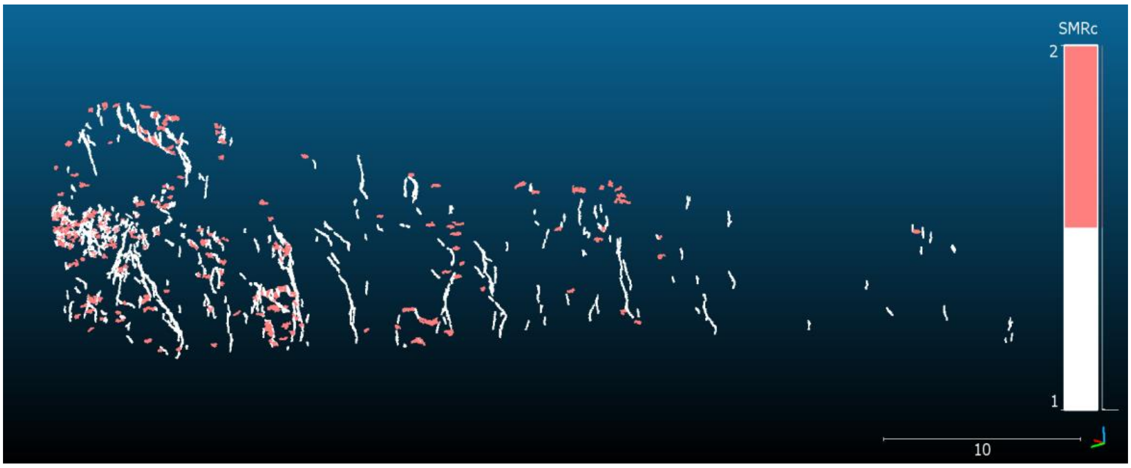

Figure 5-21. 3D distribution of joints (clusters) in the rock slope colourized by SMR class I (white) and class II (pink). Scale in meters.

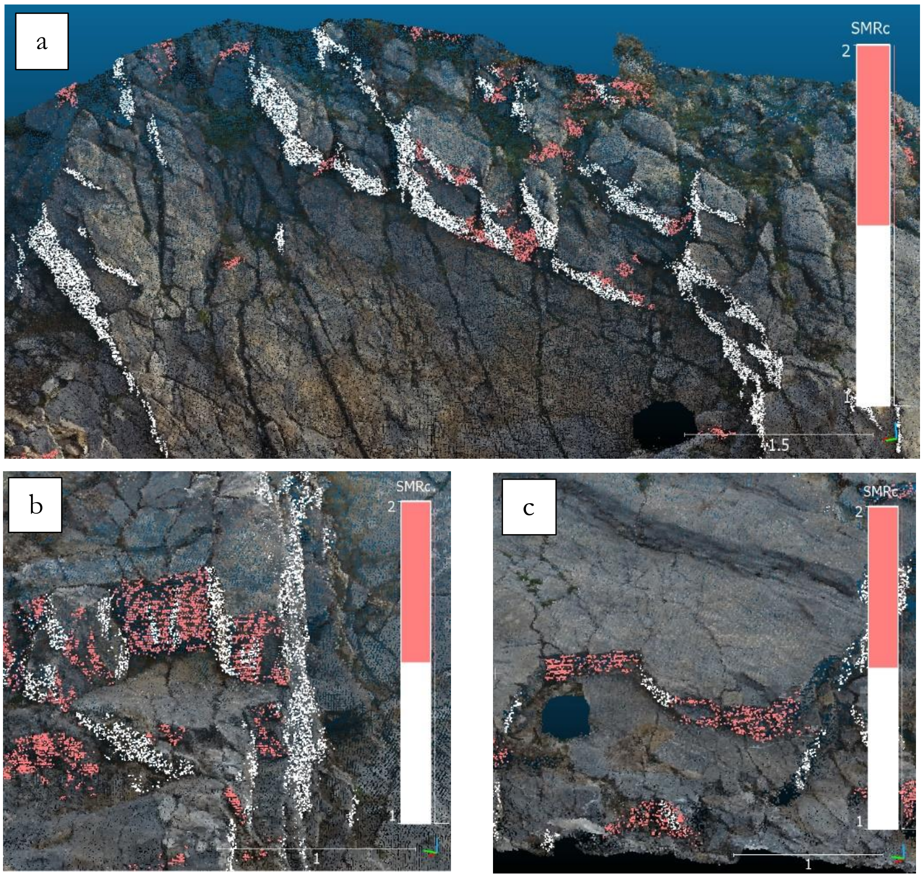

Figure 5-22. 3D distribution of joints (clusters) in the overhanging parts of the slope, colourized by SMR class I (white), and class II (pink). In the upper part (a) the overhanging has both classes whereas the lower part (b and c) has mainly class II. Scale in meters.

5.3.5. Rockfall Susceptibility Index

The four rockfall susceptibility indicators were calibrated mainly using the same areas of the slope with overhanging, which are visually indicative of higher susceptibility (Figure 5-16). The reason is that for this case study where the most dominant joint set (JS 1-Figure 5-2) is parallel to the slope surface and therefore configures the entire slope as partially stable (Figure 5-14a), the presence of overhanging is a differential factor determining the falling of blocks. It means that the lack of support rather than kinematic stability analysis plays a major role in rock detachment for this particular case. As to account for that, overhanging joints were given a value of 2 as high susceptibility.

Lower spacing and higher persistence was given also a value of 2. For SMR, Class I was considered as low susceptibility (0) since its description is completely stable with no failures according to Romana (1993). Class II (stable) and III (partially stable) are described as some failure of blocks and thus given a value of moderate. The remaining classes VI (unstable) and V (completely unstable), even though not present in this study area, where given as a high susceptibility. This SMR division could be of usage in other rock slopes in which theses classes are present. The final scoring of indicators after calibration is presented in Table 5-11, which are summed up to 7 to provide the Rockfall Susceptibility Index I_{RFS} for each joint (cluster)[4] according to Eq.(16). In this work, I_{RFS} is classified as high from 7 to 5, moderate from 5 to 3 and low below 3.

Table 5-11. Scoring of indicator for Rockfall Susceptibility Assessment.

Indicators	Scores		
	High (2)	Moderate (1)	Low (0)
I_S (spacing)	< 0.50 m	0.50 m– 1.00 m	> 1m
I_P (persistence)	> 1m	1 – 0.50m	< 0.50 m
I_{SMR}	Classes VI and V	Class II and III	Class I
$I_{overhanging}$	present	n.a.	absent

n.a: not applicable

The 3D visualization of the I_{RFS} shows areas of higher susceptibility in the left part of the rock slope (Figure 5-23). The areas of overhanging (bottom and upper part) show moderate to high susceptibility depending on the persistence and spacing of joints (Figure 5-24). It is worth noticing that the persistence of exposed surfaces is indeed a useful indicator since it contributes to the differentiation of susceptibility levels within the overhanging areas. In other words, the greater the extension of lack of support (persistence of overhanging) the more prone to rockfall it will be compared to smaller areas, an indication of larger unstable volumes.

[4]The total would be 8 if SMR classes VI and V were present in this case study.

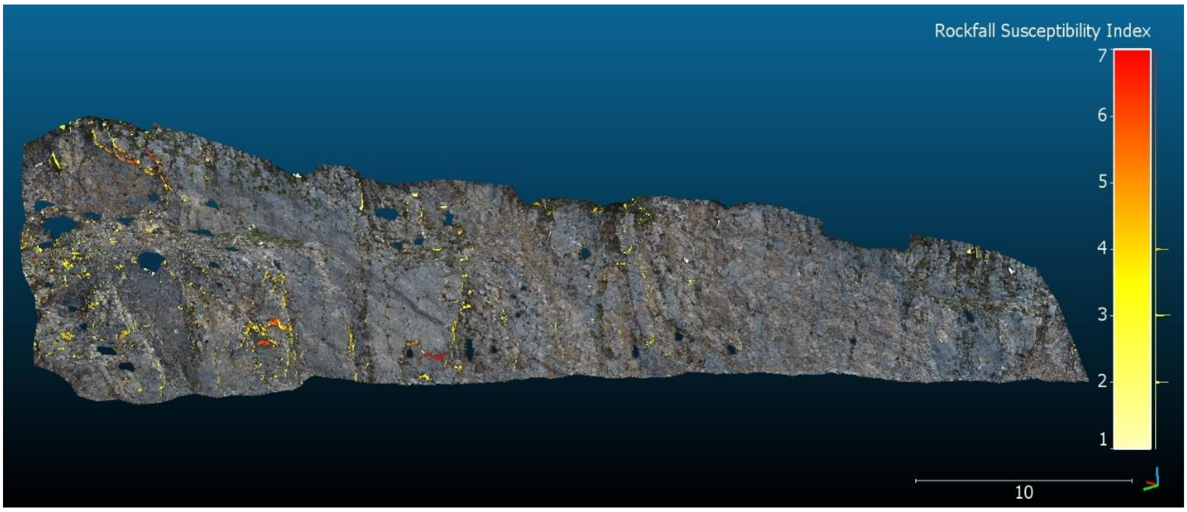

Figure 5-23. 3D distribution of the Rockfall Susceptibility Index in the rock slope. Areas of moderate (3-5) and high (5-7) susceptibility are mainly in the left part of the slope. Scale in meters.

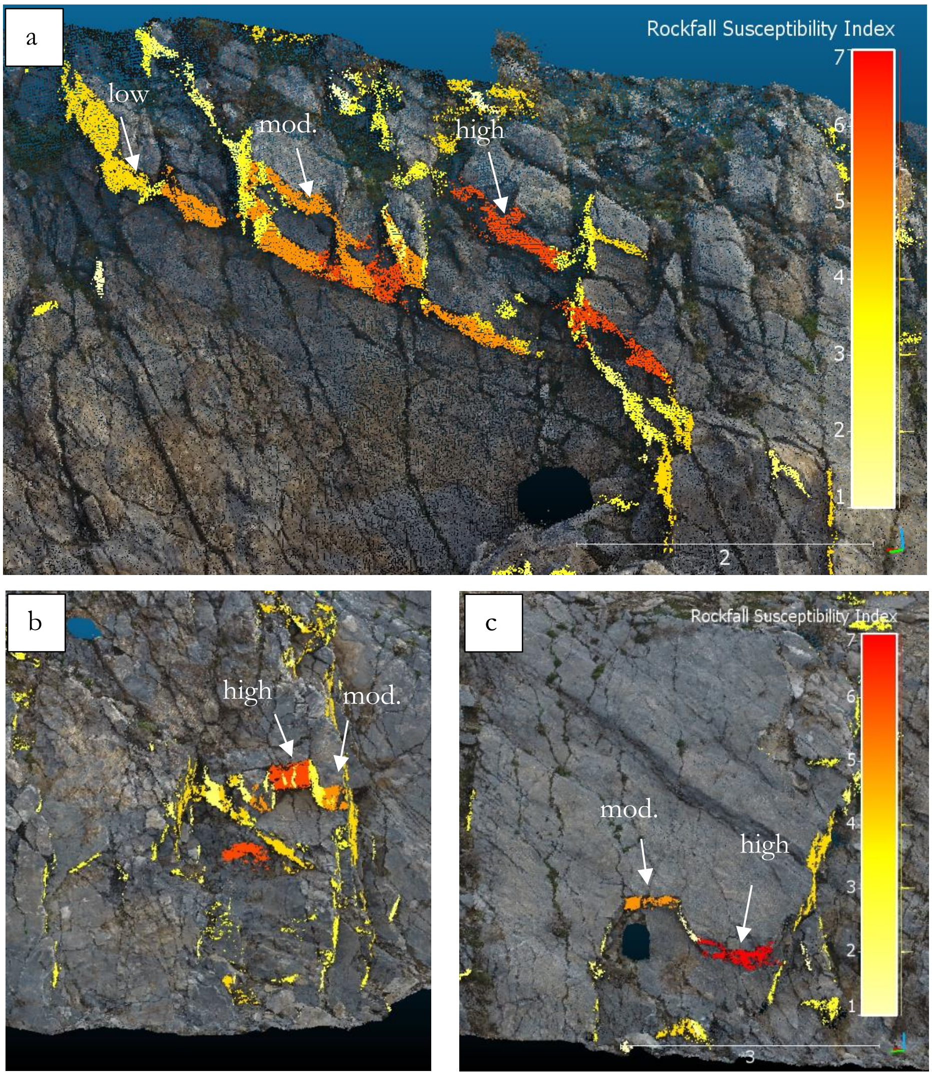

Figure 5-24. Overhanging areas in the upper (a) and bottom (b, c) of the rock slope, differentiated in terms of susceptibility due to spacing and persistence properties. Scale and colour bar identical for (b) and (c).

In the lateral view of the 3D rock slope, there are several areas with moderate susceptibility represented by the joints with higher persistence (Figure 5-25). Although they do no reduce the rock mass shear strength (not trace length), the persistence of exposed surfaces, in this case, shows previous breakages of rocks that were once part of the continuous slope surface. This inference is based on the observation of the right part of the slope were fewer lateral exposed surfaces are present and as a consequence, the surface of the slope is more continuous.

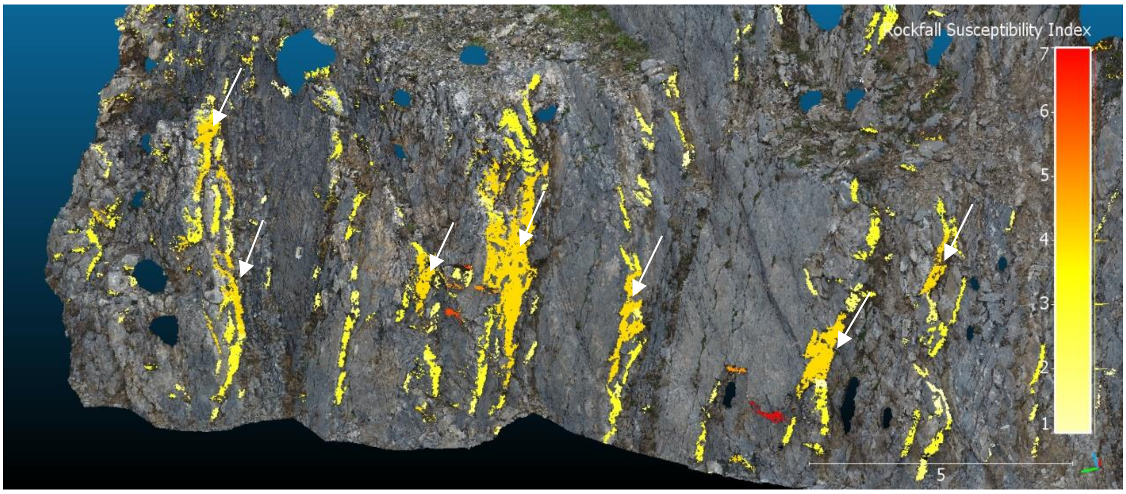

Figure 5-25. Moderate susceptibility areas (dark yellow) as lateral exposed surfaces (white arrows) on the left part of the rock slope. Scale in meters.

6. DISCUSSION

6.1. Validation and uncertainties of the Rockfall Susceptibility Index

Similarly to Dunham et al. (2017), the validation of the susceptibility assessment was carried out qualitatively by visual inspection from field observation and photographs. The areas of high and moderate I_{RFS} correspond to the areas where most fallen blocks are observed, that is, on the bottom left and center of the slope (Figure 6-1) and below overhanging joints (Figure 5-10). In contrast, the right side with a more continuous slope surface has fewer and smaller blocks compared to the left side. Thus, the approach proposed in this thesis for identifying source areas prone to rockfall shows good results.

Notwithstanding, improvements can be done. For instance, a quantitative and more accurate validation could be performed if another 3DPC of the slope was available on a later date. This would allow computing the change detection is the slope due to fallen blocks and afterward check how many areas of previous identified high and moderately susceptibility matches those scars of rockfall, as proposed by Matasci et al. (2018). Complementary, the application of I_{RFS} in a larger scale rock slope would also be beneficial to evaluate the minimum number of areas needed for calibration in order to haver a higher accuracy. This evaluation was not possible in the studied rock slope due to its scale. Finally, another type of validation could be carried out using intermediate scenarios for the indicators and evaluating how different the I_{RFS} would turnout to be compared to the worse case scenario presented in this thesis.

This work lacks a method to compute and visualize uncertainties similar to previous rockfall susceptibilities for 3DPC in the literature. Unlike susceptibilities maps where uncertainties are commonly presented, for 3DPC the uncertainties are rarely dealt with in recent papers. For instance, Matasci et al. (2018) developed a rockfall susceptibility approach for overhanging slopes in 3DPC with validation but no computation of uncertainties. Neither did Zhang et al., (2019) when applying the rockfall susceptibility assessment in Augmented Reality (AU). Dunham et al. (2017) mention that the main source of uncertainty of their Rockfall Activity Index (RAI) is the instability rate r which may vary in time due to climatic fluctuations. Although they state a variation by no more than 20% for r based on preliminary studies, this uncertainty is not incorporated in RAI numerically nor visually presented in the 3DPC. Thus, this issue is still an open field of research.

Figure 6-1. Bottom view of the rock slope with bigger and more fallen blocks in the left part (dashed white line) whereas towards the right the fallen blocks are smaller and less. The white box highlights one of the overhanging of Figure 5-16b.

6.2. Potential and limitations of the proposed methodology

An advantage of the methodology herein proposed is that it does not rely on estimated instability rates based on change detection as Dunham et al. (2017), which has high a degree of variability and uncertainty according to the authors. Moreover, it takes into consideration the geomechanical properties of the rock mass that are not included in the RAI, namely discontinuity orientation and persistence among others used for the SMR calculation. These geomechanical properties are essential for rock mass characterization and stability analysis.

Compared to Matasci et al. (2018), the advantage is the automatic computation of persistence and spacing in the entire 3DPC using the DSE software. These authors compute these geomechanical properties manually using virtual scanlines in parts of the 3DPC as to be representative for each joint set, considering trace length instead of exposed surface. Also, this work presents a novel approach to visualize the spacing and persistence values on the 3DPC and to use as an indicator for rockfall susceptibility. On the other hand, Matasci et al. (2018) provide an automatic routine to detect overhanging and integrate with persistence (as trace length) and spacing for the computation of their proposed Rockfall Susceptibility Index. This is not the case for this thesis in which the indicators require calibration and manual detection of overhanging. It is worth to notice that a common feature in all three works is the use of overhanging as an indicator for rockfall susceptibility, regardless of the approach used (change detection, manually or automatic).

Zhang et al. (2019) use the same routine developed by Matasci et al. (2018) and thus the same comparison above mentioned apply between their study and the one presented here. Although they provided a great step forward by using the rockfall susceptibility routine in augmented reality (AU), the visualization results presented as figures in their publication is less capable of differentiating levels of susceptibility in the rock slope as compared to the figures presented in this work.

A great potential of the methodology is the applicability to other study areas in terms of the development of indicators, the procedure for calibration and integration into I_{RFS}. For instance, even though the studied rock slope did not have SMR class VI and V, it was included in the scoring of indicators (lower susceptibility). Although the rock slope only presented planar failure, the other types (toppling and wedge) are partly incorporated into SMR and thus could be applied to slopes where they occur. The adaptations required for its transferability lies on the scoring of the indicators based on chosen areas for calibration, which are indeed site-specific. However, the logic of giving high scores for higher persistence, low spacing, presence of overhanging and SMR VI and V should remain.

One relevant note when using this approach elsewhere is that the identified areas of higher susceptibility do not guarantee that a rock detachment will occur, but rather that is it more likely compared to other areas of the same rock slope based on indicators. Additional mechanisms not part of the scope of this work might influence the outcomes such as groundwater fluctuation inside the rock mass, ground vibration (naturally or human-induced), and rainfall (Figure 1-1).

Another potential of this methodology is that the original 3DPC is used from beginning to end as new information of indicators is added as a scalar field, without the need for mesh generation and thus interpolation of results. The spacing and persistence indicators consider the local information of each cluster and constitute one of the innovations on this work. The same applies to overhanging where local information is used. The SMR is the only indicator that represents an average since all the clusters of a joint set with a given SMR class also receive the same class, and the spacing and persistence used for the computation are the mean values (Table 5-8).

One main limitation of this work is related to the approach of joint set extraction used in the DSE software. It only extracts joint as an exposed surface instead of trace length. This brings a disadvantage of not using trace length for computing persistence nor normal set spacing, and thus losing valuable information for rock mass characterization. For instance, Cai et al 2004 developed an expression to incorporate non-persistent trace length on block volume calculation to account for the effect of rock bridges. This could not be applied here. Another application is on the proposed I_{RFS}, which might yield different results using trace length for the persistence and spacing indicators instead of exposed surfaces. A further comparison should be carried out to evaluate how different the results are. On the other hand, the use of exposed surfaces brings an advantage to identify different levels of susceptibility for overhanging joints. The persistence considered in this study as maximum length indicates whether the lack of support is greater or smaller and this implies in a more or less susceptibility for rockfall respectively (Figure 5-24). This is also an innovation of the methodology compared to the above mention related studies in the literature.

It is worth to notice also about the intrinsic characteristics of the chosen slope for the application of this approach. The most dominant joint set (JS 1) has the majority of the indicators contributing for a higher rockfall susceptibility: (i) it is parallel to the slope which configures the worst-case scenario for planar failure computed by the SMR, (ii) has the highest persistence as maximum length and (iii) minimum spacing to neighbouring joints. For these reasons, almost the entire slope would be classified as high susceptible whereas, in reality, only specific parts are, i.e overhanging (Figure 5-24) and lateral exposed surfaces (Figure 5-25). It would be helpful to apply this approach in a rock slope with different joint set characteristics to evaluate its performance.

Finally, care should be taken when using the automatic results of spacing and persistence before using them as indicators for the susceptibility assessment. For example, the joints of a given set in the rock slope should be parallel to yield appropriate results for spacing, as suggested by Riquelme et al., (2015). As for the persistence, large clusters are likely to present a large standard deviation on the distance from the point to the best fitting plane as attested here (section 5.1.2). Whenever it happens, the merging of clusters to simulate full persistent joints can wrongly merge clusters that are not coplanar in reality and thus yield unrealistic persistence values. Incorrect values of persistence and spacing can therefore also lead to incorrect indicators, consequently misleading source areas of rock detachment in the susceptibility assessment.

7. CONCLUSION

This work presents a comprehensive and novel methodology for Rockfall Susceptibility Assessment tailored for application to UAV obtained 3D slope models. It consists of 4 major sequential blocks: (i) use of UAV photogrammetry with data acquisition to 3DPC generation, (ii) Feature extraction for rock mass characterization (joint set orientation, persistence, spacing and block volume), (iii) Slope Stability Assessment by using RMR and SMR indexes for each joint set and (iv) development of a Rockfall Susceptibility Index.

The methodology was applied to a rocky slope in a mountainous area of the Samaria Gorge National Park, in Crete Island (Greece). Although only visual validation was performed, the identified areas of higher and moderated rockfall susceptibility in the 3DPC match the areas where the bigger and highest number of fallen blocks, which were found on the foot of the slope. Hence, this approach helps to refine the identification of potential rockfall source areas, which are areas prone to rock detachment compared to their surroundings and to improve the input for hazard assessment, including rockfall run out simulations.

The advances and innovations presented in this thesis are summarized as follows:

- Throughout all the workflow, the generated 3DPC was used from beginning to end as new information of indicators for susceptibility was added. Hence, there is no need for mesh generation and interpolation, which could compromise the quality of the 3D model.
- Besides field data, no other information apart from the 3DPC is required to develop the index. Thus, this method provides a cheap, efficient, and less time-consuming procedure compared to traditional field surveys or avoids occlusion commonly present in TLS surveys. A single UAV campaign is sufficient to collect data for further processing and analysis at the office. The calibration of the proposed index does not require change detection, which would imply multiple campaigns for a time series point cloud generation.
- An alternative approach to estimate the RQD directly from 3DPC was proposed, validated by the well-established correlation to volumetric joint count J_V proposed by Palmstrom (2005). This approach can be useful when no other information is available, only the 3DPC.
- A semi-automatic procedure for block volume calculation locally in 3DPC was proposed, applicable for flat and exposed surfaces of a rock mass where block shapes are regular (i.e volume = area x height). These volumes reflect the actual block volume on the rock mass.
- A novel procedure to visualize spacing, persistence, and SMR information on the 3DPC was proposed. Up to date, no publication has addressed this issue. The spacing and persistence reflect local information for each cluster (joint) whereas the SMR is an average for all the clusters of a given joint set. Furthermore, a step by step procedure provided on how to integrate these indicators (and overhanging) for the Rockfall Susceptibility Assessment.
- Indirect incorporation of volume in the Rockfall Susceptibility Assessment by considering the persistence of exposed surface as maximum length. For the overhanging areas, this procedure allows the differentiation of parts with a larger lack of support them others, and as a consequence an indication of a greater volume of rock that is prone to rockfall.

7.1. Answer to research questions

Research objective 1

a. How can geomechanical properties be extracted from UAV point clouds? b. Among them, which ones are extracted automatically, and which ones manually?

The geomechanical properties considered in this work are the joint set orientation (dip direction and dip angle), normal spacing, persistence (strike, dip, maximum length and area of convex hull), block volume (mean or locally) and overhanging. The DSE software allows the semi-automatic extraction of joint set orientation and automatic for spacing and persistence. For the joint set orientation, the original 3DPC is classified in a joint set whereas for the spacing and persistence the information is not plotted but given as a *.txt* file. The visualization of this information (and also SMR) is one of the contributions of this work.

The mean block volume calculation uses as input the mean normal set spacing whereas for the local block volume calculation the inputs are the persistence (area of convex hull) and spacing between neighbouring cluster. For this latter, the user is required to check these values given in the *txt.* files provided from DSE software and thus is a semi-automatic procedure. The overhanging joints are manually identified by checking on the RGB 3DPC which clusters of joint sets extracted by the software correspond to overhanging.

c. For those extracted manually, is it possible to automatize them? If yes, what are the procedures to follow?

The visualization of persistence and spacing information in 3DPC although being an innovative approach was carried out by manual manipulation in *Excel* of the *.txt* files provided by the DSE software. This procedure took couple hours and could be automated via an algorithm in any computer language (similar to the pseudocode of Figure 4-7) or directly as a MATLAB script on the DSE software since it is open-source software, written in this language. The procedure to automatize can be the same as the one presented in Section 4.2.2 for the persistence indicator and Section 4.2.3 for the spacing indicator, but a generic procedure is also given below.

For the persistence, the required *.txt* files are:

File #1: XXX_xyz-js-c-abcd.*txt* - *report_persistence* (where XXX is the name given by the user, xyz are the 3D coordinates of a point, js is the joint set the point belong to, c is the cluster id the points belong to and abcd are the plane equation parameters of the cluster). This file is the output of the automatic persistence computation from DSE software

File #2: XXX_xyz-js-c.*txt* (where XXX is the name given by the user, xyz are the 3D coordinates of a point, js is the joint set the points belongs to and c is the cluster id the points belong to). This file is the output from the semi-automatic joint set extraction in DSE software.

(i) Open File #1 and select the value of persistence in the column named *max* (correspond to the maximum length) for a given cluster.

(ii) Paste this value in a newly created column of persistence of File # 2 in the same line of the corresponded cluster for a given joint set. The cluster id is the link to transfer information between the two files.

(iii) Open File #2 in *CloudCompare* selecting the column of persistence as a *scalar field.*

For the spacing, the required *.txt* files are:

File #1: js-x-nfp(or fp)-cl1-cl2-s-D1-D2.txt (where x is the joint set number 1,2,3…, nfp stands for non-full persistent scenario (= non-persistent joints) and fp stands for full persistent (= persistent joint set), cl1 and cl2 are the neighbouring clusters for which the normal spacing is calculated, s is the normal spacing between cl1 and cl2, D1 and D2 are the parameter D of the plane equation for cl 1 and cl2 respectively).

File #2: XXX_xyz-js-c.*txt* (where XXX is the name given by the user, xyz are the 3D coordinate of a point, js is the joint set the point belongs to and c is the cluster id the point belong to)

(i) Open File #1 and select the value of minimum normal spacing in the column named s for a given cluster id. The one cluster can have more than one normal spacing value so the minimum value has to be selected.

(ii) Paste this value in a newly created column for the spacing of File # 2 in the same line of the cluster id. The cluster id is the link to transfer information between the two files.

(iii) Open File #2 in *CloudCompare* selecting the column of persistence as a *scalar field*.

Finally, the manual identification of cluster which corresponds to overhanging is feasible in small scale slope (< 50m extension for instance) such as the one used in this work. However, for larger scales (hundreds of meters), the computational routine developed by Matasci et al., (2018) is more suitable.

Research objective 2

a. Which methods, which are available in the literature for Rockfall Susceptibility Assessment, can be adapted to use features extracted from 3DPC?

The mean normal set spacing, mean joint set persistence, and RQD extracted from the 3DPC can be used first for the RMR computation of each joint set, followed by the computation of SRM. This latter is useful to evaluate the slope stability in terms of kinematic analyses, i. e angular relationship between joint and slope orientation as described in Section 2.2.2. Even though the SMR was not a major factor to identify source areas of rockfall in this work given the intrinsic particularities of the rock slope, it could be useful for rock slopes with a different configuration of joint set orientation (i.e not parallel to the slope).

The outputs from DSE software were also adapted to derive local block volume calculation as stated in research question 1b.

b. Which indicators can be developed using the extracted features from 3DPC? c. How can these indicators be quantified in a reproducible way?

This work presents a methodology to develop and quantify indicators for the spacing, persistence, overhanging, and SMR (Section 4.4.1 to 4.4.4). The spacing, persistence, and overhanging indicators contain local information of a particular cluster (joint) in the 3DPC. For instance, if a cluster has a computed persistence of 20 m, this value will be given only to this cluster. Therefore no averaging or extrapolation is carried out. The SMR is the only indicator that can be considered to be an average since it is computed for all the clusters in a given joint set and not individually.

Research objective 3

a. What is the weight of each indicator?

The four indicators considered in this work (overhanging, persistence, spacing and SMR) were given the same weight to account for the Rockfall Susceptibility Index I_{RFS}, in line with recent publications (Section 4.4.5 – step iii). The advantage of this approach is to make it more generic and thus applicable to other case studies whereas the disadvantage is that given the particularities of a rock slope, an indicator might not be as useful to account for rockfall susceptibility compared to others as attested for the SMR in this thesis.

b. How can the output of this index be classified?

The four indicators were scored into low (0), moderate (1), and high (2) susceptibility according to their contribution to the quality of the rock mass (spacing and persistence), stability of the slope (SMR), and lack of support (overhanging). The I_{RFS} thus can range from 0 to 8 but particularly for the rock slope understudy the maximum value is 7 since no joint set is considered as SMR classes VI or V. The I_{RFS} was then classified as 7 to 5 for high susceptibility, 5 to 3 as moderate, and 3 to 0 as low (Section 4.4.5 – step iii). Theoretically, it can also be replicated to other rock slopes just setting from 8 to 5 as high susceptibility. Since the methodology was applied and validated for only one case study, further validation in other rock slope are needed.

c. How can this index be fed back in the 3DPC, showing areas with different susceptibility levels?

The I_{RFS} can be fed back in the 3DPC similarly to the process described for the susceptibility indicators, where for each cluster a value is given as a new column in a *.txt* file containing the 3D coordinates of points and then opened in *CloudCompare* selecting this column as a *scalar field* (Figure 4-12).

d. How to calibrate and validate this index with data collected in the study area?

The calibration of the susceptibility indicator is the key aspect before their integration into the I_{RFS}. This is performed by choosing areas on the 3DPC with different rockfall susceptibility levels based on visual observation and then evaluating how each indicator is characterized there (Section 4.4.5 – step ii).

The validation can be performed qualitatively as presented in this work or quantitatively. The qualitatively is more applicable when only one UAV campaign on a single date is carried out. In this case, during the campaign areas with deposition of fallen blocks in the foot slope should be recorded for example by photos. It is important to keep the fallen blocks in a broader context of the rock slope when taking the photos as to be able to locate them and thus check if their position corresponds to the identified areas of higher rockfall susceptibility on the 3DPC (Figure 6-1). If more than one campaign is possible, then a quantitative and more accurate validation can be carried out by change detection of 3DPC in a time series analysis: the changes should reflect areas of rock detachment (scars) and be compared directly with the previous higher susceptibility areas in an earlier date.

e. What are the assumptions and limitations to apply this index in other study areas?

The main limitation on the development of the I_{RFS} is that it does not incorporate joint set as trace length in all the indicators for susceptibilities. As previously stated (Section 4.2.1 and 6.2), trace length (joints inside the rock mass) are important geomechanical parameters for rock mass characterization of spacing, persistence, and block volume. This limitation is due to the intrinsic process of joint set extraction as a plane by the DSE software instead of lines. The concept proposed in this thesis can also be carried out using trace lengths to develop the I_{RFS}. The results could then compared to the I_{RFS} using joints as exposed surfaces to evaluate the differences and similarities of both approaches.

The methodology herein presented for rock mass characterization, development of indicators for rockfall susceptibility, calibration and integration into a I_{RFS} applies to other studies areas based on the assumption that the mechanism governing the rockfall activity are the same. However, for the studied slope failure occurs where overhangs, thus lack of support of the rock mass are present. The visualization of results in areas with other failure mechanisms has not been studied here. In principle, this should not limit the application since the indicators considered here are widely applied to evaluate rock mass quality (spacing and persistence), slope stability (SMR for failure mechanisms), and lack of support (overhanging). In areas where additional factors are of greater influence for rock detachment such the triggering factors (Figure 1-1), the applicability of this methodology is not enough. Finally, the calibration of indicators is also site-specific.

7.2. Suggestions for future works

Given the findings and limitations outlined in this thesis as well as recent literature related to this topic, the following research topics are put forward:

- Further validation of the methodology presented herein in rock slopes with different joint set configuration. In other words, this should include case studies in which: (i) the most dominant joint set is not parallel to the slope, (ii) all the SMR classes are present in the slope, from V to I, and (iii) toppling and wedge failure mechanism occurs. Additionally, quantitative validation should also be conducted in either of these two ways: (i) checking if the areas of higher rockfall susceptibility identified in an earlier stage match the scars of rock detachment from a latter date or (ii) computing change detection from 3DPC in a time series analysis and checking if the areas with loss of points correspond to the higher susceptibility areas in the initial 3DPC.
- Rock mass characterization based on trace length as joints instead of exposed surfaces, followed by the development of rockfall susceptibility indicators. Some of the available methods to extract trace length in 3DPC that can be used are from Sturzenegger et al. (2011), X. Li et al. (2019), and Guo et al. (2019). Particularly, Sturzenegger et al. (2011) developed a methodology to estimate trace length intensity tailored for TLS. Trace length intensity is a parameter to account for the discontinuity frequency in a rock mass: higher frequency implies more discontinuity and thus poor rock mass quality. This parameter can be adapted for UAV based 3DPC and used as an indicator for rockfall susceptibility: the higher the trace length intensity in a given area, the more fractured the rock mass is and thus more prone to rock detachment.
- Automatization of the process to visualize persistence, spacing, and SMR information on 3DPC. Based on a MATLAB script, a routine can be created and added to the open-source DSE software to produce a final *.txt* file with that information per cluster. In this way, no manual manipulation of the outputs from this software will be required, providing a more rapid Rockfall Susceptibility Assessment.
- Incorporation of the computation routine for overhanging detection developed by Matasci et al. (2018) as to make the Rockfall Susceptibility Assessment herein proposed more automatic.
- Development of uncertainty analysis for Rockfall Susceptibility Assessment tailored for 3DPC followed by visualization.
- Development of a methodology to incorporate rock mass characterization extracted from UAV 3DPC for a regional Rockfall Susceptibility Assessment, applicable to urban environment and transportation corridors (especially roads). Traditionally, only regional terrain characteristics are considered such as slope angle, geology, and triggering factors. A further step would be on how to zonate the slope according to the susceptibility levels. Ideas can be drawn from the thesis of Sun (2018) on multi-hazard assessment along roads in China.
- Application of the indicators used in this thesis to refine the Rockfall Frequency Index developed empirically by Mavrouli et al., (2019). This adjustment can help to validate their index for other study areas and thus broader its applicability.
- Incorporation of triggering factors (rainfall, vibration, freeze and thaw cycles..) as indicators for frequency in Rockfall Hazard Assessment, since they can also influence rockfall activity besides

the local rock mass characteristics. Ideas can be drawn from D'Amato et al., (2016) dealing with quantification of meteorological factors for rockfall occurrence.

- Incorporation of volume above the overhanging as an indicator of magnitude for Rockfall Hazard assessment. In this thesis, the persistence as the maximum length is used to account for the extension of lack of support in the overhanging areas. However, no quantitative information on volume is considered. The bigger the volume above the overhanging, the more hazardous that portion is. Moreover, there is also the need to estimate semi-(or automatic) block volumes with irregular shapes.
- Incorporation of intensity for a Rockfall Hazard assessment. For instance, the height of points in 3DPC can be an indicator for intensity considering that it will imply higher kinetic energy of fallen blocks (height is used to compute velocity). Hence, the intensity would be useful to distinguish hazardous areas that have the same level of susceptibility: the higher the area is in the rock slope, the more hazardous that portion is compared to an area with the same susceptibility but lower height.

LIST OF REFERENCES

Abellan, A., Derron, M.-H., & Jaboyedoff, M. (2016). "Use of 3D Point Clouds in Geohazards" Special Issue: Current Challenges and Future Trends. *Remote Sensing*, *8*(2), 130. https://doi.org/10.3390/rs8020130

Abellán, A., Vilaplana, J. M., & Martínez, J. (2006). Application of a long-range Terrestrial Laser Scanner to a detailed rockfall study at Vall de Núria (Eastern Pyrenees, Spain). *Engineering Geology*, *88*(3–4), 136–148. https://doi.org/10.1016/j.enggeo.2006.09.012

Abellán, Antonio, Oppikofer, T., Jaboyedoff, M., Rosser, N. J., Lim, M., & Lato, M. J. (2014). Terrestrial laser scanning of rock slope instabilities. *Earth Surf. Process. Landforms*, *39*(November 2013), 80–97. https://doi.org/10.1002/esp.3493

Alameda-Hernández, P., El Hamdouni, R., Irigaray, C., & Chacón, J. (2019). Weak foliated rock slope stability analysis with ultra-close-range terrestrial digital photogrammetry. *Bulletin of Engineering Geology and the Environment*, *78*(2), 1157–1171. https://doi.org/10.1007/s10064-017-1119-z

Barton, N., & Choubey, V. (1977). The shear strength of rock joints in theory and practice. *Rock Mechanics and Rock Engineering*, *10*(1–2), 1–54. https://doi.org/10.1007/BF01261801

Bieniawski, Z. T. (1973). Engineering Classification of Jointed Rock Masses. *Transactions of the South African Institution of Civil Engineers*, *15*(12), 335–343.

Buyer, A., Aichinger, S., & Schubert, W. (2020). Applying photogrammetry and semi-automated joint mapping for rock mass characterization. *Engineering Geology*, *264*(October 2019), 105332. https://doi.org/10.1016/j.enggeo.2019.105332

Cai, M., Kaiser, P. K., Uno, H., Tasaka, Y., & Minami, M. (2004). Estimation of rock mass deformation modulus and strength of jointed hard rock masses using the GSI system. *International Journal of Rock Mechanics and Mining Sciences*, *41*(1), 3–19. https://doi.org/10.1016/S1365-1609(03)00025-X

Chen, N., Kemeny, J., Jiang, Q., & Pan, Z. (2017). Automatic extraction of blocks from 3D point clouds of fractured rock. *Computers & Geosciences*, *109*(August), 149–161. https://doi.org/10.1016/j.cageo.2017.08.013

CloudCompare (version 2.10) [GPL software]. (2020).

D'Amato, J., Hantz, D., Guerin, A., Jaboyedoff, M., Baillet, L., & Mariscal, A. (2016). Influence of meteorological factors on rockfall occurrence in a middle mountain limestone cliff, *16*, 719–735. https://doi.org/10.5194/nhess-16-719-2016

DJI. (n.d.). Phantom 4 - DJI's smartest flying camera ever. Retrieved September 21, 2019, from https://www.dji.com/nl/phantom-4?site=brandsite&from=insite_search

Dunham, L., Wartman, J., Olsen, M. J., O'Banion, M., & Cunningham, K. (2017). Rockfall Activity Index (RAI): A lidar-derived, morphology-based method for hazard assessment. *Engineering Geology*, *221*(March), 184–192. https://doi.org/10.1016/j.enggeo.2017.03.009

Fanos, A. M., & Pradhan, B. (2018). Laser Scanning Systems and Techniques in Rockfall Source Identification and Risk Assessment : A Critical Review. *Earth Systems and Environment*, *2*(2), 163–182. https://doi.org/10.1007/s41748-018-0046-x

Fanos, A. M., & Pradhan, B. (2019). A novel rockfall hazard assessment using laser scanning data and 3D modelling in GIS. *CATENA*, *172*(March 2018), 435–450. https://doi.org/10.1016/j.catena.2018.09.012

Ferrari, F., Giacomini, A., & Thoeni, K. (2016). Qualitative Rockfall Hazard Assessment: A Comprehensive Review of Current Practices. *Rock Mechanics and Rock Engineering*, *49*(7), 2865–2922. https://doi.org/10.1007/s00603-016-0918-z

Gigli, G., Morelli, S., Fornera, S., & Casagli, N. (2014). Terrestrial laser scanner and geomechanical surveys for the rapid evaluation of rock fall susceptibility scenarios. *Landslides*, *11*, 1–14. https://doi.org/10.1007/s10346-012-0374-0

Guo, J., Liu, S., Zhang, P., Wu, L., Zhou, W., & Yu, Y. (2017). Towards semi-automatic rock mass discontinuity orientation and set analysis from 3D point clouds. *Computers & Geosciences*, *103*(July 2016), 164–172. https://doi.org/10.1016/j.cageo.2017.03.017

Guo, J., Liu, Y., Wu, L., Liu, S., Yang, T., Zhu, W., & Zhang, Z. (2019). A geometry- and texture-based automatic discontinuity trace extraction method for rock mass point cloud. *International Journal of Rock Mechanics and Mining Sciences*, *124*(September), 1–10. https://doi.org/10.1016/j.ijrmms.2019.104132

Guta, H. E. (2017). *Use of unmanned aerial vehicles compared to terrestrial laser scanning for characterizing discontinuities on rock exposures*. Faculty of Geo-Information Science and Earth Observation, University of Twente.

Hoek, E. (2007). *Practical Rock Engineering*. (E. Hoek, Ed.) (2007th ed.). British Columbia: RocScience.

ISRM. (1978). International society for rock mechanics commission on standardization of laboratory and field tests: Suggested methods for the quantitative description of discontinuities in rock masses. *Int. J. Rock. Mech. Min. Sci. & Geomech. Abstr.*, *15*, 319–368.

Karagiannis, S., & Apostolou, A. (2004). Knowledge Management in Eco-tourism: A Case Study. In D. Karagiannis & U. Reimer (Eds.), *Practical Aspects of Knowledge Management. PAKM 2004. Lecture Notes in Computer Science* (Vol. 3336, pp. 508–521). Springer, Berlin, Heidelberg. https://doi.org/10.1007/978-3-540-30545-3_48

Li, H., Li, X., Li, W., Zhang, S., & Zhou, J. (2019). Quantitative assessment for the rockfall hazard in a post-earthquake high rock slope using terrestrial laser scanning. *Engineering Geology*, *248*(October 2018), 1–13. https://doi.org/10.1016/j.enggeo.2018.11.003

Li, X., Chen, Z., Chen, J., & Zhu, H. (2019). Automatic characterization of rock mass discontinuities using 3D point clouds. *Engineering Geology*, *259*, 105131. https://doi.org/10.1016/j.enggeo.2019.05.008

Manutsoglu, E., Soujon, A., & Jacobshagen, V. (2003). Tectonic structure and fabric development of the Plattenkalk unit around the Samaria gorge, Western Crete, Greece. *Zeitschrift Der Deutschen Geologischen Gesellschaft*, *154*(1), 85–100. https://doi.org/10.1127/zdgg/154/2003/85

Matasci, B., Stock, G. M., Jaboyedoff, M., Carrea, D., Collins, B. D., Guérin, A., … Ravanel, L. (2018). Assessing rockfall susceptibility in steep and overhanging slopes using three-dimensional analysis of failure mechanisms. *Landslides*, *15*(5), 859–878. https://doi.org/10.1007/s10346-017-0911-y

Mavrouli, O., Corominas, J., Ibarbia, I., Alonso, N., Jugo, I., Ruiz, J., … Navarro, J. A. (2019). Integrated risk assessment due to slope instabilities in the roadway network of Gipuzkoa, Basque Country. *Natural Hazards and Earth System Sciences*, *19*(2), 399–419. https://doi.org/10.5194/nhess-19-399-2019

Menegoni, N., Giordan, D., Perotti, C., & Tannant, D. D. (2019). Detection and geometric characterization of rock mass discontinuities using a 3D high-resolution digital outcrop model generated from RPAS imagery – Ormea rock slope, Italy. *Engineering Geology*, *252*(February), 145–163. https://doi.org/10.1016/j.enggeo.2019.02.028

Olsen, M., Wartman, J., McAlister, M., Mahmoudabadi, H., O'Banion, M., Dunham, L., & Cunningham, K. (2015). To Fill or Not to Fill: Sensitivity Analysis of the Influence of Resolution and Hole Filling on Point Cloud Surface Modeling and Individual Rockfall Event Detection. *Remote Sensing*, *7*(9), 12103–12134. https://doi.org/10.3390/rs70912103

Palmstrom, A. (2005). Measurements of and correlations between block size and rock quality designation (RQD). *Tunnelling and Underground Space Technology*, *20*(4), 362–377. https://doi.org/10.1016/j.tust.2005.01.005

Palmström, A. (2001). Measurement and characterization of rock mass jointing. In V. M. Sharma & K. R. Saxena (Eds.), *In-situ characterization of rocks* (pp. 1–40). Rotterdam, The Netherlands: A.A. Balkema publishers.

Pérez-Rey, I., Riquelme, A., González-deSantos, L. M., Estévez-Ventosa, X., Tomás, R., & Alejano, L. R. (2019). A multi-approach rockfall hazard assessment on a weathered granite natural rock slope. *Landslides*, *16*(10), 2005–2015. https://doi.org/10.1007/s10346-019-01208-5

Pix4D documentation. (n.d.). Retrieved May 18, 2020, from https://support.pix4d.com/hc/en-us/articles/202557799-Menu-Process-Processing-Options-2-Point-Cloud-and-Mesh-Point-Cloud

Pix4Dmapper. (2019). Lausanne, Switzerland.

Riquelme, A., Abellán, A., Tomás, R., & Jaboyedoff, M. (2014). A new approach for semi-automatic rock mass joints recognition from 3D point clouds. *Computers & Geosciences*, *68*, 38–52. https://doi.org/10.1016/j.cageo.2014.03.014

Riquelme, A. J., Abellán, A., & Tomás, R. (2015). Discontinuity spacing analysis in rock masses using 3D point clouds. *Engineering Geology*, *195*, 185–195. https://doi.org/10.1016/j.enggeo.2015.06.009

Riquelme, A. J., Tomás, R., & Abellán, A. (2014). SMRTool beta. A calculator for determing Slope Mass Rating (SMR). Alicante: University of Alicante.

Riquelme, A. J., Tomás, R., & Abellán, A. (2016). Characterization of rock slopes through slope mass rating using 3D point clouds. *International Journal of Rock Mechanics and Mining Sciences*, *84*, 165–176. https://doi.org/10.1016/j.ijrmms.2015.12.008

Riquelme, Adrián, Tomás, R., Cano, M., Pastor, J. L., & Abellán, A. (2018). Automatic Mapping of Discontinuity Persistence on Rock Masses Using 3D Point Clouds. *Rock Mechanics and Rock Engineering*, *51*(10), 3005–3028. https://doi.org/10.1007/s00603-018-1519-9

Romana, M. R. (1993). A Geomechanical Classification for Slopes: Slope Mass Rating. In J. A. Hudson (Ed.), *Comprehensive Rock Engineering* (1st ed., pp. 575–600). Elsevier. https://doi.org/10.1016/B978-0-08-042066-0.50029-X

Romana, M., Tomás, R., & Serón, J. B. (2015). Slope Mass Rating (SMR) geomechanics classification: Thirty years review. In *13th ISRM International Congress of Rock Mechanics* (Vol. 2015-MAY, pp. 1–10). Quebec, Canada.

Saroglou, C. (2019). GIS-Based Rockfall Susceptibility Zoning in Greece. *Geosciences*, *9*(163), 21. https://doi.org/10.3390/geosciences9040163

Sarro, R., Riquelme, A., García-Davalillo, J., Mateos, R., Tomás, R., Pastor, J., … Herrera, G. (2018). Rockfall Simulation Based on UAV Photogrammetry Data Obtained during an Emergency Declaration: Application at a Cultural Heritage Site. *Remote Sensing*, *10*(1923), 20. https://doi.org/10.3390/rs10121923

Seidel, M. (2003). *Tectono-sedimentary evolution of middle Miocene supra-detachment basins (western Crete , Greece)*. Universität zu Köln.

Shang, J., West, L. J., Hencher, S. R., & Zhao, Z. (2018). Geological discontinuity persistence : Implications and quantification, *241*(March), 41–54. https://doi.org/10.1016/j.enggeo.2018.05.010

Singh, B., & Goel, R. K. (2011a). Rock Mass Rating. In *Engineering Rock Mass Classification: tunneling, foundations and landslides* (1st ed., pp. 45–62). United States of America: Elsevier. https://doi.org/10.1016/B978-0-12-385878-8.00006-9

Singh, B., & Goel, R. K. (2011b). Rock Material. In *Engineering Rock Mass Classification: tunneling, foundations and landslides* (1st ed., Vol. 1, pp. 13–19). United States of America: Elsevier. https://doi.org/10.1016/B978-0-12-385878-8.00003-3

Singh, B., & Goel, R. K. (2011c). Slope Mass Rating. In *Engineering Rock Mass Classification: tunneling, foundations and landslides* (1st ed., pp. 231–243). United States of America: Elsevier. https://doi.org/10.1016/B978-0-12-385878-8.00018-5

Slob, S. (2010). *Automated rock mass characterisation using 3-D terrestrial laser scanning*. International Institute for Geo-information Science and Earth Observation (ITC).

Spanos, I., Platis, P., Meliadis, I., & Tsiontis, A. (2008). A review on the ecology and management of the Samaria Gorge , a Greek biosphere reserve. *Journal of Geography and Regional Planning*, *1*(2), 19–33.

Sturzenegger, M., Stead, D., & Elmo, D. (2011). Terrestrial remote sensing-based estimation of mean trace length , trace intensity and block size / shape. *Engineering Geology*, *119*(3–4), 96–111. https://doi.org/10.1016/j.enggeo.2011.02.005

Sun, A. (2018). *Development of a rapid multi-hazard assessment along roads: a case study from China*. Faculty of Geo-Information Science and Earth Observation, University of Twente.

Ünlüsoy, D., & Süzen, M. L. (2020). A new method for automated estimation of joint roughness coefficient for 2D surface profiles using power spectral density. *International Journal of Rock Mechanics and Mining Sciences*, *125*(November 2019), 1–9. https://doi.org/10.1016/j.ijrmms.2019.104156

van Veen, M., Hutchinson, D. J., Kromer, R., Lato, M., & Edwards, T. (2017). Effects of sampling interval on the frequency - magnitude relationship of rockfalls detected from terrestrial laser scanning using semi-automated methods. *Landslides*, *14*(5), 1579–1592. https://doi.org/10.1007/s10346-017-0801-3

Vogiatzakis, I., & Rackham, O. (2008). Crete. In I. N. Vogiatzakis, G. Pungetti, & A. M. Mannion (Eds.), *Mediterranean Island Landscapes. Landscape Series* (vol. 9, pp. 245–270). Springer, Dordrecht.

https://doi.org/10.1007/978-1-4020-5064-0_11

Wang, S., Zhang, Z., Wang, C., Zhu, C., & Ren, Y. (2019). Multistep rocky slope stability analysis based on unmanned aerial vehicle photogrammetry. *Environmental Earth Sciences*, *78*(260), 16. https://doi.org/10.1007/s12665-019-8145-z

Westoby, M. J., Brasington, J., Glasser, N. F., Hambrey, M. J., & Reynolds, J. M. (2012). 'Structure-from-Motion' photogrammetry: A low-cost, effective tool for geoscience applications. *Geomorphology*, *179*, 300–314. https://doi.org/10.1016/j.geomorph.2012.08.021

Zhang, Y., Yue, P., Zhang, G., Guan, T., Lv, M., & Zhong, D. (2019). Augmented Reality Mapping of Rock Mass Discontinuities and Rockfall Susceptibility Based on Unmanned Aerial Vehicle Photogrammetry. *Remote Sensing*, *11*(1311), 34. https://doi.org/10.3390/rs11111311

APPENDICES

APPENDIX A – Scanline location

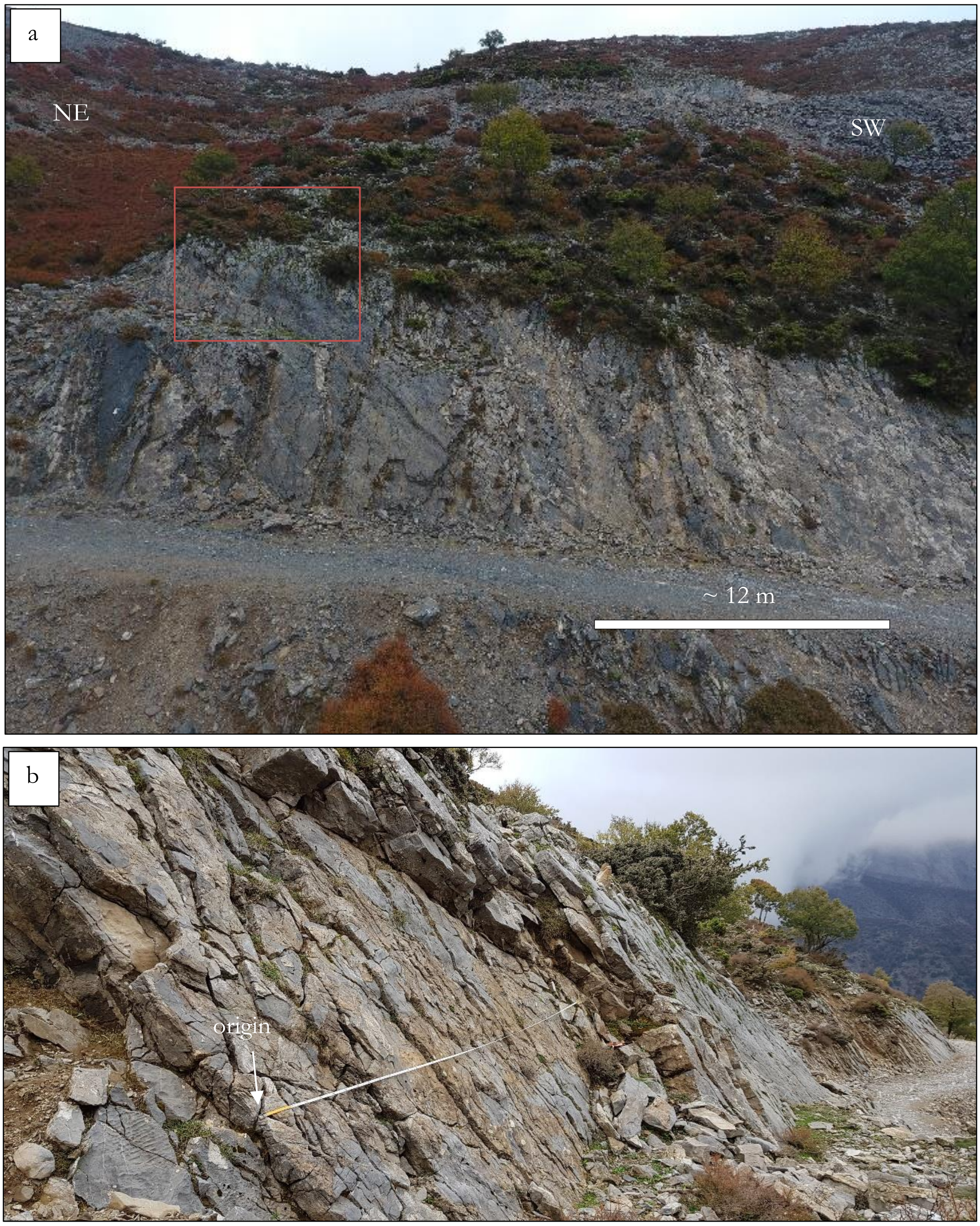

Figure 0-1. (a) UAV RGB image covering part of the rock slope with the location of the scanline in the red box. (b) Detailed view of the scanline in the upper part of the slope, below overhanging. The total length of the scanline is 4 meters, but the survey was done until 1,95 m.

APPENDIX B – Scanline survey data

Table 0-1. Scanline survey data collected in the upper part of the rock slope (Figure 0-1). Bold values were used in Table 5-3.

Distance from origin (m)	Persistence Above|below (m)	Dip dir /dip. angle (°)	Termination Above |below (A – B)	Aperture (mm)	Infilling	Rugosity JRC | ISRM (1978)	Joint set
0	0 | 1.20	216/55	B	40	none	14-16 | Undulating smooth	JS 2
0.10	0.20 | 0.10	240/80	B	10	none	6-8 |Stepped smooth	JS 2
0.20	0.15 | 0.25	54/85	B	5	none	8-10 | Stepped slickensided	JS 2
0.40	0.10 | 1.00	**24/85**	B	20	none	18-20 | Undulating smooth	JS 2
0.60	0.50 |1.00	220/75	B|A	10	none	2-4| Planar smooth	JS 2
0.75	0.70 | 0.10	220/65	B|A	40	none	18-20 | Stepped rough	JS 2
1.00	0 | 0.25	214/70	B	30	none	4-6 | Planar smooth	JS 2
1.40	1.00 | 0.70	214/80	B|A	40	none	8-10| Planar rough	JS 2
1.75	0.53 | 1,40	210/60	B|A	5	none	6-8 | Planar rough	JS 2
1.95	0.73 | 0.15	28/85	B|A	3	none	6-8 | Planar rough	JS 2

Notes:

- Joint sets 1, 3 and 4 were not intersected by the scanline. To account for them, compass measurements were collected in other areas of the slope as follow: JS 1 (**320/55**), JS 3 (**180/50**)
- Persistence: measured the trace length above and below the intersection of the scanline with the joint.
- Termination: how the joint terminates in its extremes above and below. The types of termination present in the rock slope were either at an intact material (A) and/or at another joint (B)
- Rugosity: classified according to Joint Roughness Coefficient (JRC) from Barton & Choubey (1977) and to ISRM (1978)

APPENDIX C – Joint Roughness Classification – Part I

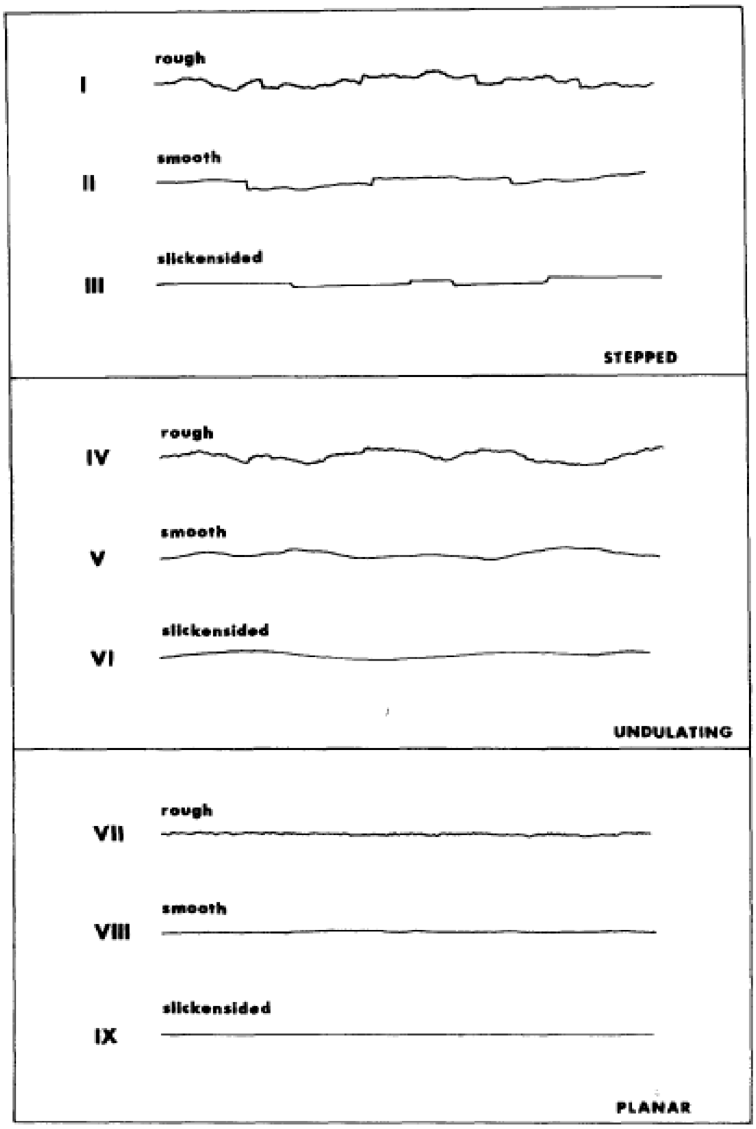

Figure 0-2. Classification of joint roughness according to ISRM (1978).

APPENDIX D – Joint Roughness Classification – Part II

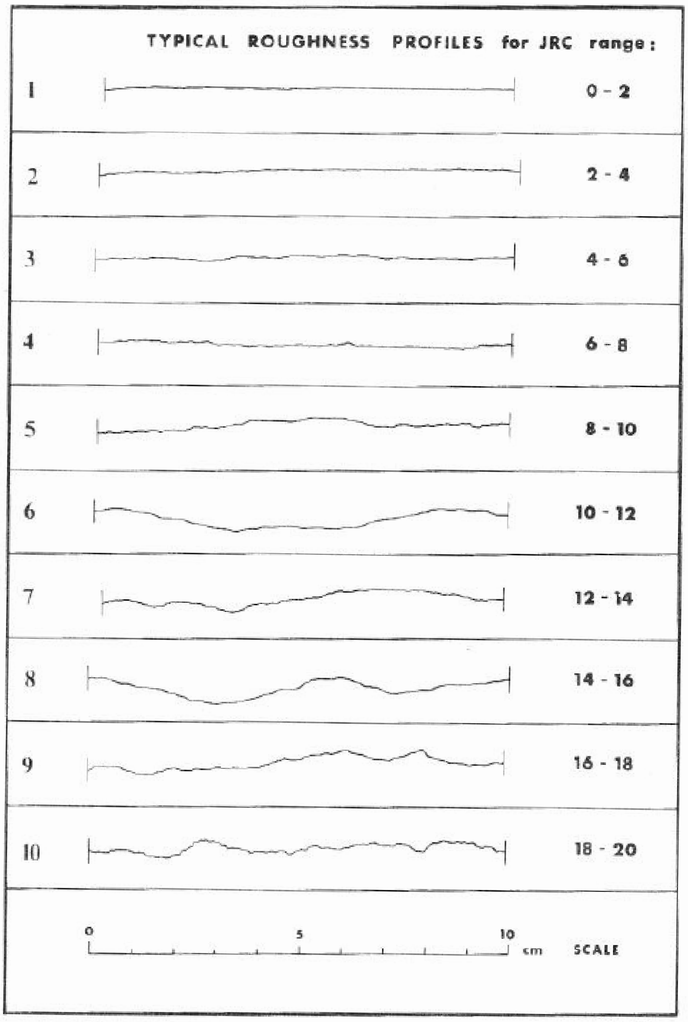

Figure 0-3. Classification of joint roughness according to Barton & Choubey (1977).